EARLY-AGE CONCRETE TEMPERATURE AND MOISTURE RELATIVE TO CURING EFFECTIVENESS AND PROJECTED EFFECTS ON SELECTED ASPECTS OF SLAB BEHAVIOR

A Dissertation

by

DAN YE

Submitted to the Office of Graduate Studies of
Texas A&M University
in partial fulfillment of the requirements for the degree of

DOCTOR OF PHILOSOPHY

August 2007

Major Subject: Civil Engineering

EARLY-AGE CONCRETE TEMPERATURE AND MOISTURE RELATIVE TO CURING EFFECTIVENESS AND PROJECTED EFFECTS ON SELECTED ASPECTS OF SLAB BEHAVIOR

A Dissertation

by

DAN YE

Submitted to the Office of Graduate Studies of
Texas A&M University
in partial fulfillment of the requirements for the degree of

DOCTOR OF PHILOSOPHY

Approved by:

Chair of Committee, Dan G. Zollinger
Committee Members, Robert L. Lytton
Dallas N. Little
Alan B. Palazzolo
Head of Department, David V. Rosowsky

August 2007

Major Subject: Civil Engineering

ABSTRACT

Early-age Concrete Temperature and Moisture Relative to Curing Effectiveness and Projected Effects on Selected Aspects of Slab Behavior. (August 2007)

Dan Ye, B.S., Southeast University, Nanjing, China;

M.S., Southeast Univeristy, Nanjing, China

Chair of Advisory Committee: Dr. Dan G. Zollinger

Concrete curing has long been realized to be important to produce durable concrete. Curing compound is widely used to cure concrete in the field. The current curing membrane evaluation method ASTM C 156, however, is incapable of distinguishing the curing compound quality and guiding the curing practice in the field. A new laboratory curing membrane evaluation protocol is developed in this study. It has the ability to rank the quality of curing compound and guide curing practice in the field according to the field ambient weather conditions and the type of curing compound. A series of field tests were conducted to investigate the key factors that affect the curing effectiveness in the field conditions.

A finite element program, temperature and moisture analysis for curing concrete ($TMAC^2$), is updated to solve the coupled and nonlinear heat transfer and moisture transport problems in early-age concrete. Moisture capacity is induced into the $TMAC^2$, which makes it unique to characterize the self-desiccation. A full scale concrete pavement test study was conducted at the FAA National Airport Pavement Test Facility (NAPTF) near Atlantic City, New Jersey. In this study, the material properties, i.e. thermal conductivity and moisture diffusivity, were backcalculated from field data. Thereafter, backcalculated material properties were used to forward-calculate the temperature and moisture histories of all other sections.

High order shear deformable theory is used to model the concrete slab curling and warping behavior because of highly nonlinear temperature and moisture gradients. The maximum shear strain is obtained a couple of inches below the concrete slab. This might account for the occurrence of delamination.

DEDICATION

To my mother, Yongwei Ye, and my wife, Chen Chen.

ACKNOWLEDGMENTS

The study presented herein was sponsored by TxDOT (Texas Department of Transportation) and FHWA (Federal Highway Administration), U.S. Department of Transportation. Their support is gratefully acknowledged. I would like to express my sincere gratitude to my advisor, Dr. Dan G. Zollinger, for his advice and help to complete this dissertation. I would also like to thank Dr. Robert L. Lytton, Dr. Dallas N. Little, and Dr. Alan B. Palazzolo for serving as advisory committee members.

TABLE OF CONTENTS

Page

LIST OF FIGURES

Page

Page

Page

Page

Page

LIST OF TABLES

Page

CHAPTER I
INTRODUCTION

Concrete has played a major role in the construction of the U.S. Interstate Highway System since 1956. According to the Federal Highway Administration (FHWA), the national highway system, which includes the nearly 45,000 mile interstate system, carries 40% of the nation's total traffic, 70% of the commercial traffic, and 90% of the tourist traffic. About 60% of the interstate system is made of concrete, especially in urban areas where heavy traffic loads prevail. The widely usage of concrete as pavement material can be credited to its excellent durability and less demands for repair. Concrete pavement commonly serves 20–30 years without needing major repair.

The design of concrete pavements is undergoing a passage from empirical design to mechanistic design, which requires a thorough and profound understanding of concrete pavement behavior from a mechanistic stand point. Early age concrete temperature and moisture history are fundamental characteristics that affect concrete strength development (Mindess and Young 1981; Neville 1996) and the source of concrete slab curling and warping behavior as well (Fang; Hveem 1951; Dempsey, Herlache et al. 1986; Ytterberg 1987; Kant and Gupta 1988; Kapila, Falkowsky et al. 1997; Byrum 2001; du Plessis and Harvey 2003; Jeong 2003; Jeong and Zollinger 2004).

PROBLEM STATEMENT

There are three main problems that this study is focused on, i.e. the laboratory curing membrane effectiveness evaluation, temperature and moisture analysis for curing concrete and concrete slab curling and warping behavior due to nonlinear temperature and moisture gradients.

This dissertation follows the style and format of the *Journal of Transportation Engineering*.

Laboratory Curing Membrane Effectiveness

Excessive early-age water evaporation from the surface of the concrete pavement may induce detrimental impacts, i.e. high porosity, delamination, and loss of strength, on the long term performance of concrete pavement. Spalling refers to the breakdown or dislodging of concrete segments along a joint or crack in a concrete slab within 0.6 m (2 ft) of a joint or crack (Miller and Bellinger 2003), and it affects the quality of concrete pavement smoothness and riding quality.

Texas Department of Transportation (TxDOT) has recently experienced cases of spalling and delamination failures which are related to excessive early age evaporation under the extreme field conditions, such as high temperature, low relative humidity, high solar radiation and high wind speed. To mitigate the early age unexpected water loss, application of curing compounds in concrete paving has been widely used to minimize evaporation. However, the TxDOT standard specifications for pavement construction (Item 526) only defines the use of the membrane curing in terms of key characteristics such as percent solids, density, viscosity, color and the application rate but does not specify curing performance or limits on the rate of evaporation. The current laboratory curing membrane effectiveness evaluation method ASTM C 156 has some intrinsic deficiencies, i.e. singular experimental conditions, mortar's hardening effect, and limited research on moisture loss limits. Therefore a new laboratory test protocol is needed to evaluate the curing membrane effectiveness in controlling evaporation.

Temperature and Moisture Analysis for Curing Concrete ($TMAC^2$)

Curing membrane plays an essential role as the boundary conditions for temperature and moisture analysis. Thus the ability to simulate the temperature and moisture history in early-age concrete is of great importance to assist curing effectiveness evaluation. Furthermore, early-age concrete temperature and moisture histories are relevant to crack control, sawcut, assessment of concrete strength development, and concrete slab curling and warping behavior due to such internal strain. Ambient weather conditions, mix proportions, and curing conditions affect the temperature and moisture histories in hardening concrete. The $TMAC^2$ program, a finite element program developed in Texas

Transportation Institute (TTI) to predict the early-age concrete temperature and moisture, has been under construction for over ten years. A series of breakthroughs, such as coupling of temperature and moisture analysis, heat loss due to evaporation, backcalculation of thermal conductivity and moisture diffusivity etc., have been accomplished. However, the relative humidity drop due to self-desiccation was neglected in previous version of TMAC^2. In this study, the moisture capacity is induced in the formulation of moisture transport governing equation, which enables TMAC^2 to quantify the relative humidity drop due to water consumption due to hydration.

Concrete Slab Curling and Warping Analysis

Concrete pavement thickness is the smallest of the three dimensions. Beam and plate theories are widely adopted as the basis to conduct mechanical analysis for concrete slabs. The variations of ambient weather conditions cause temperature and moisture changes leading to temperature and moisture gradients inside the concrete to result. These gradients cause concrete slabs to deform commonly referred to as curling and warping. Zero stresses are resulted at the midplane according the ordinary beam and plate theories. Delamination, however, sometimes occurs at the midplane of the concrete slab. This discrepancy of observation and theory is because the kinetic assumption of classic beam and plate theory excludes the existence of transverse shear (Timoshenko and Woinowsky-Kreiger 1959), which could account for the midplane delamination. The basic assumption of beam and plate theories is that plane sections remain plane and perpendicular to the midplane after deformation, which results in zero shear stress. But when concrete slabs are subjected to highly nonlinear temperature and moisture gradients, this assumption is difficult to satisfy. High order shear deformable beam (Kant and Gupta 1988) theory is used to conduct the curling and warping analysis to predict the delamination stress due to nonlinear temperature and moisture profiles.

STRUCTURE OF DISSERTATION

This thesis consists of seven chapters. Each chapter has its specific objective. The first chapter provides the significance of the research, scope of this study, and the structure of the thesis.

Chapter II reviews the current state of art pertinent to concrete curing issues, the studies regarding the early-age concrete temperature and moisture, and concrete slabs curling and warping modeling. Fig. I-1 shows the procedures to evaluate the concrete pavements under environmental impacts. Curing, mix proportion, and environmental conditions are the determinative factors that govern early-age concrete temperature and moisture and concrete properties development, which further affect the concrete slab behavior.

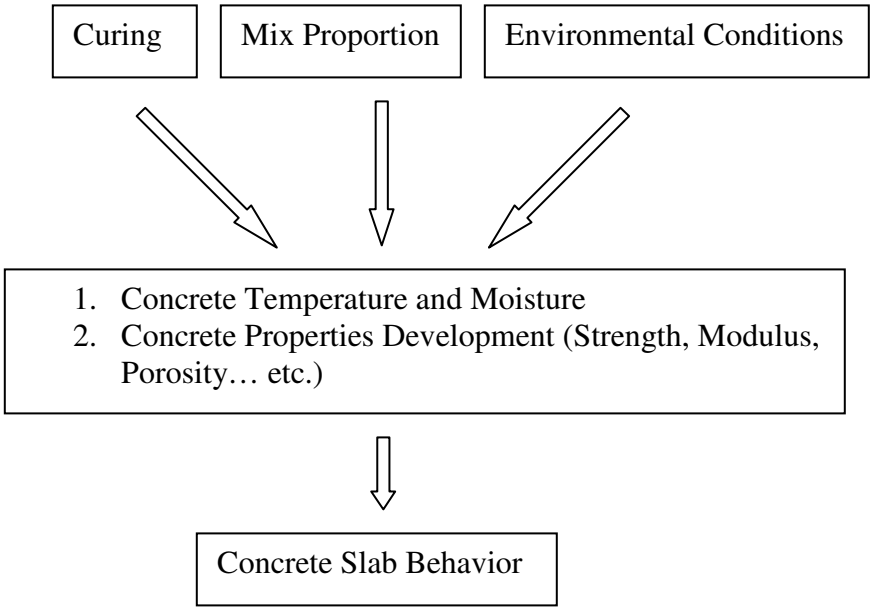

Fig. I-1. Hierarchy of Early-age Concrete Slab Evaluation

Chapter III presents a new laboratory protocol to substitute current ASTM C 156 as a curing membrane effectiveness evaluation method. The new protocol overcomes

the deficiencies of the ASTM C 156 and is able to guide curing practice according to the actual weather conditions and type of the curing compound. A series of curing compounds are ranked based on this protocol. A field application tool is presented in this chapter as well and describes a means for pavement engineers to manage curing in the field in terms of weather conditions at the time of construction and the type of curing compound.

Chapter IV presents all the field test data and a summary of findings based on the field data. Laboratory approved curing compounds don't guarantee a good curing practice in the field. Uniformity, scheme and timing of curing application are considered important factors to achieve good curing in the field. Thus field tests are needed to spot the factors that affect the curing quality in the field. The curing effectiveness in the field is evaluated based on both moisture retention and concrete physical properties.

Chapter V describes updating of early age concrete heat transfer and moisture transport models in TMAC^2. TMAC^2 is a finite element program that simulates the early-age concrete heat transfer and moisture transport. In the current version of TMAC^2, Thermal conductivity and moisture diffusivity were considered to be a function of concrete temperature, concrete moisture, and the degree of hydration, which makes the problem nonlinear and coupled. It is nonlinear because the thermal conductivity and moisture diffusivity matrixes are dependent of temperature and moisture, which are unknown variables; while it is coupled because two governing equations have to be solved simultaneously. In this research, moisture capacity is induced into the moisture transport governing equation, which makes it possible to simulate the relative humidity drop due to self-desiccation. A one dimensional simplification is adopted and the finite element formulae are derived based on this simplification in this chapter. The later part of this chapter presents a full scale concrete pavement test study to demonstrate how to evaluate the early-age concrete slab behavior with the assist of TMAC^2 program. The concrete pavement was cast at the FAA National Airport Pavement Test Facility (NAPTF) near Atlantic City, New Jersey. In this study, the concrete set maturity was

determined and the relationship between shrinkage and relative humidity was measured. For one of the sections, the temperature and relative humidity data were recorded at three different locations. The data was used to backcalculate the material properties, i.e. thermal conductivity and moisture diffusivity. The backcalculated material properties were used to forward-calculate the temperature and moisture histories of all other sections. Since concrete is still in its plastic state before final set, the effective temperature and moisture gradients should be offset by the gradients when concrete hardens, which are called set gradients. Based on the set maturity, the set temperature and moisture gradients were calculated as well.

Chapter VI uses high order shear deformable theory to model concrete slab curling and warping behavior subject to highly non-linear temperature and moisture gradients. Unlike ordinary beam and plate theories which assume cross-section planes remain plane and perpendicular to the midplane of the beam or plate, high order shear deformable theory gives more freedom in the horizontal displacement to accommodate the internal strains due to temperature and moisture gradients. A fourth order polynomial function is assumed for the horizontal displacement. And the governing equations are derived base on the energy principles. Finally, a sample calculation is provided.

Chapter VII concludes this dissertation in terms of a summary of the products and findings of this study.

CHAPTER II
LITERATURE REVIEW

This chapter reviews the current state of art pertinent to the concrete curing issues, the modeling of early-age concrete temperature and moisture, and the theories of concrete slab curling and warping behavior characterization. Curing membranes serve as the boundary conditions for heat transfer and moisture transport for early-age concrete. As a result, early-age concrete temperature and moisture are a direct assessment of concrete curing. Temperature and moisture gradients would induce internal strains, which trigger concrete slab curling and warping.

CONCRETE CURING

Firstly, a discussion will be given regarding what is concrete curing and what happens when cement hydrates. Secondly, a synthesis of current curing membrane effectiveness evaluation will be summarized. Lastly, the current lab evaluation protocol ASTM C 156 will be reviewed and its defects will be presented as well.

Concrete Curing Mechanism

Ensuring sufficient water availability in hydrating concrete is of great importance to achieve ultimate degree of hydration so as to produce delamination resistant concrete for both short-term and long- term performance of concrete pavement. Excessive early-age evaporation from the surface of concrete pavement results in high porosity concrete, delamination, and loss of strength.

The minimum amount of water needed for cement to achieve ultimate degree of hydration is about 0.44 gram of water per gram of cement (Powers 1947). This amount of water will provide room for the hydration products. So good curing practice should keep the concrete as nearly saturated as possible until the originally water-filled space has been filled with hydration products to some desired extent (Powers 1947).

An interesting discussion is about what is the minimum water content that hydration can occur? One researcher (Lasseter 1931) mixed 17 gram of cement with 1 gram of water and months later half of the water was still evaporable. Similarly, another attempt (Power and Brownyard 1947) mixed 8 gram of cement with 1 gram of water and both free water and unhydrated cement were found after four years curing under water. Therefore, even if there is in the presence of free water, cement might remain unhydrated. It is because that hydration product of 1 unit volume of cement takes up at least 2.4 unit volumes. The water cement ratio by volume 1.4:1 is equivalent to 0.44 by weight. This explains why the specimen cured under water for years still had unhydrated cement.

Relative humidity is a good indicator of the saturation condition of concrete mix. Researchers (Gause and Tucker 1940) placed fresh cement pastes in sealed bottles and kept tracking the relative humidity in the bottle. The test results are shown in Fig. II-1.

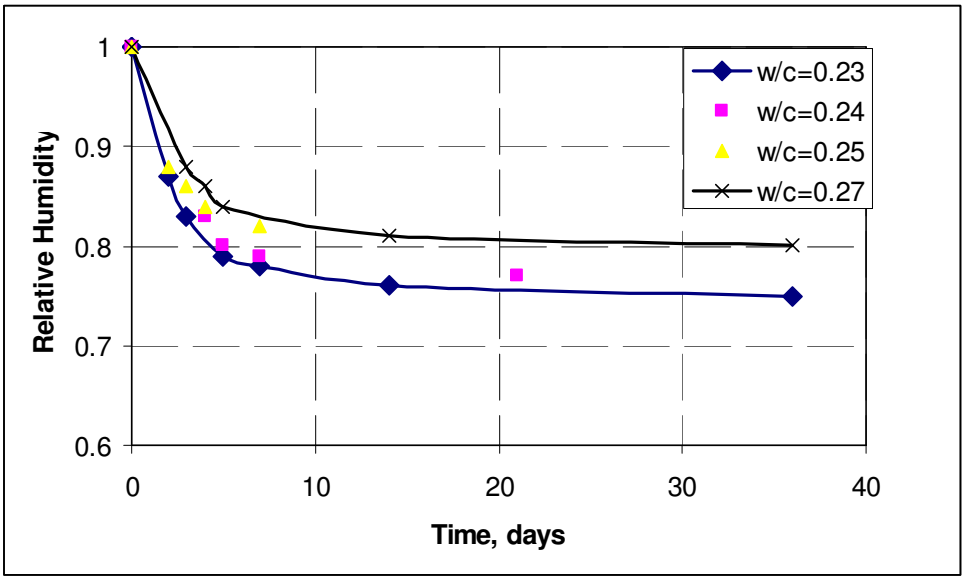

Fig. II-1. Reduction of Vapor Pressure over Sealed Pastes (Gause and Tucker 1940)

It is noted that the vapor pressure dropped at a progressively diminishing rate. The phenomenon where the water vapor pressure drops due to cement hydration is called self-desiccation (Powers 1947). Accordingly, the volume change due to self-desiccation

is called autogenous shrinkage (Davis 1940) and (Swayze 1942). It should also be noted that mixes with lower water cement ratios ended up with lower 'level-off' relative humidity, which is the indication of cessation of hydration. Therefore, it is evident that the hydration of cement in sealed container would not drop water vapor pressure down to 0.75 or 0.80.

In another interesting experiment (Powers 1947), several portions of cement were stored in chambers with different moisture conditions. The amounts of total and non-evaporable water were determined. The results for 6 months of exposure are shown in Fig. II-2. It is noted that the water taken by cement when water vapor pressure was below 0.8 was comparatively low. When water vapor pressure was above 0.8, the cement took much more water, which indicates the hydration rate was quite higher. This result is in agreement with previous tests. Since then, researchers began to believe that the vapor pressure must be maintained at a comparatively high value (relative humidity 0.8) in order to ensure hydration proceed at an appreciable rate.

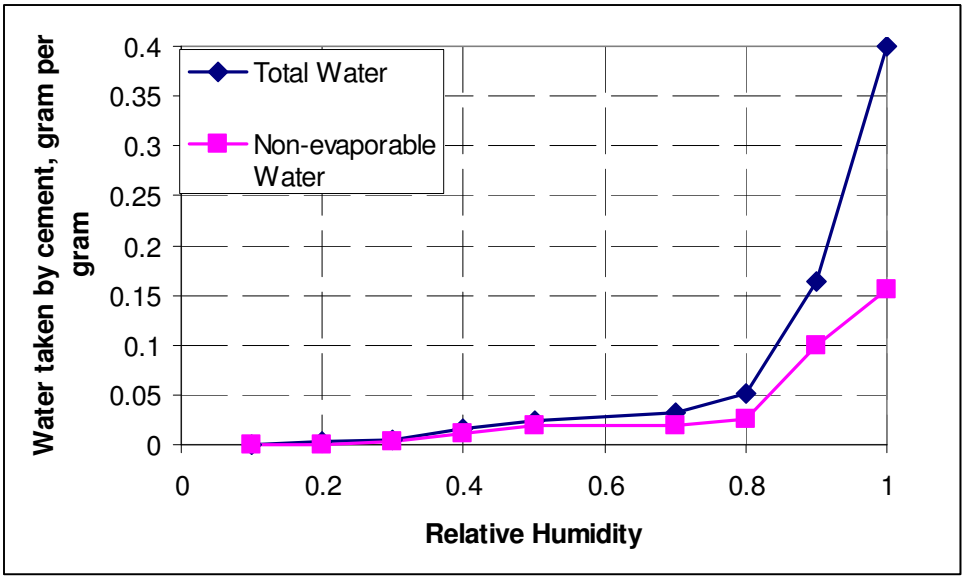

Fig. II-2. Amounts of Water Taken Up by Dry Cement Exposed to Water Vapor for Six Months (Powers 1947)

As stated earlier, hydration products can only take up the water-filled space. In porous media, the relationship between condensed water content and vapor pressure is well defined by Kelvin's equation. When cement grains are exposed to water vapor like the experiment mentioned earlier, capillary condensation will occur. Condensation occurs at the points of contact between grains. For a simple case, a ring of water is condensed around a point where two identical spheres contacts, as shown in Fig. II-3. Under equilibrium situation, water vapor in the voids is balanced with the saturated pressure in condensed water by the surface tension of the water. The Kelvin's equation for this case is given by equation (II-1). This equation states, from a curing perspective, that the higher the vapor pressure is the greater the amount of condensed water, which allows more hydration products to form.

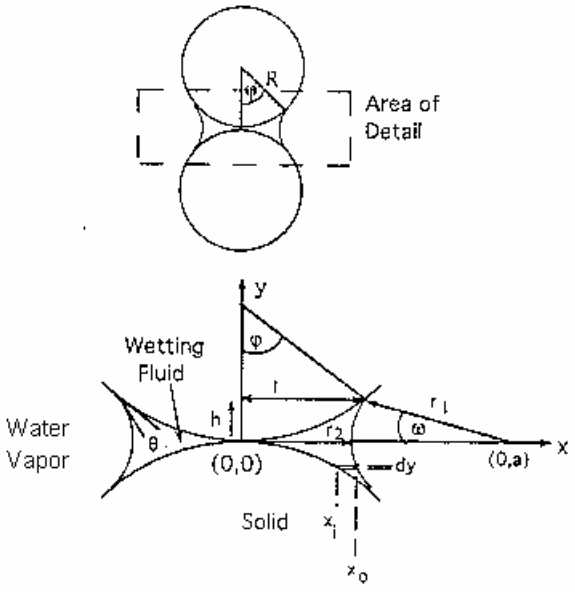

Fig. II-3. Diagram of Water Ring around the Contact Point of Two Spheres (Powers 1947)

$$\frac{1}{r_1}+\frac{1}{r_2}=-\frac{RT}{Mv_f\gamma}\ln\left(\frac{p}{p_s}\right) \qquad \text{(II-1)}$$

where

r_1 = radius of concavity,

r_2 = radius of convexity,

γ = surface tension of the water,

v_f = specific volume of water,

M = molecular weight of water,

R = gas constant,

T = absolute temperature,

p = vapor pressure, and

p_s = pressure of saturated vapor.

Classification of Curing Compound

According to ASTM C 309-03 (2003), the following types of liquid membrane-forming compounds are included:

- Type 1 – Clear or translucent without dye,
- Type 1-D – Clear or translucent with fugitive dye, and
- Type 2 – White pigmented.

The solids dissolved in the vehicle shall be one of the following classes:

- Class A – No restrictions,
- Class B – Must be a resin as defined in Terminology D 883.

In TxDOT, only type 2 (white pigmented) curing compounds are approved. Fig. II-4 and Fig. II-5 illustrate the compositions of resin-based curing compound and wax-based curing compound, respectively.

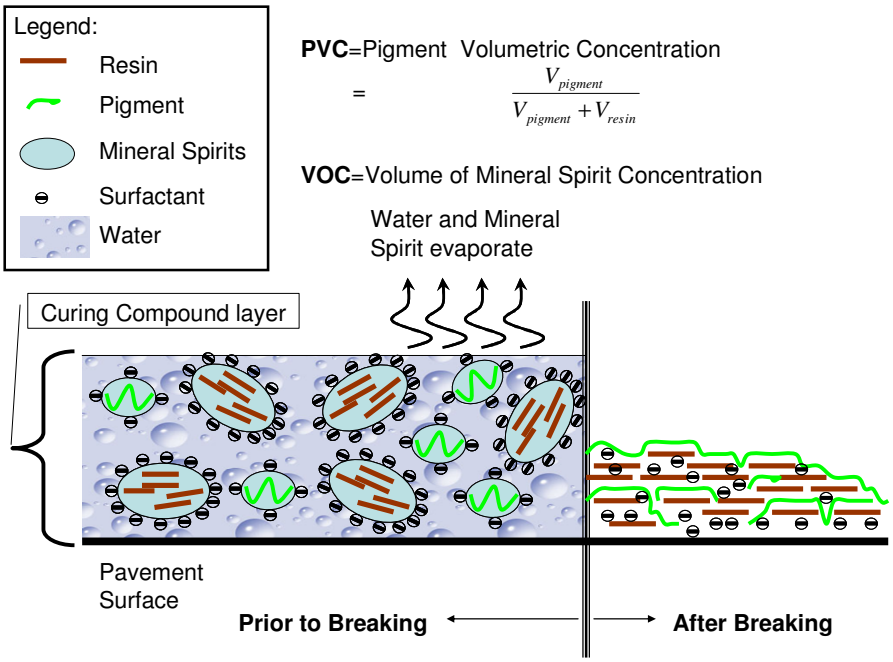

Fig. II-4. Diagram of Resin-based Curing Compound (Type 2 Class B)

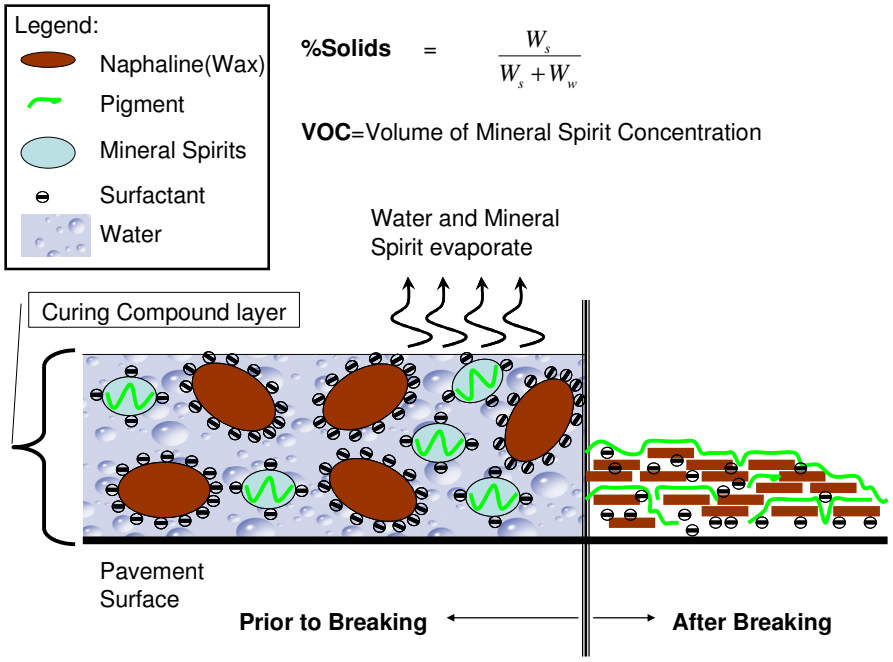

Fig. II-5. Diagram of Wax-based Curing Compound (Type 2 Class A)

Synthesis of Curing Membrane Effectiveness

Some investigations into the effectiveness of curing membranes have tended to measure special concrete properties (i.e. oxygen permeability, electrical conductivity, porosity, etc.) that caused by or related to the availability of hydration of water and comparing those parameters to evaluate the effectiveness of curing compound. Although these parameters do have some utility in this regard, their use in curing specifications has some practical limitations since it is difficult to evaluate the curing membrane effectiveness in this manner under field conditions. Some researchers have concluded that maturity is not a good indicator of curing effectiveness. However, this is because only temperature-based maturity was considered. Research under project 0-1700 (Mukhopadhyay, Ye et al. 2006) found that moisture-based maturity was very effective in this manner. The following provides a review of current literature on evaluating curing membranes effectiveness and briefly summarizes the work done in Research Project 1700 regarding assessment of curing effectiveness.

Researchers (Carrier and Cady 1970) evaluated the effects of various application rates of membrane-curing compounds on concrete using a laboratory test in which slab specimens were cured with rates from zero to 100ft^2/gal. To evaluate the effectiveness of application rate, the moisture changes were characterized in terms of changes in relative humidity (RH) and changes in relative surface strengths using the Schmidt hammer. The test specimens were made with five application rates of curing compound: 0, 50, 100, 150, and 200 % of the standard coverage (200ft^2/gal) with a white-pigmented type commonly used in Pennsylvania. The RH measuring points were positioned at depths ranging from 0.25 to 2 in. below the concrete surface. The field environment simulated in the lab was that of a hot summer day where the air temperature was cycled daily (4 h at 110 ± 2 °F - heating phase - and 20 h at 75 ± 2°F) and the wind speed was held constant at 4 ± 1 mph during the heating phase and the RH is maintained at 20 ± 5 %. The RH of specimen was measured at 1, 2, 3, 5, 7, 9, 11, and 14-days of age with the strengths of cured specimen surface were measured with the Schmidt hammer after 14

days of age. Petrographic examination of the surface concrete determined the differences in the extent of hydration. They reached to the following conclusions:

1. In the measurement of RH, while the zero coverage specimens dried quickly, the specimen sprayed with 200 % application (100 ft^2/gal) loses as much moisture as those sprayed with 50 % (400 ft^2/gal).
2. Hydration virtually ceases when concrete dries below RH of about 80% at which the water-filled capillaries begin to empty. Therefore, the effective curing time is the period that the RH in concrete maintains above 80%.
3. The effective curing time increases with increasing application rates; that is, the curing period with zero application rates is very short, while the others increase progressively with increasing application rates.
4. The result of strength test appears to be similar to that of RH test. The result indicates that while the 0% coverage surfaces are much weaker than any others, the specimens with different application rate have almost same strengths within the accuracy of the Schmidt hammer. The surface strengths of specimens sprayed appear to be similar regardless of the curing time of some specimens.
5. Petrographic examination shows similar qualitative results; that is, while the upper mortar of the sprayed specimens appears much stronger than that of the unsprayed specimens, there are no differences between the sprayed specimens.
6. For the depth more than 1 in. below the membrane, the concrete maintains the 80% of RH even at 28-day; that is, the surface membrane would not affect the internal concrete curing. However, for the upper 1 in. of concrete, the moisture distribution increases as the application rate of curing compound increases.

Curing efficiency was evaluated based on oxygen permeability and moisture loss measurements. Both results are compared in Table II-1. The curing efficiency from oxygen permeability is statistically better than that from moisture loss measurements.

The oxygen permeability tests maybe a good method to assess the traditional methods of curing.

Table II-1. Comparison of Curing Efficiency Results (Carrier and Cady 1970)

Curing membrane	**Solvent-borne resin**	**Wax emulsion**	**Solvent-borne acrylic**	**Acrylic emulsion**
Curing efficiency* from moisture loss (%)	87.0 (3.8)**	90.1 (3.0)	81.3 (7.2)	56.2 (11.1)
Curing efficiency* from oxygen permeability (%)	82.2 (1.8)	92.8 (2.2)	84.6 (2.9)	52.6 (6.8)

The efficiency of selected curing compounds to cure concrete was assessed by Wainwright and Cabrera (1990) that involved as one type of laboratory test the monitoring of evaporation of water from mortar specimens under controlled environmental conditions. Four types of curing compounds were evaluated by measuring compressive strength, total porosity, degree of hydration, rate of moisture loss, and oxygen permeability. Concrete slabs of 600 x 300 x 100 mm and mortar slabs of 300 x 150 x 50 mm were cast and kept at 35 ± 1ºC, 45 ± 5 % RH under a 3 m/s wind velocity. The four compounds tested were solvent-borne resin (resin-based), wax emulsion (wax-based), solvent-borne acrylic, and acrylic emulsion. The compounds were applied at a rate of 0.2 liter/m^2.

Compressive strength was measured at 3, 7, and 28 days using 100 mm cubes. The 28 day strength of non-cured specimens was about 22% and 19% lower than those water-cured for 3 days and those cured with a wax emulsion membrane, respectively. Moisture loss was measured by monitoring the weight change with time. The water loss trends were similar to those of compressive strength but the difference between curing types was greater. However, all curing methods produced significant reduction in moisture loss. The wax emulsion compound performed the best and was almost three times less than that of non-cured concrete.

Porosity was measured at various depths beneath the surface of the concrete slabs. The trends were similar to the test results noted above. The difference between curing methods decreased as the depth below the surface increased. However, since the concrete more than 50 mm below the surface is rarely affected by curing conditions at the surface, the differences between curing methods become insignificant at depths more than 50 mm. The measurement of the pore size distribution was conducted using samples taken within 12 mm from the surface for both cured and non-cured mortar slabs. The results show that the volume of the capillary pores greater than 0.01μm is significantly reduced for the cured specimens.

Oxygen permeability was measured with samples taken at various depths beneath the surface of the concrete slabs. The results were similar to those of the porosity test. Near the surface, the non cured concrete was 8-10 times permeable than cured concretes. Similar as the measured porosities, the difference is insignificant at depths more than 50 mm below the surface.

The study shows that although all test results present a similar trend, the oxygen permeability test is most sensitive and the wax emulsion is the most effective curing membrane. The concrete more than 50 mm depth is little affected by curing condition. The permeability test was recommended for assessment of potential durability and the curing efficiency since the permeability reflects potential durability of concrete and is mainly affected by curing methods.

Cable, Wang, and Ge (2003) carried out a research project sponsored by Iowa DOT to evaluate curing compound materials, application methods, and effects of curing on concrete properties. The research consisted of laboratory testing and field evaluation of identified products and application rates. The research showed that curing materials and application methods have a critical effect on the properties of the near-surface concrete particularly in hot weather conditions. Concrete cured with curing compounds that were indexed with a high curing efficiency had lower sorptivity, higher conductivity, higher degree of hydration, and higher compressive strength. Among these tests, the sorptivity test is the most sensitive indicator for quality whereas the compressive and

flexural strengths were not. The sorptivity showed a close relationship to moisture content and degree of hydration while the conductivity showed a strong correlation to moisture content of the concrete.

Curing compound materials and related application methods were evaluated in the field relative to the properties of field concrete pavement. The curing compounds tested are listed in Table II-2 according to Iowa DOT designations and their rated qualities. The 1600-white series (1645 white and 1600 white) are wax-based, white-pigmented concrete curing compounds with selected white pigments. The difference between 1645 and 1600 is the solid content that 1645 has 29.2% and 1600 has 17.1%. The 2200- white series concrete curing compounds are high solids, white pigmented, polyalphamethylstryene-based (resin-based).

Table II-2. Typical Properties of the Curing Compounds

Curing Compounds	Efficiency Index	Estimated Cost ($/gal)
1645-White	95.9	2.0
1600-White	89.0	1.0
2255-White	98.1	6.5

The compounds and two application rates were compared to no curing and wet curing by testing the conductivity, permeability, and maturity of the surface concrete. The conductivity is a measure of water retentivity of a curing compound; the maturity should be an indication of the degree of hydration, and the permeability an indication of durability of the near-surface concrete. The efficiency index is defined as:

$$Efficiency = \frac{E_o - E_c}{E_o - E_w} \tag{II-2}$$

where

E_o = moisture loss for omission of curing,

E_c = moisture loss for certain curing compound, and

E_w = moisture loss for wet curing.

Maturity testing conducted in the manner it was did not prove to be beneficial. The maturity could not sufficiently evaluate the effectiveness of curing and was not sensitive to environment effects such as the air temperature, humidity, wind, or rainfall on the degree of maturity of the concrete.

The permeability testing was conducted at the top, middle, and bottom of cores taken from the pavement. The test data showed little difference in the middle and bottom permeability and there seemed to be no difference between different curing methods; the without curing however, yielded higher permeability at the top. The sections with cuing compound and with wet curing had almost the same permeability. The permeability also decreases as the depth increases.

This research showed that electrical conductivity is statistically related to moisture content of the concrete and that the method of curing affected the top of pavement more than portions deeper below the surface. Deep sections had higher conductivity than at the top because of evaporation. Accordingly, the effectiveness of a curing method is ascertained by comparison between the initial and current conductivity values. The conductivity results shows the same trend with the efficiency index of curing compounds listed in Table II-1. No sorptivity test or moisture content results were given but the degree of absorption of water is thought to be closely related to the pore structure characteristics of concrete and should be a good test for the curing effectiveness. The moisture content readings with time showed a large variation due to several factors such as texture of the pavement, measuring position, and environmental change.

This research concluded that only slight differences existed between wet curing, compound curing and no curing; while the maturity test could not identify the difference between different curing compound materials. The permeability test showed that cuing compounds provide the same quality as wet curing and that the compound materials

tested were ranked as: wet curing, 2255 single layer, 1645 double layer, 1645 single layer, and 1600 double layer.

The Minnesota's Department of Transportation (Mn/DOT) examined and evaluated curing compounds used in the state projects relative to any needed changes in their curing specification (Vandenbossche 1999). Some of the work focused on the application of the compound to the pavement surface. The Mn/DOT requirement is 4 m^2/gal (163 ft^2/gal) regardless of the type of pavement surface such as tinning or texturing which increases the surface area. The application rate should be determined based on surface texture and application device in order to obtain uniform coverage. The five factors listed below affect the curing compound application.

1. Nozzle type : spray pattern, droplet size, pump pressure, spray angle, flow rate,
2. Nozzle spacing and boom height : adjusting for 30% overlap of spray pattern edge,
3. Nozzle orientation,
4. Cart speed, and
5. Wind shield.

It was thought that non-uniform coverage is mainly caused by damage to the nozzle or orifice. Nonetheless, Mn/DOT showed that the desired coverage can be achieved by the proper nozzle selection, cart speed, pump pressure, flow rate and so on. The study proposes the following recommendation for applying a curing compound:

1. The application of the curing compound should be calculated based on the type of surface texture maintaining a minimum of 4 m^2/gal (163 ft^2/gal).
2. 30 % of the spray overlap should be obtained.
3. The coverage should not be controlled by the pump speed but by the cart speed.
4. The cart speed should be calculated using the following equation.

$$v = \frac{coeff. \times F}{C \times w} \qquad \text{(II-3)}$$

where

v = cart speed (km/h, or miles/h),

coeff. = 6 for SI units, or 0.13636 ,

F = flow rate (L/min, or gall./ min) per nozzle,

C = desired coverage (L/m2, or gall/ft2), and

w = Nozzle spacing (cm, of inches)

In another MnDOT related study, Whiting and Snyder (2003) evaluated the effectiveness of high and low volatile organic compound (VOC) curing compounds by examining the moisture-retention capacity of them. A modification of ASTM 156-98, Standard Test Method for Water Retention by Concrete Curing Materials, was used for this evaluation. In addition, compressive strength, permeability, and capillary porosity of hardened mortar samples were also determined. Three different curing methods, ponded water (Treatment W), no curing (Treatment N), and polyvinyl sheeting (Treatment P), are also examined for reference. The curing compounds used for test are low VOC (L-1, 2, 3) and three of high VOC (H-1, 2, 3). Infrared fingerprinting, characteristic of surface coverage, and percentage of solids are examined to understand this aspect of each curing compound tested.

The moisture retention was measured by monitoring the mass loss of each mortar specimen. The curing compound was applied as soon as the bleed water has disappeared and the application rates were based on the minimum rate recommended by the manufacturers. The specimens were cured in the test chamber at a specific temperature, RH, and evaporation rate.

As expected, the result of the moisture retention test showed that Treatment P was the most effective. However, generally speaking, the high VOC compounds showed a lower rate of moisture loss than the low VOC compounds but moisture loss was high within the first 24 hrs and then the gradually stabilized. Although ASTM requires the moisture loss after 72 hrs to be less than 0.55kg/m^2, only Treatment P met that

requirement. Moisture retention capacity of the curing compounds was evaluated relative to the moisture loss for the Treatment N:

$$\%Effectiveness = \frac{Mn - Ms}{Mn}(100) \qquad \text{(II-4)}$$

where

Mn = average moisture loss of specimens from Treatment N, and

Ms = average moisture loss of specimens from treatment being considered.

The % effectiveness decreases with time for all treatments where Treatment P had the highest %Effectiveness.

In terms of compressive strength, mortar specimens cured with high VOC compounds gained strength more quickly than those cured with low VOC compounds. The 28 day strength of Treatment N cured mortar was about 54% of that of Treatment W. The 28 days strength of specimens with curing compounds ranged from 55% to 75% of the strength achieved using Treatment W. The result showed that curing method has a greater impact on long term strength development than early age strength. A high correlation existed between the average moisture loss and the compressive strength. There was also a strong correlation between the percentage of solids and compressive strength. However, the percentage of solids is apparently only a good indicator if the compounds are chemically similar.

The relative permeability of the specimens was also estimated using the RCP test at 3, 10, and 28 days. After 3 and 10 days of curing, the estimated permeability of all specimens was high, exceeding 4,000 coulombs. After 28 days of curing, all test results range from moderate to high permeability. The low VOC samples had the highest permeability value and Treatment W and Treatment P had the lowest value.

In conclusion of the study, the specimens with high VOC compounds show less moisture loss, higher strength, and lower permeability than those with low VOC compounds. The specimens cured with plastic sheeting show better moisture retaining ability, long term strength, and lower permeability than any other curing compounds.

However, early strength is higher in some specimens with a high VOC compound than in those with plastic sheeting. Thus, the VOC content does not appear to be the best indicator of how a curing compound will perform.

Review of ASTM C 156

Current Texas Department of Transportation (TxDOT) specification for curing membrane application practice requires two applications, each of which has an application rate of 180 ft^2/gallon. The criteria for selecting curing compounds for paving activities are: water retention, pigments, drying time, type and amount of solids, volatile organic compounds (VOC), and compatibility with coatings.

The standard test, ASTM C 156 "Standard Test Method of Water Retention by Concrete Curing Materials", is focused on water retention and requires a controlled environmental chamber that has a potential of evaporation from 0.65 to 1.1 kg/m^2/hr (0.133 to 0.225 lb/$ft^{2/}$hr). The standard water loss limit according to ASTM C 309 and AASHTO M 148 is 0.55 kg/m^2 (0.113 lb/ft^2) for a duration of 72 hours, and TxDOT specifications require that the total water loss with respect to the total weight of specimen is less than 2% at 24 hours and less than 4% at 72 hours. This standard water loss limit is based on the strength of stripped and coated cylinders dating to the 1930s and 1940s.

The method is relatively straightforward but apparently the reported precision between laboratories is poor, and several deficiencies can be pointed out. The method is also rather limited as far as field application since it is conducted under fixed ambient conditions (temperature, relative humidity, and wind speed) and a single application rate, while field environmental conditions represent a variety of these combinations. Secondly, ASTM C 156 specifies the use of mortar specimens to conduct the evaporation test, which exhibits a high evaporation rate initially while the specimen is still fresh and then decreases as the mortar hardens. The majority of moisture loss occurs during the initial stages and very little after that takes place during the 72 hour period. Thirdly, the dimension of the strength test specimen is too large to capture the subtlety induced by different curing methods; in order for the difference in strength to be

noticeable, the difference of the physical properties of the concrete at the top of the specimen that is subject to exposure would need to be enormous. Nowadays, curing is key to achieving quality concrete within the top a few inches of the exposed surface. The following discussion will elaborate these aspects of ASTM C 156 as a curing compound effectiveness evaluation method.

Singular Experimental Conditions

ASTM C 156 is carried out under a singular set of ambient conditions and with only a curing compound application rate. Since ambient weather conditions have huge variations, curing effectiveness needs to be defined over a range of humidity and wind conditions. As a result, the final curing effectiveness is the combination of the effect of curing practice and ambient conditions, as shown in Fig. II-6. Curing practice includes the type of curing compound, application rate, and uniformity. Ambient conditions consist of temperature, relative humidity, and wind speed.

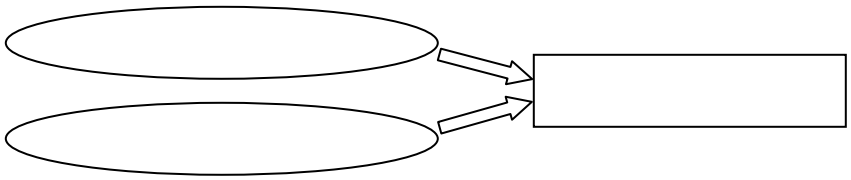

Fig. II-6. Factors on Curing Effectiveness

The controlling conditions required in ASTM C 156 are listed in Table II-3. There is no specific requirement for wind, which is crucial factor affecting the evaporation rate. ACI nomograph (ACI 308) can be used to characterize the effect of weather on evaporation potential. It takes the input of air temperature, air relative humidity, concrete temperature, and wind velocity, as shown in Fig. II-7. This nomograph can also be represented in Equation (II-5), which has variables of air temperature, air relative humidity, and wind speed.

Table II-3. ASTM C 156 Environnemental Conditions

Temperature	37.2 ±1.1 ºC (99.0±2.0 ºF)
Relative Humidity	32±2%

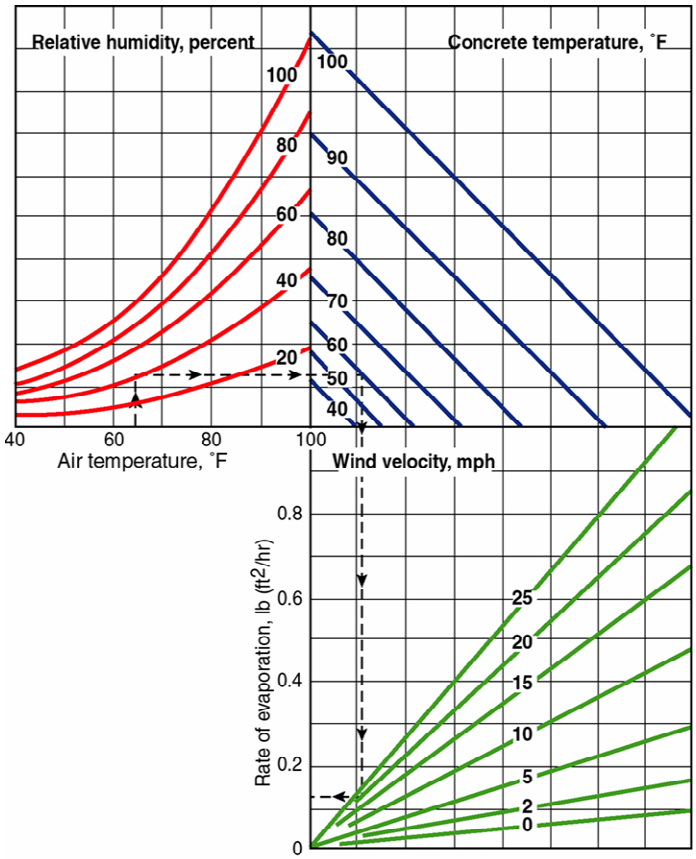

Fig. II-7. Nomograph in the American Concrete Institute Guide (ACI 308)

$$PE = [T_c^{2.5} - (R *\times T_a^{2.5})] [1 + 0.4 V] * 10^{-6} \quad \text{(II-5)}$$

where:

PE = Potential of Evaporation rate, lb/ft^2/hr

T_c = Concrete Temperature, ^{o}F

T_a = Air Temperature, ^{o}F

R = (Relative Humidity %) / 100, and

V = Wind Velocity, mph

According to this equation, the weather severity index for ASTM C 156 is 0.066 lb/ft^2/hr. In Texas, the air temperature can go as high as 105 ºF and with the effect of the wind the potential of evaporation rate can go up to 0.600 lb/ft^2/hr, on the other hand, the potential of evaporation is as less as 0.020 lb/ft^2/hr with the air temperature 70 ºF, relative humidity of 50%, and no wind. Using a test method carried out under a singular condition is not sufficient, thus a comprehensive curing evaluation system should be based on the tests under a variety of PEs.

Mortar Specimen

ASTM C 156 describes a method to evaluate water retention as a measure of curing effectiveness. The method involves the measurement of evaporation from a mortar specimen over a period of 72 hours. The mortar exhibits a high rate of evaporation while it is fresh and a lower rate when it is hardened. Following this procedure, it is nearly impossible to separate the water retention capacity of curing membrane from that due to the hardening of the mortar. Consequently, the evaluation of the water retention capability of a curing compound is seriously compromised.

A special lab test was conducted to demonstrate the extent the hardening of the mortar contributes to the reduction of water loss. Four short cylindrical specimens with a diameter of 6 in. and a thickness of 2 in shown in Fig. II-8 were prepared. The environmental conditions are listed in Table II-4.

Table II-4. Environmental Conditions

Temperature	104 ºF (40 ºC)
Relative Humidity	30%
Wind Speed	10 mph
PE	0.395 lb/ft^2/hr

The environmental conditions for these tests were according to Table II-3, and a wind flow of 10 mph was applied. The weight losses for mortar specimens and water specimens are show in Fig. II-9 and Fig. II-10, respectively.

As shown in Fig. II-9, the weight loss for the mortar specimens is divided into four stages to facilitate understanding of the effects of the mortar hardening on water loss. Mortar specimens exhibit a high initial moisture loss rate but the total moisture loss gradually levels off, while water specimens show a constant moisture loss rate. The constant moisture loss rate indicates that the curing compound is stable under constant ambient conditions. Fig. II-10 shows that the rates of moisture loss for water specimens were constant throughout the testing period, which indicates the properties of the curing membranes remained unchanged.

Fig. II-8. Specimens for the Special Test

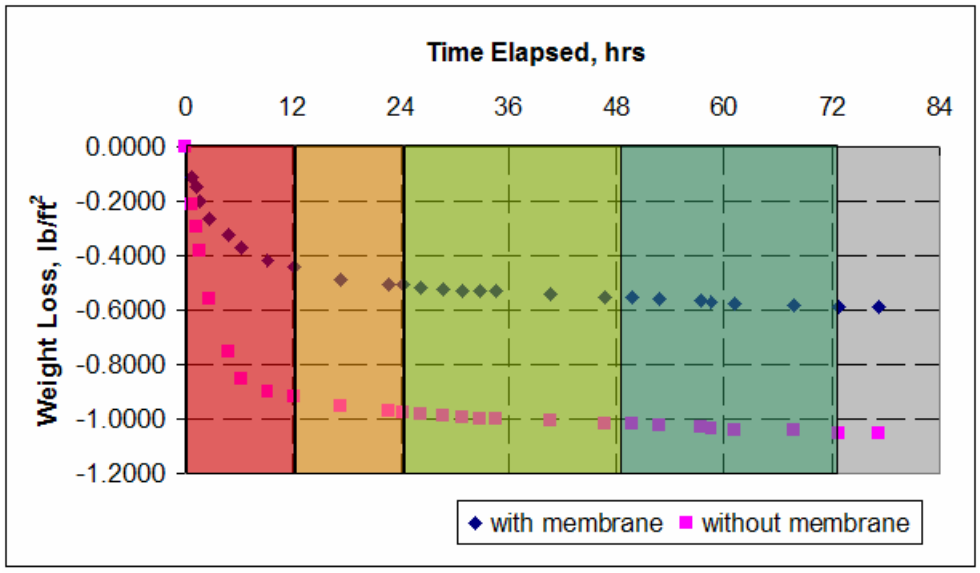

Fig. II-9. Weight Loss for Mortar Specimens

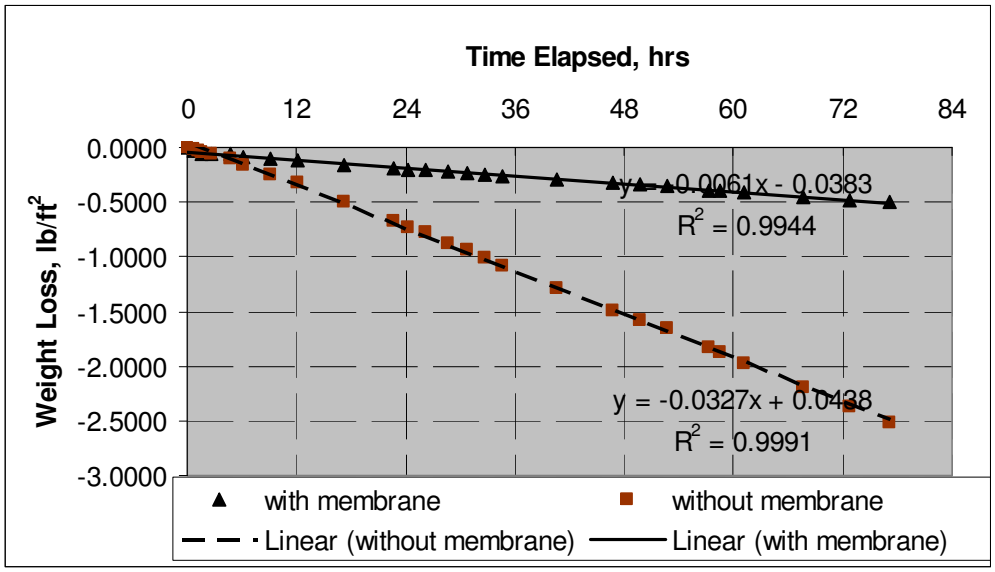

Fig. II-10. Weight Loss for Water Specimens

Fig. II-11 shows a comparison of mortar specimen water loss at different stages. The first 12-hour stage is the only one in which the non-cured sample moisture loss is evidently larger than that of cured sample. For the remaining stages, the moisture loss differences between cured and non-cured samples are very small. However, in the first

stage the most evaporated water is bleeding water, which would not cause much problem as far as curing is concerned. Water loss in that state occupies a huge amount of the total loss. In the rest three stages, the moisture loss from the two specimens were about the same. This evidence suggests that the rate of moisture loss due to the hardening of the mortar is nearly equivalent to the rate of moisture loss of the membrane cured mortar. The huge water loss, which has less impact on curing effectiveness, at the first stage and mortar's hardening effect complicate the interpretation of moisture loss data. Furthermore the starting point of recording moisture loss is when bleeding water stops. However, it is really difficult to justify the stoppage point, which results in huge variation of moisture loss in the first stage. This accounts for the poor precision of this method.

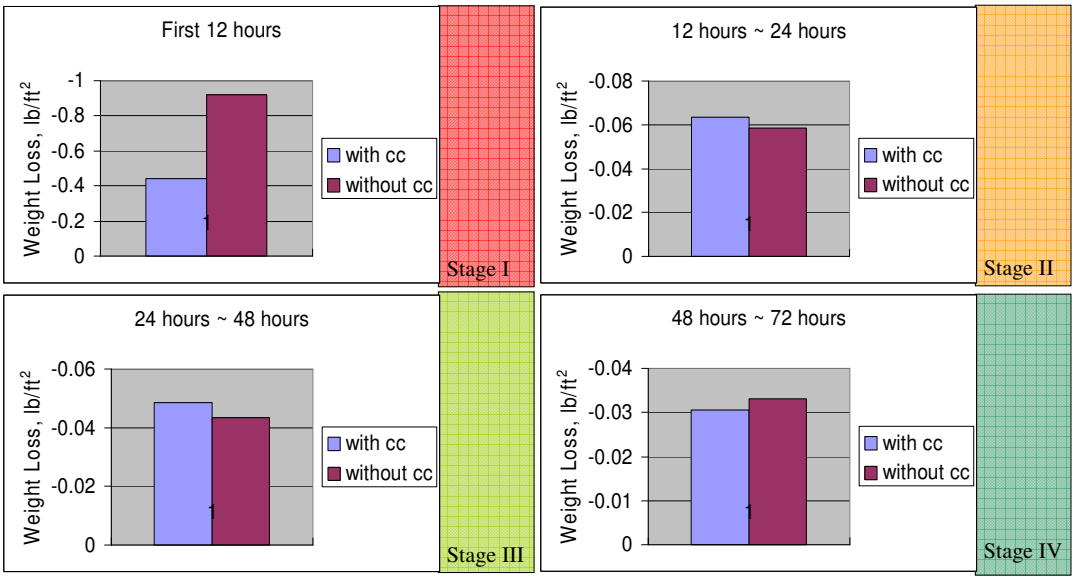

Fig. II-11. Weight Loss at Different Stages

Limits on Moisture Loss

The standard water loss limit according to AASHTO M 148 and ASTM C 309 is 0.55 kg/m2 (0.113 lb/ft2) for a duration of 72 hours. The water loss limit is based on the strength of stripped and coated cylinders dating to the 1930s and 1940s. The question is that the strength of the cylindrical specimen is determined by its overall strength and its

defected top part might not affect the overall strength that much. The limit should, perhaps, be lower due to the composite effect of the large volume of the fully cured concrete. As shown in Fig. II-12, it would be more meaningful to investigate the properties of the top part of the specimen other than taking the compression strength of the whole cylinder specimen which comprises of large volume of well cured concrete

Curing affects only the very top part of the exposed concrete. It is inappropriate to use thick samples to conduct a compression strength test to substantiate the curing effectiveness. Physical properties (total porosity, permeability) test in the top part of concrete specimen is more desirable when evaluating curing effectiveness.

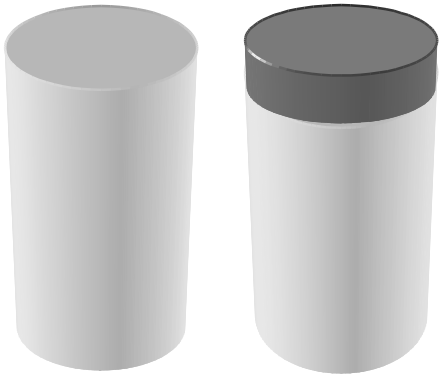

Fig. II-12. Diagram of Cylinder Samples of Different Top Conditions

Spray Technology

The new laboratory protocol, which will be presented in the succeeding chapter features linkages between curing practice (application rate) according to the actual ambient conditions (potential of evaporation) and type of curing compound (ranking of curing compound). These linkages instill a greater level of versatility in the curing equipment technology. This section reviews present technologies pertinent to curing compound spraying.

Typical type sprayers used in the field consist of spray nozzles, lines, pump, tank, pressure regulator, pressure gauge, strainers, shutoff valve and agitator. Some sprayers are equipped with pressure activated shutoff valves at each nozzle to stop nozzle flow

without dripping. The pump moves the material from the tank and pumps it to the spray nozzles. Pressure at the spray nozzles is determined by the setting of the agitator control valve and the pressure regulator, the capacity of the pump, and the pressure loss in lines, and fittings between the pressure gauge and the nozzles. For slip form pavers, sprayers use a boom with nozzles spaced uniformly along the boom as shown in Fig. II-13.

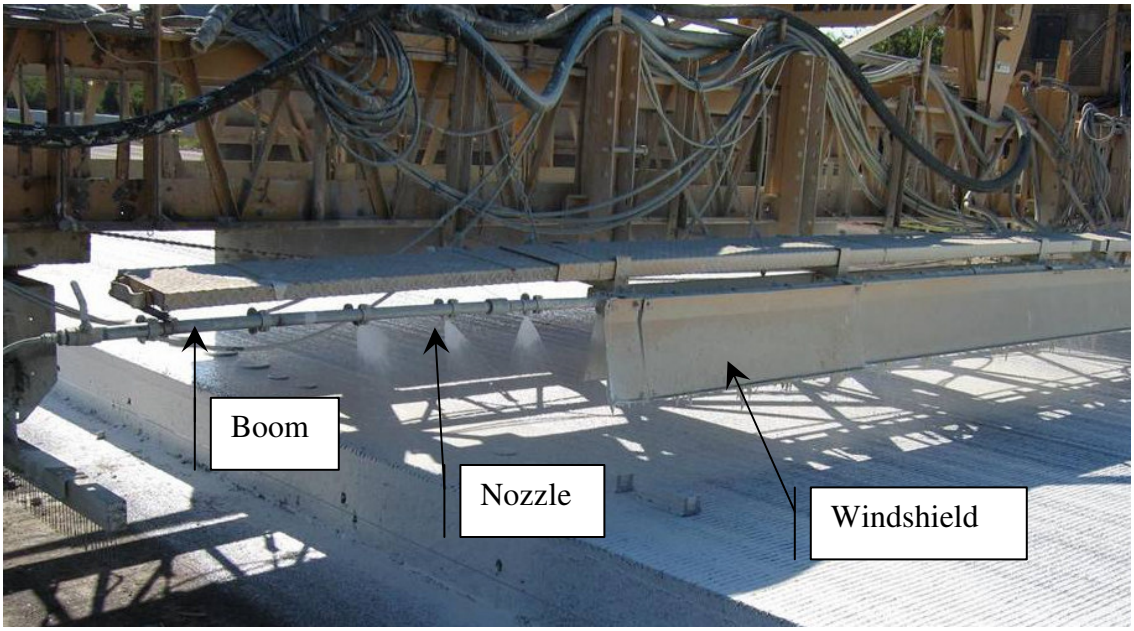

Fig. II-13. Curing Application by Slip Form Paver

In the chip seal industry, designated application rates of the asphalt binder on the pavement surface are re checked periodically by placing either buckets or absorbent pads across the width of pavement (as depicted in Fig. II-14). Before and after pad weights are taken so that the weights of the binder applied can be obtained. The application rates on each pad are then calculated based on the weight gained and the pad area. Since the pads are placed across the width of pavement, the application rate distribution transversely can also be obtained. The control of application process is also automated and metered, however, the purpose of the metering is mainly to set to control the initial rate of application and the application pressure. The application is also checked for

spray height and nozzle orientation particularly if ‘drilling’ or improperly spray distribution occurs.

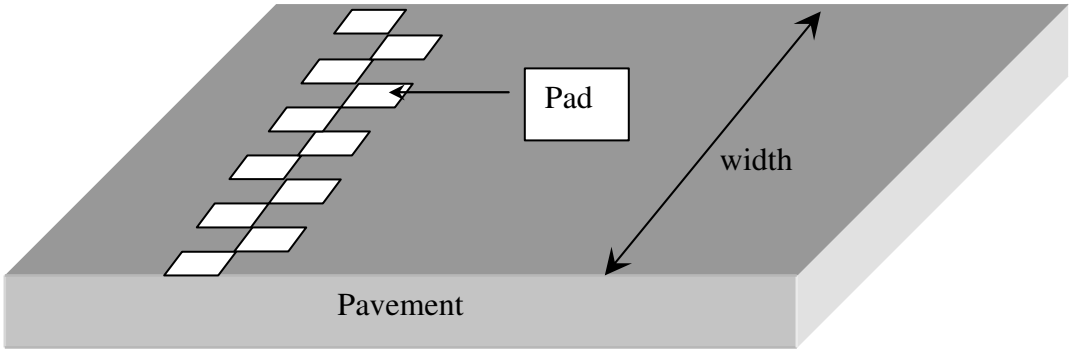

Fig. II-14. Setup of Pads on Pavement Surface

Nozzle Type

Nozzle selection is one of the most important factors affecting curing quality. The type of nozzle determines not only the amount of spray applied, but how the uniformity of the applied spray is controlled, the coverage obtained on the sprayed surfaces, and the amount of drift that can occur. Each nozzle type has specific characteristics and capabilities and is designed for use under certain application conditions.

Each type of nozzle has a specific spray angle, flow rate, spray pattern and droplet size. The most prevailing patterns are hollow cone, full cone, and flat fan, as shown in Fig. II-15. For curing compound application, a flat spray nozzle is often used.

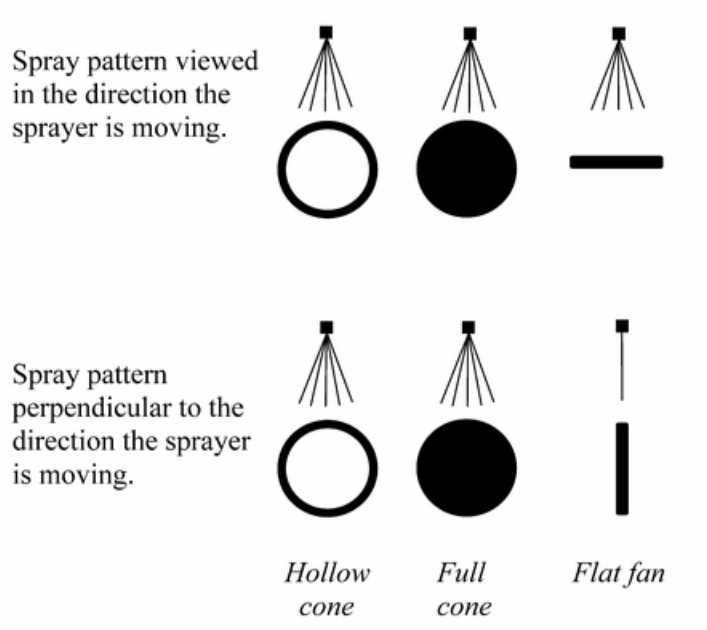

Fig. II-15. Typical Spray Patterns (Catalog 45A 1997)

Spray nozzles used for broadcast spraying do not always deliver a uniform quantity of material over the width of the spray pattern (Fig. II-16). The distribution pattern is determined by nozzle design, wear, clogging and pressure at the nozzle.

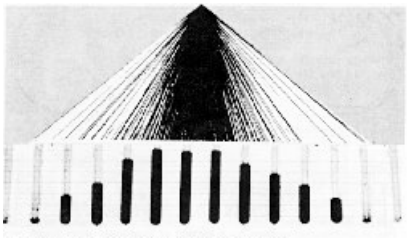

Fig. II-16. Typical Distribution (Catalog 45A 1997)

The dimension of the droplet created by nozzle is critical for successful curing application. It is hard to apply uniform coverage with large droplets; while if the droplets are too small, they increase the drift potential. Droplets with a diameter smaller than 200 microns are susceptible to drift. Nozzle manufacturers often provide volume median diameters for nozzles at different pressure. Each type of nozzle has a designated

4-digit number. The first two digits represent the spray angle in degrees and the last two represent the flow rate (gallons per minute).

Uniformity of Distribution

Nozzle spacing and boom height

As stated earlier, spray nozzles used for broadcast spraying do not deliver a uniform quantity of material over the width of the spray pattern. When a number of nozzles are spaced on the boom, the individual nozzle spray patterns must overlap to obtain more uniform distribution over the entire boom width. Nozzle manufacturers normally provide recommendations for boom height for each particular nozzle and nozzle spacing. Improper boom height will result in uneven distribution patterns (Fig. II-17). Anything that changes boom height will affect the distribution pattern.

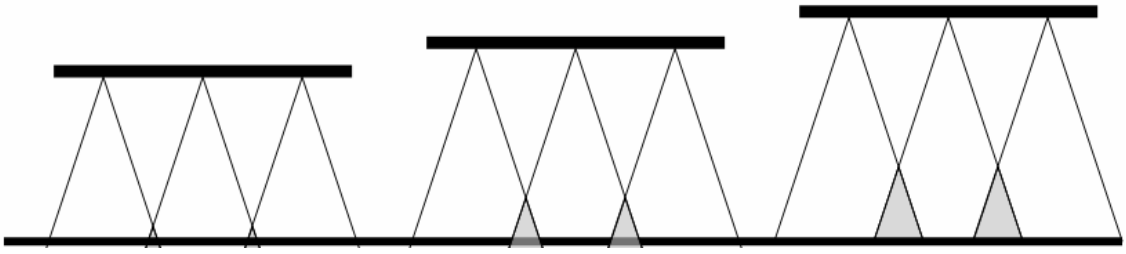

(a) Insufficient Overlap. (b) Correct Overlap. (c) Excessive Overlap.

Fig. II-17. Boom Height vs. Overlap (Catalog 45A 1997)

Effect of pressure

Pressure is another important factor that affects the distribution pattern. When pressure goes up, the size of droplets tends to decrease so that a more uniform coverage can be obtained; when pressure goes down, the size of droplets increase, which results in a less-uniform coverage. Coverage obtained is determined primarily by droplet size and the volume of material applied. As droplet size is decreased, better coverage is obtained with a given volume of material. If the diameter of spray droplets is reduced by one-half, the number of droplets produced with a given volume is increased by eight times. Conversely, doubling the diameter will reduce the number produced by eight times.

Using small droplets to achieve good coverage can result in problems due to drift. Thus, the pressure and boom height need to be mutually check to ensure uniform coverage.

Application Rate

The quantity of curing compound applied per unit of area by a sprayer depends on the shape and size of the hole (orifice) in the nozzle, pressure, nozzle spacing on the boom, and speed of travel.

Nozzle size

Nozzles are selected that deliver the correct amount of material per unit of time and desirable droplet size under certain pressure. However, during use the size of the hole in the nozzle may change rather rapidly due to wear, plugging (due to dirt or residue of the curing compound) and damage caused by trying to clean a plugged nozzle with wire, etc. The rate of nozzle wear depends on the type of material being sprayed, the amount of dirt in the water and the material from which the nozzle is made.

The Prairie Agricultural Machinery Institute in Canada has found nozzle tip wear sufficient to cause a 10 percent increase in nozzle delivery after only 50 hours of use. This is the major reason for checking the flow rate of a nozzle frequently.

Pressure

As the pressure the nozzle increases, the flow rate through the nozzle increases. The flow rate is directly related to the square root of the pressure. Thus, doubling the pressure increases the nozzle flow rate by 1.4 times; tripling the pressure increases the flow rate by 1.73 times; and increasing the pressure by four times doubles the flow rate.

Normally nozzle manufacturers publish flow rate in gallons per minute (GPM) versus pressure for their nozzles. Nozzles might not deliver the amount specified by the manufacturer, if there is an inaccurate pressure gauge. It could also be caused by the fact that the actual pressure at the nozzle is less than that indicated by the pressure gauge. Such pressure losses can be caused by restrictions in the line, buckling of supply hoses

or partially clogged nozzle strainers. Using nozzles larger than those for which the sprayer was designed may cause a reduction in pressure at the nozzle.

Nozzle spacing

If a given nozzle size, increasing spacing on the boom will reduce the application rate (typically expressed in gallons per square feet). For example, spacing nozzles (of the same size) at 40 inch intervals instead of 20 inches apart on the boom reduces the application rate by one-half.

Speed of travel

Application rate varies inversely with the cart speed. That is, if the speed of travel in miles per hour (MPH) is doubled, the application rate is reduced by one-half. If the MPH is reduced to one-half, the application rate is doubled. Thus, speed of travel is very important in obtaining the proper application rate. Otherwise, if the chosen MPH is not maintained, improper application rates result.

Calibration Procedures

The following procedures are to be followed in order to obtain a uniform distribution of the designed application rate:

First, select the proper nozzle size.

Second, determine application rate (AR).

Third, select an appropriate speed of travel.

Fourth, determine the effective spray width (W) per nozzle. For boom type sprayers, W is equal to the nozzle spacing on the boom.

Fifth, determine the cart speed to obtain the required gallons per minute (GPM) for each nozzle from the equation (II-3).

EARLY AGE CONCRETE HEAT TRANSFER AND MOISTURE TRANSPORT

The nature of the heat transfer and moisture transport in hardening concrete is a subject of great interest relative to their effects on concrete strength development and pavement slab mechanical behavior, while the curing membranes serve as the boundary conditions

for both phenomena. Well cured concrete tend to have less drying shrinkage and thermal expansion, and higher strength and maturity. Thus its understanding is the key for a realistic estimation of drying shrinkage, thermal expansion, strength, maturity and curing efficiency.

Heat Transfer

From thermodynamics theory, energy tends to spread from high potential to low potential. As far as heat transfer is concerned, temperature is the index for the thermal energy. Thus, heat will transfer from high to low temperature locations. It is useful to document the nature and theory of heat transfer relative to its effect on temperature history of hydrating concrete, since temperature history is an important factor in concrete maturity concept. The control volume in heat transfer theory is a region of space bounded by a control surface through which energy and matter may pass, as shown in Fig. II-18. If the summation of the inflow and generation of energy exceeds the outflow, there will be an increase in the amount of energy stored in the control volume, whereas there will be a decrease in energy stored in the case that the outflow of energy exceeds that summation. If the inflow and generation of energy equal the out flow, a steady-state condition must prevail in which there will be no change in the amount of energy stored in the control volume.

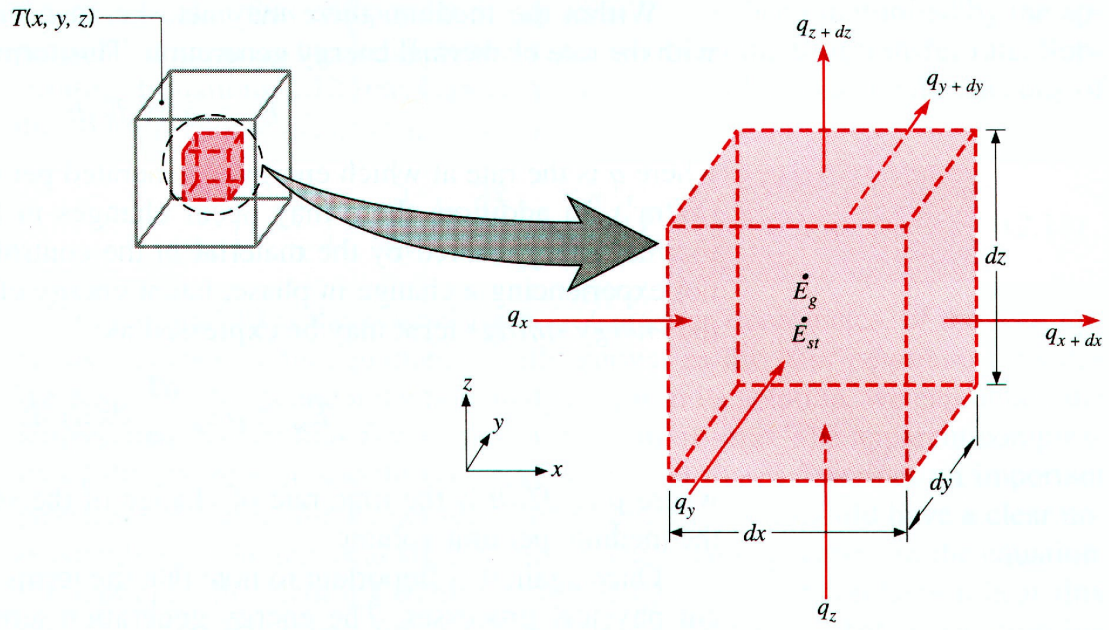

Fig. II-18. Thermal Conduction through an Infinitesimal Small Control Volume (Incropera and DeWitt 1996)

Based on the law of the conservation of energy, at any point in time the energy terms include the rate at which thermal and mechanical energy enters and leave through the control surface, $\dot{E}_{in}$ and $\dot{E}_{out}$. Also, thermal energy might be created within the control volume due to conversion from other forms of energy, as heat of hydration in the case of hardening concrete. This process is referred to as energy generation, and the rate at which it occurs is designated as $\dot{E}_g$. Thus the rate of change in energy stored within the control volume is designated as $\dot{E}_{st}$. A general form of energy conservation is expressed on a rate basis (Incropera and DeWitt 1996).

$$\dot{E}_{in} + \dot{E}_g - \dot{E}_{out} = \frac{dE_{st}}{dt} = \dot{E}_{st} \qquad \text{(II-6)}$$

Equation (II-6) may be applied at any instant of time. The alternative form for a time interval Δt is obtained by integrating equation (II-6) over time (Incropera and DeWitt 1996):

$$E_{in} + E_g - E_{out} = \Delta E_{st} \tag{II-7}$$

Equation (II-6) and (II-7) imply that the amounts of energy inflow and generation act to increase the amount of energy stored within the control volume, whereas outflow acts to decrease the stored energy.

The inflow and outflow of energy that occurs at the control surface is proportional to the surface area. Additionally, heat transfer that occurs due to conduction, convection, and radiation is involved in the energy inflow and outflow at the control surface. The energy generation term is associated with conversion from other forms of energy such as the concrete heat of hydration. As concrete hydrates, a chemical reaction takes place generating thermal energy which is dependent upon the amount and fineness of the cementitious materials used in the concrete.

Energy storage changes within the control volume due to changes in the internal, kinetic and potential energies. Hence, for a time interval, Δt, the energy storage term of equation (II-7), ΔE_{st}, can be equated to $\Delta U + \Delta KE + \Delta PE$ where kinetic and potential energy effects are neglected in heat transfer analysis. The internal energy, ΔU, consists of a sensible or thermal component, which accounts for the translational, rotational, and/or vibrational motion of the atoms/molecules comprising the matter in the control volume; a latent component, which relates to intermolecular forces influencing phase change between solid, liquid, and vapor states; a chemical component, which accounts for energy stored in the chemical bonds between atoms; and a nuclear component, which accounts for binding forces in the nucleus. Accordingly, the rate of change in energy storage in equation (II-6) due to the temperature change in the control volume can be expressed as (Incropera and DeWitt 1996):

$$\dot{E}_{st} = \frac{dU_t}{dt} = \frac{d}{dt}\left(\rho V c_p T\right) \tag{II-8}$$

where

ρ = density of mass within control volume (kg/m^3),

V = control volume (m^3), and

c_p = specific heat (W·hr/kg/^{o}K).

An infinitesimally control volume, *dxdydz*, is defined and shown in Fig. II-18. If there are temperature gradients in concrete, conduction heat will occur across each of the control surfaces. The conduction heat rates perpendicular to each control surface at the *x*, *y*, and *z* coordinate locations are indicated by the terms q_x, q_y, and q_z, respectively. The conduction heat rates at the opposite surfaces can be expressed as a Taylor series expansion by neglecting higher order terms.

$$q_{x+dx} = q_x + \frac{\partial q_x}{\partial x} dx \tag{II-9}$$

$$q_{y+dy} = q_y + \frac{\partial q_y}{\partial y} dy \tag{II-10}$$

$$q_{z+dz} = q_z + \frac{\partial q_z}{\partial z} dz \tag{II-11}$$

Within the hydrating concrete, there should be an energy source term associated with the rate of thermal energy generation.

$$\dot{E}_g = \dot{q} dxdydz \tag{II-12}$$

where $\dot{q}$ is the rate at which energy is generated per unit volume of the concrete (W/m^3). In addition, there may be changes in the amount of the internal thermal energy stored in the control volume of concrete. The energy storage term may be expressed as:

$$\dot{E}_{st} = \rho c_p \frac{\partial T}{\partial t} dxdydz \tag{II-13}$$

Equation (II-6) is transformed into equation (II-14) by applying the methodology of conservation of energy and by referring equation (II-9) to (II-13) and Fig. II-18 (Klemens 1969; Siegel and Howell 1981).

$$q_x - \left(q_x + \frac{\partial q_x}{\partial x} dx \right) + q_y - \left(q_y + \frac{\partial q_y}{\partial y} dy \right) + q_z - \left(q_z + \frac{\partial q_z}{\partial z} dz \right) + \dot{q} dxdydz = \rho c_p \frac{\partial T}{\partial t} dxdydz \tag{II-14}$$

where

$\dot{q}$ = rate of energy generation per unit volume (W/m^3), and

$\rho c_p \frac{\partial T}{\partial t}$ = rate of change of the thermal energy per unit volume (W/m^3).

The constitutive relationship between temperature gradient and heat flow at the control surface shown in Fig. II-18 can be further expressed by Fourier's law as:

$$q_x = -k_x dydz \frac{\partial T}{\partial x} \tag{II-15}$$

$$q_y = -k_y dxdz \frac{\partial T}{\partial y} \tag{II-16}$$

$$q_z = -k_z dxdy \frac{\partial T}{\partial z} \tag{II-17}$$

where k_x, k_y and k_z are the thermal conductivity (W/m/^{o}K) in x, y and z directions. Equations (II-15) to (II-17) are substituted into equation (II-14) and dividing out the dimensions of the control volume ($dxdydz$) to obtain equation (II-17) (Klemens 1969; Siegel and Howell 1981).

$$\left[\frac{\partial}{\partial x}\left(k_x\frac{\partial}{\partial x}\right)+\frac{\partial}{\partial y}\left(k_y\frac{\partial}{\partial y}\right)+\frac{\partial}{\partial z}\left(k_z\frac{\partial}{\partial z}\right)\right]T+\dot{q}=\rho c_p\frac{\partial T}{\partial t} \quad \text{(II-18)}$$

A material having thermal conductivity in different directions is anisotropic; whereas material having the same thermal conductivities in all directions is called isotropic material.

Conduction is a mode of heat transfer in which heat is transferred by random molecular motion in a concrete slab while convection represents a mode of heat transfer in which heat is transported through mixing of hot and cold fluid particles between the slab surface and a moving fluid (i.e. wind). Heat transfer by radiation represents the transmission of energy by electromagnetic waves. For concrete pavement, radiation and convection play a dominant role in transferring heat between the slab surface and the surrounding air, while conduction plays a separate role in transferring heat within the slab as shown in Fig. II-19.

Conduction

Heat conduction describes the phenomenon that heat transfer from points of higher temperature to points of lower temperature in a concrete slab. Heat energy is transferred within the slab due to interaction between the particles with high temperature and particles with low temperature. Molecules at a high temperature are said to have high energy, which makes the molecules themselves randomly translate, and internally rotate and vibrate more energetically.

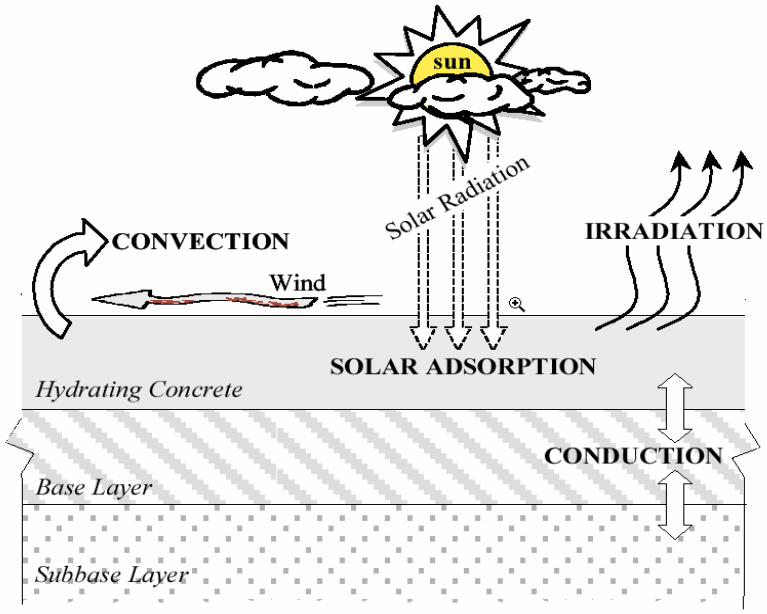

Fig. II-19. Heat Transfer Mechanisms between Pavement and Its Surroundings (Ruiz, Schindler et al. 2001)

Conduction can also be expressed by using Fourier's law in the form of a rate equation. Conduction for a temperature distribution T in one dimension can be expressed as a function of direction x as (Klemens 1969):

$$q''_{cond} = -k\frac{dT}{dx} \tag{II-19}$$

where the conductive heat flux, q''_{cond} (W/m^2), is the heat transfer rate in the x direction per unit area perpendicular to the direction of transfer. The thermal conductivity k is an important material property related to heat transfer characteristics of the concrete. The process of conduction is spontaneous and irreversible, and is related to the entropy of the concrete. The second law of thermodynamics, the governing principle behind the distribution of entropy, is used to derive the heat conduction equation. This approach has been used to estimate the temperature distribution and the associated frost action in multi-layer pavement systems (Dempsey, Herlache et al. 1986).

Convection

Heat energy is transferred from a slab surface to the surrounding environment by currents of fluid particles. In addition, this heat transfer is facilitated by random molecular motion in the fluid. In other words, convection heat transfer occurs between a flow of wind and a surface of a concrete slab when they are at different temperatures. If the temperatures between a slab surface and a wind flow differ, temperature in the fluid flow above the slab will vary from T_s at the slab surface to T_a in the flow far above the slab surface. Convection heat transfer is expressed as (Says and Crawford 1980; Kaviany 1994)

$$q''_{conv} = h_c (T_s - T_a) \tag{II-20}$$

where q''_{conv} (W/m^2) is the convective heat flux and h_c (W/m^2/^{o}K) is the convective heat transfer coefficient. The convective heat transfer coefficient is difficult to determine because of the many variables that affect it. Empirical formulae were suggested to relate convection heat transfer coefficient to wind velocity and roughness of slab surface (Branco, Mendes et al. 1992)

$$h_c = 6 + 3.7v \tag{II-21}$$

where 6 W/m^2/^{o}K represents an average slab surface roughness without wind effects. And the heat transfer coefficient increases with the increase of wind speed proportionally.

Irradiation

Irradiation transfers heat energy by electromagnetic waves while conduction and convection requires a material medium. Emissive power E (W/m^2) indicates the rate of heat energy release from a surface of a concrete slab with unit area by irradiation. The upper limit of emissive power is shown as (Incropera and DeWitt 1996)

$$E = \varepsilon\sigma T_s^4 \tag{II-22}$$

where, T_s (^{o}K)is the absolute temperature at the surface of a concrete slab and σ (=5.67×10^{-8} W/m^2/^{o}K^4) is the Stafan-Boltzmann constant. The term ε is the emissivity, which ranges from 0 to 1, is a radiative property of a slab surface and provides a measure of how efficiently the surface emits energy relative to a blackbody.

Irradiation for a concrete pavement is determined on the basis that a slab surface at temperature T_s is radiating to a much larger surface at temperature T_a surrounding the slab surface. Irradiation heat transfer can be expressed as (Meinel and Meinel 1976; Siegel and Howell 1981):

$$q_r^{"} = \varepsilon\sigma\left(T_s^4 - T_a^4\right) \tag{II-23}$$

Equation (II-23) is assumed to yield a reasonable estimate of heat exchange between a slab surface and the surrounding environment under cloudy weather conditions (Thepchatri, Johnson et al. 1977).

Solar Radiation

Solar radiation ($q_s^{"}$) absorbed directly into a concrete slab surface causes the surface of the slab to be heated more rapidly than the interior region. This effect contributes to a temperature gradient through the depth of the slab (Hsieh, Qin et al. 1989; Branco, Mendes et al. 1992). There are several factors which influence the solar radiation absorption into a given slab surface. These include the time of the day or year, the latitude, and cloudiness, and so on (Thepchatri, Johnson et al. 1977; Chapman 1982; Branco, Mendes et al. 1992). The solar radiation consists of direct and indirect components. The direct component is the solar radiation that is directly incident on the surface while the indirect radiation refers to the solar radiation resulting from multiple scattering by the environment. Accordingly, the total solar radiation that reaches the

surface of a concrete slab is the sum of direct and indirect contributions (Branco, Mendes et al. 1992):

$$q_s^{"} = \alpha\left[I_d \sin\theta + I_i\left(\frac{1+\cos\gamma}{2}\right)\right] \quad \text{(II-24)}$$

where

$q_s^{"}$ = solar radiation (W/m^2),

α = surface heat absorptivity of concrete (= 0.6),

I_d = direct solar radiation (W/m^2),

I_i = indirect solar radiation (W/m^2),

θ = incidence angle of solar radiation against the slab surface (degree), and

γ = inclination angle of slab surface (degree).

The amount of solar radiation received by the slab surface depends on the incidence angle of solar radiation against the slab surface and the inclination angle of slab surface. The incident angle of solar radiation can be determined by a method presented by Hsieh et al. (1989). The indirect solar radiation may range from 10 % of the total solar radiation on a clear day to nearly 100 % on a totally sunny day. No solar radiation absorption occurs at night since the sun's rays are no longer prevalent.

Heat Flux due to Evaporation

Including heat flux due to evaporation in the boundary condition of heat transfer at the slab top surface is important to accurately account for moisture effects on the temperature conditions at the surface of a concrete pavement. Few temperature prediction models consider the evaporation effects in their boundary conditions (Kapila, Falkowsky et al. 1997). There have been many efforts to develop concrete temperature prediction models which can be easily used although they ignore the effect of heat flux due to evaporation in their boundary conditions (Yang 1996; Ruiz, Schindler et al. 2001). Heat flux due to evaporation can be calculated by:

$$q_e^{"} = EH_v \qquad \text{(II-25)}$$

where

E = rate of evaporation (kg/m^2/hr or W/m^3), and

H_v = heat of vaporization of water

= $597.3 - 0.564T_s$ (cal/g) (Linsley et al, 1975)

= $427(597.3 - 0.564T_s)$ (m).

Moisture Transport

Drying shrinkage and creep strains are related to the amount of movement and distribution of moisture in a concrete slab. These strains are primary contributors to the warping inducted deformation of a concrete slab and formation of early aged cracks or shallow delaminations immediately below the pavement surface. In the past, a method used to determine the moisture in concrete was by actual measurement of weight loss of small laboratory samples. Recently, quantities of moisture have been indirectly measured using moisture sensors with the recent development of instrument and measurement techniques. Moisture flow and diffusion in concrete have been a significant topic in the research of concrete pavement materials (Bažant and Najjar 1972; Parrott 1988; Parrott 1991; Buch and Zollinger 1993; Xin, Zollinger et al. 1995; Jeong 2003).

In freshly placed concrete, moisture movements are typically characterized by high rates of diffusion followed by gradually lower and lower rates 10 to 12 hours after placement. This drying characteristic is inherently related to a material property referred to as the moisture diffusivity (D) which has been generally accepted to be dependent upon the pore water content within the cement paste. It has been observed that moisture diffusivity may change significantly with variations in the moisture content or the relative humidity (from 100 to 70 percent) of the concrete (Pihlajavaara 1964; Kasi and Pihlajavaara 1969; Bažant 1970; Bažant and Najjar 1972). At constant water content (w), moisture diffusivity changes little with time in mature concrete in contrast with the

dramatic changes fresh concrete undergoes during the first 24 hours after placement. In this regard, diffusivity in early-aged concrete is not only a function of humidity but also of concrete age and porosity. The moisture diffusivity is an important constitutive parameter in modeling moisture flow in hardening concrete.

The rate of moisture flow through concrete can be expressed by the velocity of flow (J) representing the mass of evaporable water passing through a unit area perpendicular to the direction of flow per unit time. The velocity of flow by Darcy's law is derived from energy gradients (Bažant and Najjar 1972):

$$J = -C \cdot grad\ \mu \tag{II-26}$$

where μ is Gibb's free energy per unit mass of evaporable water and the coefficient C characterizes the permeability of the porous of concrete. Equation (II-26) is restricted to small energy gradients and laminar flow conditions. Assuming water vapor behaves as an ideal gas, Gibb's free energy is (Bažant and Najjar 1972):

$$\mu = \left(\frac{RT}{MV_w}\right) \cdot \ln H + \mu_{sat}(T) \tag{II-27}$$

where

R = universal gas constant (8.3143 J/mol/^{o}K),

T = absolute temperature (^{o}K),

M = molecular weight of water (18.015 g/mol),

V_w = specific volume of water (1 cm^3/g),

H = humidity of concrete $\left(= \frac{RH}{100}\right)$, and

RH = relative humidity of concrete (%).

Equation (II-26) can be rewritten in terms of temperature (T) and humidity (H) of concrete as (Bažant and Najjar 1972):

$$J = -c \cdot grad\ H \tag{II-28}$$

where the coefficient c is permeability as a function of temperature and humidity of concrete as below (Bazant and Najjar 1972).

$$c = \left(\frac{RT}{MV_w}\right) \times \left(\frac{C}{H}\right) \tag{II-29}$$

The relationship between humidity and water content within concrete at a constant temperature and the degree of hydration is described by desorption or sorption isotherms (Bazant and Najjar 1972). It is evident that the relationship between the moisture and the measured humidity of concrete will vary as a function of the age. The dependence of the evaporable water content on humidity (as a function of temperature) is a function of the porosity of the pore structure within the cement paste and is represented empirically in the form of desorption or sorption isotherms that are illustrated in Fig. II-20.

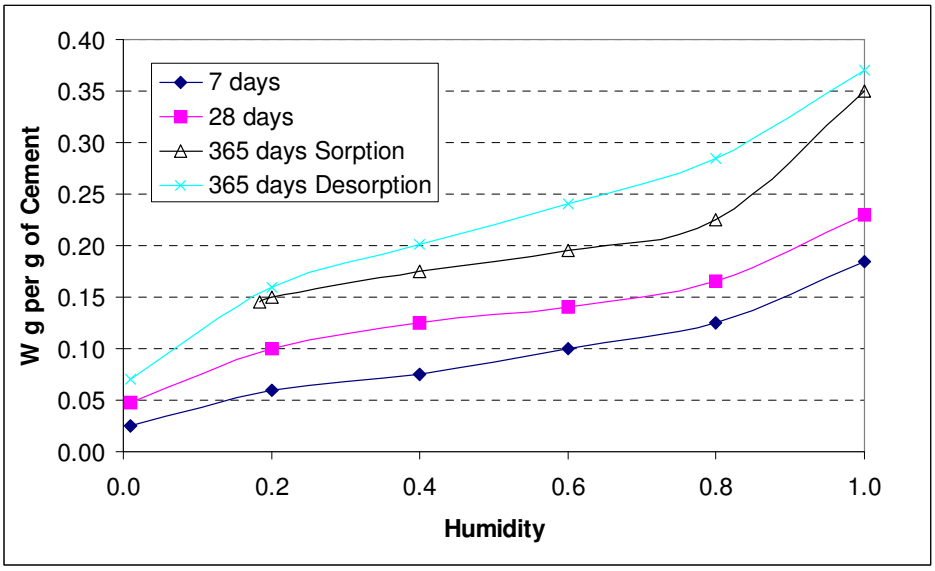

Fig. II-20. Desorption-Isotherms (Bažant 1970)

It should be noted that the isotherm for sorption is different from the isotherm for desorption. This characteristic may be due to the various states of equilibrium of the pore water. An investigation by Parrott (1988) implied the significance of porosity with respect to the position of the desorption or sorption isotherm within concrete. The results indicated that a greater amount of moisture loss in drying concrete would occur in regions nearest to exposed drying surfaces which may be also regions of greater porosity. This observation was proven in the relationship between weight loss and relative humidity of concrete indicated in Fig. II-21. Therefore, it can be explained that there is a greater volume of coarse pores at positions nearer to an exposed concrete surface and consequently the relationship between weight loss and relative humidity of concrete will vary with distance from the exposed surface. In this respect, the performance and behavior of a concrete pavement may be affected by the porosity of the surface. It should also be noted that the resulting desorption isotherm at any time during hydration of hardening slab concrete must be interpreted not only as a function of the degree of hydration, but also as a function of porosity. At a given porosity, the desorption isotherm may be expressed in the differential form as (Bažant and Najjar 1972):

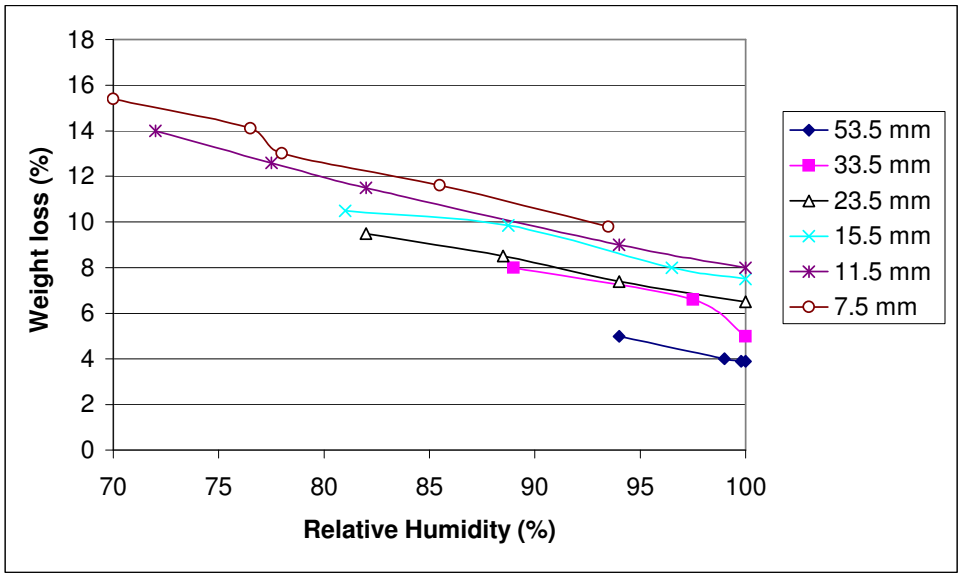

Fig. II-21. Weight Loss versus Relative Humidity of Drying Concrete at Various Vertical Distances from the Exposed Surface (Parrott 1988)

$$dH = kdw \tag{II-30}$$

$$k = \left(\frac{\partial H}{\partial w}\right)_w \tag{II-31}$$

where the parameter k represents the slope of the moisture isotherm where the mass of water (w) is described as a function of humidity (H). Moisture movements in an unsaturated porous medium are effected by temperature profiles of the medium. Thus, the calculation of humidity in hydrating concrete requires additional terms under variable temperature conditions as (Bažant and Najjar 1972):

$$dH = kdw + KdT + dH_s \tag{II-32}$$

where

K = hygrothermic coefficient ($= \left(\frac{\partial H}{\partial T}\right)_w$), and

dH_s = change in humidity (H) due to hydration at a constant water content (w) and time (t) .

The hygrothermic coefficient represents the change in humidity due to one degree of change in temperature at constant water content and a given level of hydration. It should be noted that the pore water content (w) includes both the evaporable or capillary water (w_c) and the non-evaporable water (w_n) per unit volume of materials.

Based on conservation law, the rate of moisture flow in unit volume of concrete is determined from (Bažant and Najjar 1972):

$$\frac{\partial w}{\partial t} = -divJ \tag{II-33}$$

Substituting equation (II-28) into equation (II-33) and subsequently substituting equation (II-33) into equation (II-32) leads to (Bažant and Najjar 1972):

$$\frac{\partial H}{\partial t} = k \cdot div(c \cdot gradH) + \frac{\partial H_s}{\partial t} + K\frac{\partial T}{\partial t} \qquad \text{(II-34)}$$

which is the diffusion equation for the drying concrete under variable temperature conditions. Equation (II-34) is further developed to be equation (II-35).

$$\frac{\partial H}{\partial t} = kc\frac{\partial^2 H}{\partial x^2} + k\frac{\partial c}{\partial x}\frac{\partial H}{\partial x} + \frac{\partial H_s}{\partial t} + K\frac{\partial T}{\partial t} \qquad \text{(II-35)}$$

Permeability (c) is also a function of the porosity and indirectly a function of position x. Because permeability change with position x is assumed to be very small, the second term in the equation (II-35) is considered to be negligible and is consequently dropped from the diffusion equation as:

$$\frac{\partial H}{\partial t} = D\frac{\partial^2 H}{\partial x^2} + \frac{\partial H_s}{\partial t} + K\frac{\partial T}{\partial t} \qquad \text{(II-36)}$$

where D (= $k \cdot c$) is moisture diffusivity (L^2/t).

Parrot (1988) studied the factors for RH in concrete by evaluating the effects of w/c ratio, cement type, moist curing time, and exposure condition on time-dependent relative humidity in drying concrete. The specimens used for the study were made using various cement types and w/c ratio and sealed to ensure uniaxial exposure. Cubes with 100mm were used to measure the relative humidity (RH) and cured for 1, 3, 28 days before exposure. The RH was measured through the cavities located at various distances form the exposed faces of the cube. The specimens were exposed under three types of conditions, i.e. 1) under laboratory conditions where RH was 58% and temperature was 20ºC, 2) under outdoor conditions consisting of RH ranging from 58-90%, and temperature ranging from 6-21ºC and rainfall ranging from 40-70mm/month or sheltered

from rainfall, and 3) under the indoor conditions where RH was not controlled and temperature was 15-25ºC.

The test results indicated that the effects of w/c ratio and curing time are small on the time-dependent RH of the concrete. The cement type and exposure conditions have significant effects. The concrete made with cement binder materials, such as pulverized fuel ash (PFA) and ground granulated blastfurnace slag (ggbs), were dried faster than the one made with only Portland cement (OPC). However, the RH in concrete with 5% filler dropped more slowly than that in concrete with OPC. From the result of the above tests, the RH results from for lab testing can be represented by a set of equations.

$$\text{Normalized RH } f(r) = (r - r_a)/(100 - r_a) = e^{-kT} \quad \text{(II-37)}$$

where

r = relative humidity,

r_a = ambient relative humidity,

$k = 0.8 - 0.14T + 0.01T^2$,

T = Normalized drying time, $t/t_{1/2}$,

t = drying time, and

$t_{1/2}$ = the time to reach 79% RH (to reach half of the potential RH change).

The $t_{1/2}$ is changed by the cement binder materials and represents followings:

$$t_{1/2} = 10jd \quad \text{for } t_{1/2} < 414 \text{ days} \quad \text{(II-38)}$$

$$t_{1/2} = 3jd + 290 \quad \text{for } t_{1/2} \geq 414 \text{ days} \quad \text{(II-39)}$$

where j = 1.00 for OPC, 0.56 for PFA, and 0.53 for ggbs

At given combination of depth and drying time, the relative humidity can be calculated using the equations above.

The tests under the indoor and outdoor exposure conditions show different results with those under the lab conditions. The RH of concretes exposed to the outdoor environment is not significantly affected by the distance from the exposed surface; however, under the indoor conditions, the drying is slower at a greater depth. Especially, the RHs of concrete sheltered from rain were low but those of concrete exposed rainfalls were higher.

Evaporation Model

Available moisture in hardening concrete evolves into two types - one referred to as evaporable water held in both capillary and gel pores (including interlayer pores) and the other as non-evaporable water combined structurally in the concrete hydration products (Mindess and Young 1981; Neville 1996) as shown in Fig. II-22. The sum of these portions equals the total water content in the paste. Water available in the capillary pores evaporates through the surface of the concrete when it is exposed to ambient weather conditions which typically cause a decrease in vapor pressure above the concrete surface. Because the predominance of moisture movement associated with evaporation occurs near the surface of the concrete and due to the low moisture diffusivity of hardened concrete, moisture variations within the cross-section of the concrete are found mostly near the surface.

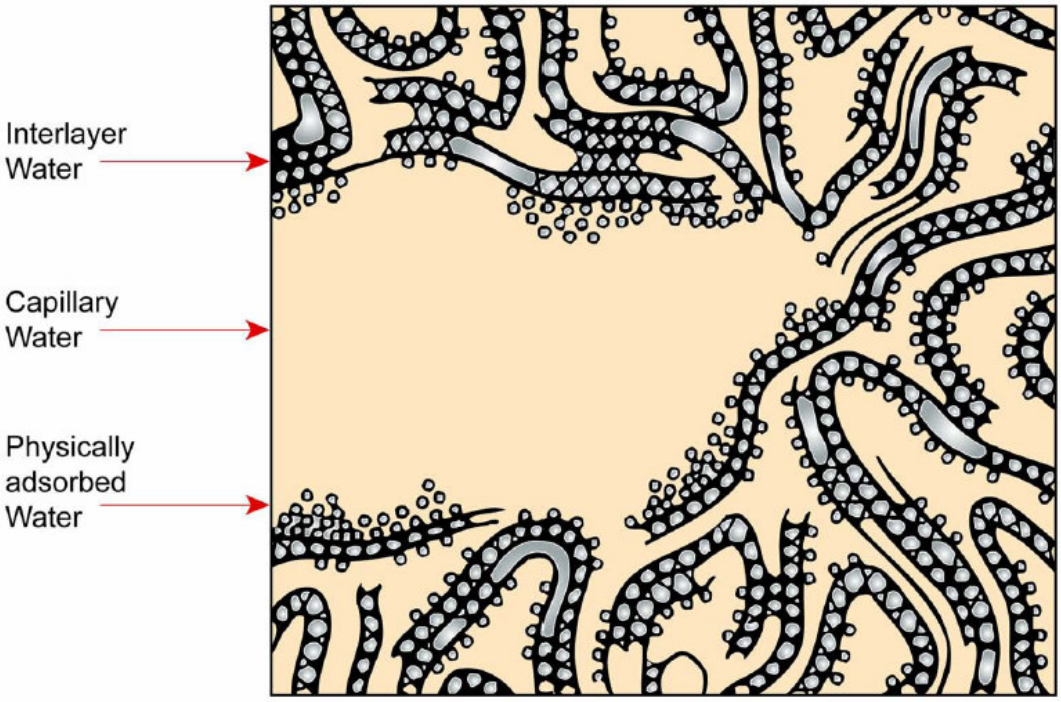

Fig. II-22. Structure of Hydrated Silicates (Mehta and Monteiro 2006)

Evaporation at the surface of a concrete slab can be defined as the net rate of vapor transport to the surrounding atmosphere (Linsley, Kohler et al. 1975). This change in state requires a heat exchange of approximately 600 calories for each gram of water evaporated. Vaporization removes heat from bleed water near the surface of the concrete slab and thus cools the concrete. Therefore, evaporation is another important factor to be considered in the analysis of thermally induced effects on a concrete slab in addition to conduction, convection, and radiation (Kapila, Falkowsky et al. 1997).

Evaporation is controlled by use of the appropriate curing method to minimize potential for undesirable cracking and deformation at early ages. The presence of water serves to enhance both hydration and strength development. As hydration advances and fills the water-filled space in the capillary pores(Powers 1947), capillary porosity continues to decrease and the amount of the gel pores increase. Gel pores tend to limit the movement of moisture through the capillary pores. Thus, the increase of hydrated

products and reduced capillary porosity reduces the rate of evaporation by lowering the concrete moisture diffusivity. Drying shrinkage, due to evaporation, which leads to cracking or warping is also controlled by minimization of water loss from capillary pores (Mindess and Young 1981; Neville 1996). Strength of concrete is affected not only by the total moisture content but also by the moisture variations in the concrete. For an example, test data have indicated that even a short period of drying causes a recognizable decrease in the magnitude of tensile strength of the concrete due to the moisture variation at the concrete surface (Walker and Bloem 1957).

Numerous efforts have been made to develop empirical models to express evaporation as a function of atmospheric factors (Penman 1948; Thornthwaite 1948; Menzel 1954; Veihmeyer 1964). Most of the models are of the Dalton type and have been presented in the form of (Dalton 1802):

$$E = (e_s - e_d) f(v) \tag{II-40}$$

where

E = rate of evaporation ($ML^{-2}T^{-1}$),

e_s = saturation vapor pressure of water surface (ML^{-2}),

e_d = vapor pressure of air above water surface (ML^{-2}),

$f(v)$ = wind function,

v = wind speed (LT^{-1}),

M = mass,

L = length, and

T = time.

The ACI nomograph (1996) shown in Fig. II-7 was based on the Menzel's model (1954) derived from the Dalton's model (1802) and the Lake Hefner test results conducted between 1950 and 1952 (Kohler, Nordenson et al. 1955). The Menzel's model, equation (II-41), has been accepted as one of the best methods for predicting

evaporation of bleed water while it is exposed on the surface of the concrete (which inherently excludes the consideration of curing media).

$$E = 0.44(e_s - e_d)(0.253 + 0.096v) \tag{II-41}$$

Since the quantified net radiation was not measured during the Lake Hefner tests (Kohler, Nordenson et al. 1955), this model, however, fails to consider the effects of radiation on evaporation. Another shortcoming is related to vapor pressure effects, which can be overcame by considering the many equations that have been suggested to express vapor pressure as a function of temperature (Tetens 1930; Murray 1967; Dilley 1968). Another widely used method for evaporation prediction is Penman's model (Penman 1948). Penman's model, shown in equation (36), is also a Dalton's type model but resolves the difficulties associated with them relative to wind and surface vapor pressure effects. This model predicts evaporation by considering both net radiation and aerodynamic effects.

$$E = \frac{\Delta E_q + \gamma E_a}{\Delta + \gamma} \tag{II-42}$$

where

Δ = slope of the saturation vapor pressure versus temperature curve (ML^{-2})

$= \frac{e_s - e_a}{T_s - T_a}$,

e_a = saturation vapor pressure of air (ML^{-2}),

T_s = surface temperature,

T_a = air temperature,

E_q = rate of evaporation due to net radiation ($ML^{-2}T^{-1}$),

γ = psychrometric constant (ML^{-2}), and

E_a = rate of evaporation due to aerodynamic effects ($ML^{-2}T^{-1}$).

Both the ACI nomograph and Penman's model are based on evaporation from a water surface but fail to consider the effects of changes of moisture within the concrete with time, and consequently cannot accurately predict evaporation from concrete (particularly, beyond the cessation of bleeding). Therefore, these models are only suitable while concrete is still fresh. Once concrete is hardening, they can not predict the evaporation any more.

Another model by Incropera and Dewitt (1996) suggests that the rate of evaporation is governed by the difference between vapor pressure at the surface of concrete and the vapor pressure of the ambient air. This boundary effect is represented mathematically as:

$$E = \frac{M_A h}{R \rho c_p Le^{2/3}} \left[\frac{p_{A,s}}{T_s} - \frac{p_{A.\infty}}{T_\infty} \right] \qquad \text{(II-43)}$$

where

E = evaporation rate (kg/m^2/hr),

M_A = molecular weight of water (= 18 kg/kmol),

h = convection coefficient (W/m^2/^{o}K, kg/m/hr/^{o}K),

R = gas constant (= 8.315 kJ/kmol/^{o}K),

ρ = density of air (kg/m^3),

c_p = specific heat of air (1.005 kJ/kg/^{o}K),

Le = Lewis number, the ratio of the thermal and mass diffusivities,

$p_{A,s}$ = vapor pressure at the surface of concrete (kJ/m^3),

$p_{A,\infty}$ = vapor pressure of ambient air (kJ/m^3),

T_s = concrete temperature at the surface of concrete (^{o}K),

T_∞ = concrete temperature of ambient air (^{o}K),

q_e'' = heat flux due to evaporation (W/m^2), and

h_{fg} = heat of vaporization of water (cal/g, kJ/kg, m).

In the moisture evaporation process, it can be demonstrated that radiation is by far the most important factor. Theory and wind tunnel experiments have shown that the evaporation from water of a specified temperature is proportional to wind speed and is highly dependent on the vapor pressure of the overlying air. The temperature of freshly placed concrete is not independent of wind speed and vapor pressure. The maximum rate of evaporation of water (g/ cm^2·sec) is expressed in equation (II-44) (Jones 1991).

$$v_{max} = 0.0583 p \sqrt{18/T} \qquad \text{(II-44)}$$

where

p = staruation vapor pressure, mm of mercury, and

T = ºK

Under these conditions, at 20 ºC water would evaporate at the rate of 0.253 g/cm^2·sec. In reality, the evaporation rate of water is smaller by a factor of 100,000 to 1,000,000(Jones 1991). de Boer (1953) considered that the slow actual rate of evaporation is due to the fact that there is a thin gas layer over the liquid surface in which the water vapor pressure is near saturation. The slow diffusion of the water vapor from this layer into the air above was thought to mainly govern the actual rate of evaporation. A number of researchers (Jones and Wexler 1960; Gates and Benedict 1963; Gates, Vetter et al. 1963; Gates 1965; Shiba and Ueda 1965; Jones 1969) tried to measure this thin gas layer. Gates et al. (1963) used a microwave refractometer to make measurements of the moisture profile above a water surface. Their plot of water vapor pressure against distance shows an exponential decrease in water vapor pressure with distance. Shiba and Ueda (1965) used a resistance electric hygrometer to measure the humidity distribution near the surface. Jones (1960; 1969) used a miniature barium fluoride humidity element in the preliminary investigation of the distribution of water vapor above a free water surface. During the experiments, the room temperature varied between 24.3 and 25.0 ºC and the room relative humidity was 15%. The results are plotted in Fig. II-23.

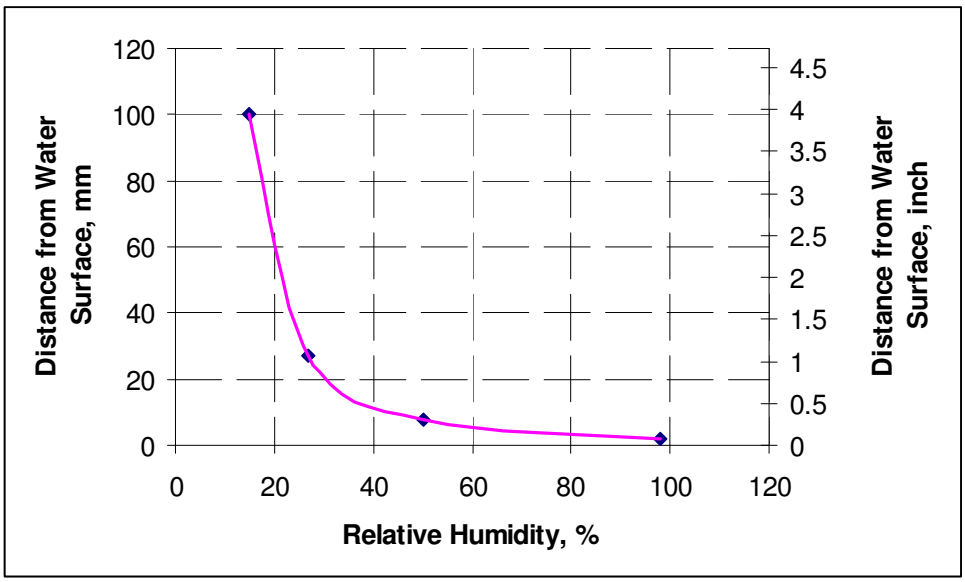

Fig. II-23. Water Vapor Profile above Water Surface(Gates, Vetter et al. 1963)

Based on these findings, the wind effect on evaporation could be explained such a way that wind tends to destroy the gas layer so that the vapor pressure difference is enlarged between the water surface and the air right above it. If the wind speed were suddenly increased, the evaporation rate would increase momentarily. This increased rate of evaporation would immediately begin to extract heat from the concrete surface at a more rapid rate than it could be replaced by radiation and conduction. The temperature of concrete surface would approach a new, low equilibrium value, and evaporation would diminish accordingly. All of the meteorological factors mentioned above should be contained in a model for evaporation.

Up to this point, a thorough review on evaporation from water surface has been made. A further effort made by Jeong (2003) was trying to simulate the evaporation from the concrete surface over the period of concrete hardening. His evaporation model is based upon the Penman's model (1948). Both net radiation and aerodynamic effects are considered in the new model in the same way as in the original Penman's model. As further described below, many constituents in the original model are replaced with other

expressions and concrete properties with respect to moisture loss; each are considered and included to formulate the new model to provide more accurate and simpler to understand prediction.

$$E = \delta \frac{Q_s}{H_v} + J \tag{II-45}$$

where

E = rate of evaporation from concrete due to both net radiation and aerodynamic effects (kg/m^2/hr),

δ = calibration factor for moisture condition of concrete surface,

Q_s = solar radiation absorption through electromagnetic waves (kg/m/hr)

$= \alpha\left[I_d \sin\theta + I_i\left(\frac{1+\cos\gamma}{2}\right)\right]$ (Branco, Mendes et al. 1992),

α = surface heat absorptivity of concrete (= 0.6) (Chapman 1982),

I_d = direct solar radiation (kg/m/hr),

I_i = indirect solar radiation (kg/m/hr),

θ = incidence angle of solar radiation against the slab surface (degree)

γ = inclination angle of slab surface (degree),

H_v = heat of vaporization (heat removed from water on the surface of concrete slab being vaporized)

$= 597.3 - 0.564T_s$ (cal/g) (Linsley, Kohler et al. 1975)

$= 427(597.3 - 0.564T_s)$ (m),

J = rate of evaporation from concrete due to convective heat transfer, irradiation, and aerodynamic effects (kg/m^2/hr)

$= B \ln\frac{H_s}{H_a}$ (Bažant and Najjar 1972),

B = surface moisture emissivity,

H_s = surface relative humidity, and

H_a = ambient relative humidity.

Key parameters of the modified model are described and further elaborated below. The rate of evaporation (E) consists of two components, one due to aerodynamic effects (E_a) explained as the rate of evaporation of a saturated vapor immediately above the water surface (Penman 1948) and the other due to energy effects (E_q). The net radiation (Q_n), which represents the energy exchange at concrete surface, consists of the elements such as solar radiation, convective heat transfer, and irradiation as:

$$Q_n = Q_s - Q_c - Q_r \tag{II-46}$$

where

Q_n = net radiation at concrete surface (kg/m/hr),

Q_s = solar radiation absorption (kg/m/hr),

Q_c = heat flux due to convection (kg/m/hr),

= $h_c(T_s - T_a)$ (Branco, Mendes et al. 1992)

h_c = convective heat transfer coefficient

= $6 + 3.7v$ (W/m^2/^{o}C) (Branco, Mendes et al. 1992)

= $367(6 + 3.7v)$ (kg/m/hr/^{o}C),

Q_r = heat energy from high to low temperature body (kg/m/hr)

= $\varepsilon\sigma(T_s^4 - T_a^4)$ (Incropera and DeWitt 1996)

= $\varepsilon[4.8 + 0.075(T_a - 5)](T_s - T_a)$ (Branco, Mendes et al. 1992),

ε = surface heat emissivity of concrete (= 0.88) (Chapman 1982), and

σ = Stefan-Boltzmann constant (= 5.67×10^{-8} W/m^2/^{o}K^4 = 2.08×10^{-5} kg/m/hr/^{o}K^4) (Chapman 1982).

Jeong (2003) further characterized B term as functions of effective curing thickness (ECT) and wind speed (v) during and after bleeding, respectively.
During bleeding:

$$B = a + b\exp(-ECT) + cv^2 \quad \text{(II-47)}$$

After bleeding:

$$B = d + \frac{e\ln ECT}{ECT} + fv^{2.5} \quad \text{(II-48)}$$

where the unit of surface moisture emissivity is kg/m^2/hr, effective curing thickness is cm, and wind speed is m/s.

CONCRETE SLAB CURLING AND WARPING

Curling and warping are important concrete slab behavior. Normally concrete curling is referred as the deflection due to temperature gradient, while concrete warping is due to moisture gradient. The objective of curing is to let concrete develop its potential strength and durability. Properly cured concrete has denser structure and less porosity, which mitigate the environmental impacts on concrete pavements. Thus small temperature and moisture gradients are expected in well cured concrete. Under smaller internal strains, concrete slabs produce less stresses, which would in turn prolong the service life of concrete pavements.

When temperature at the slab top is higher than that at the slab bottom, concrete slab exhibits a concave shape and this gradient is call positive gradient Fig. II-24 (a); when temperature at the slab at the slab top is lower than that at the slab bottom, concrete slab exhibits a convex shape and this gradient is called negative gradient Fig. II-24 (b).

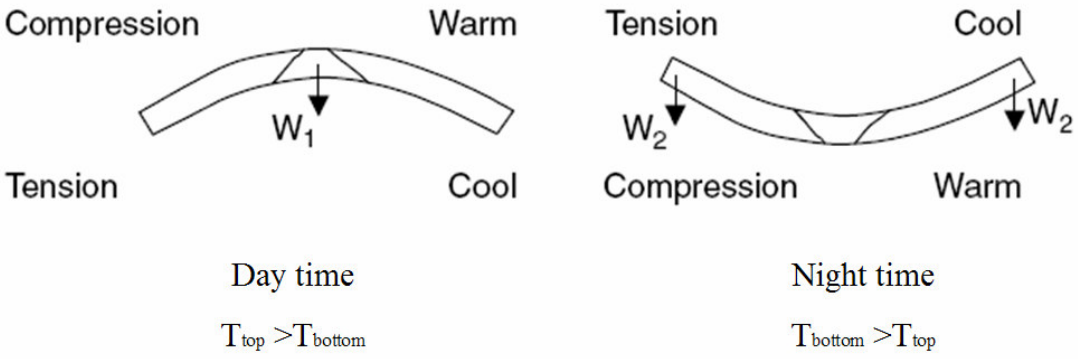

(a) Positive Temperature Gradient (b) Negative Temperature Gradient

Fig. II-24. Diagram of Concrete Slab Curling (Fwa 2006)

Generally speaking, concrete slab tends wet and to dry from the concrete surface and below according to the ambient daily high-low moisture cycle. Thus, moisture gradient is more likely to cause concrete slab to bend convexly.

The earliest concrete slab curling investigation was conducted at the Bates Experimental Road in 1922, which revealed that temperature variation between the top and bottom of concrete slab caused significant curling. Theoretically, Westergaard (1926; 1927) derived the solution for the deflection and stress due to temperature variation. His derivation was based on the assumptions that the temperature variation is linear, the slab is infinite in both length and width and the slab is in full contact with the subgrade. Based on the solution by Westergaard (1926; 1927), Bradbury (1938) superposed the solution for an infinite strip with width x and that for another strip with width y so as to obtain a solution for a slab with finite x and y dimensions. This solution is widely used today in rigid pavement design for curling stress analysis. The formulae for stresses at center of the slab, mid-point of the longitudinal edge of the slab, and mi-point of the transverse edge of the slab are presented in equations from (II-49) to (II-52).

$$(\sigma_x)_{\text{center}} = \frac{E\alpha_t\Delta_t}{2(1-\mu^2)}(C_x + \mu C_y) \qquad \text{(II-49)}$$

$$(\sigma_y)_{\text{center}} = \frac{E\alpha_t\Delta_t}{2(1-\mu^2)}(C_y + \mu C_x) \quad \text{(II-50)}$$

$$(\sigma_x)_{\text{edge}} = \frac{E\alpha_t\Delta_t}{2} C_x \quad \text{(II-51)}$$

$$(\sigma_y)_{\text{edge}} = \frac{E\alpha_t\Delta_t}{2} C_y \quad \text{(II-52)}$$

Where

$(\sigma_x)_{\text{center}}$ = slab-center curling stress in x direction,

$(\sigma_y)_{\text{center}}$ = slab-center curling stress in y direction,

$(\sigma_x)_{\text{edge}}$ = slab-edge curling stress in x direction,

$(\sigma_y)_{\text{edge}}$ = slab-edge curling stress in y direction,

E = the elastic modulus of concrete,

α_t = the coefficient of thermal expansion of concrete,

μ = the Poisson's ratio of concrete,

Δ_t = the difference between the temperatures at top and bottom of the slab, and

C_x, C_y = coefficients determined from Fig. II-25.

In Fig. II-25, ℓ is the radius of relative stiffness which is given below as.

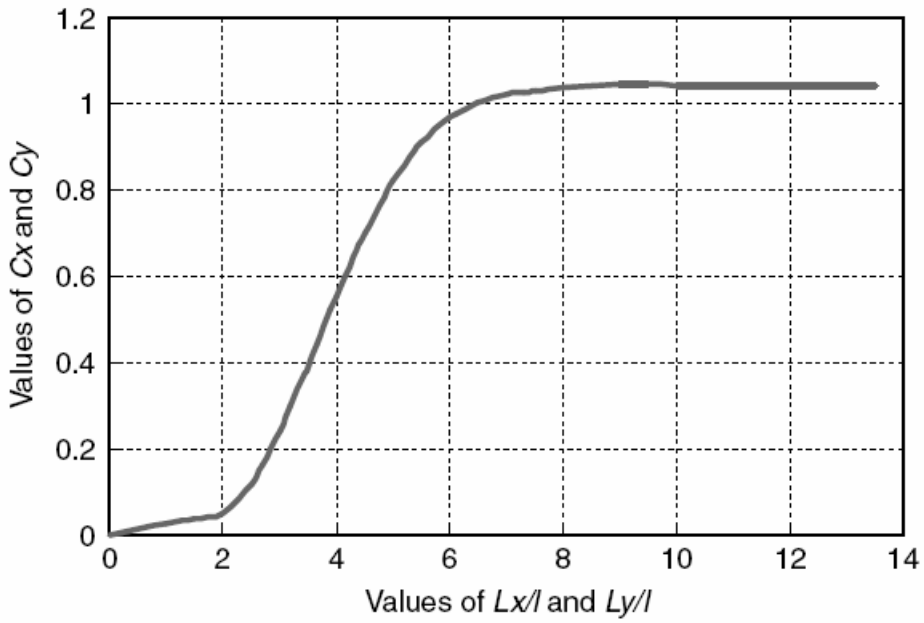

Fig. II-25. Curling Stress Coefficient (Fwa 2006)

$$\ell = \left[\frac{Eh^3}{12\left(1-\mu^2\right)k} \right]^{\frac{1}{4}} \tag{II-53}$$

where

h = the thickness of concrete slab, and

k = the modulus of subgrade reaction.

Teller and Sutherland (1935) reported, based on the measurements in concrete pavements, that temperature distributions through the thickness of concrete slab are highly nonlinear. The top quarter of the slab had a relatively large temperature variation and the temperature change within the bottom part of the slab was more gradual. Choubane and Tia (1992) showed that for some cases the linear temperature profile assumption could lead to errors of 30% or more.

ISLAB2000, a finite element program based on thick plate theory (Reissner 1945), is able to compute curling stresses due to nonlinear temperature profile. Zhang et

al. (2003) developed a closed-form theoretical solution for slab resting on a Winkler foundation or Pasternak foundation (Pasternak 1954). The nonlinear temperature profile was divided into three components as shown in Fig. II-26. The resultant curling stress in pavement is the sum of the stresses due to those three components.

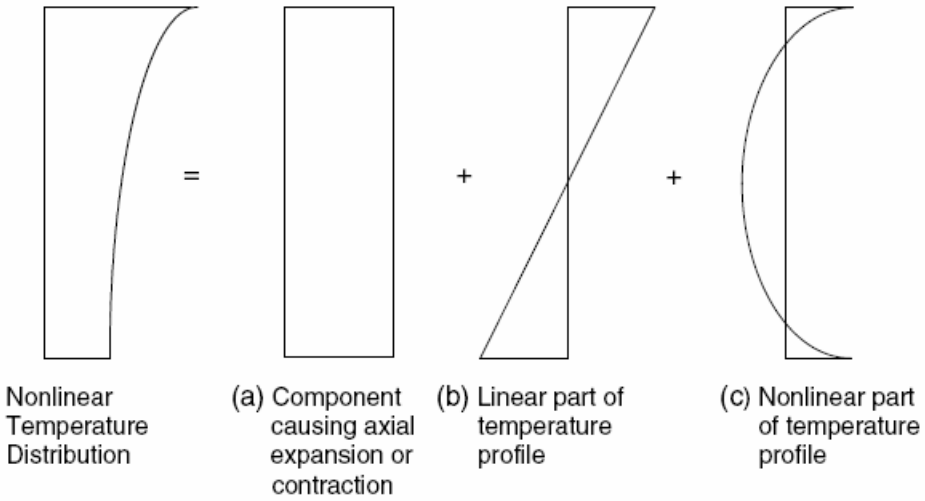

Fig. II-26. Decomposition of Nonlinear Temperature Profile (Fwa 2006)

Some researchers (Wu and Larsen 1993; Choubane and Tia 1995) used 3 dimensional isotropic finite elements to analyze the stresses due to nonlinear temperature profiles. However, the results are highly dependent on the mesh.

CHAPTER III
LABORATORY EVALUATION OF CURING EFFECTIVENESS

Ensuring sufficient water availability in hydrating concrete is of great importance to produce delamination resistant concrete for both short-term and long- term performance of concrete pavement. Excessive early-age evaporation from the surface of concrete pavement results in high porosity concrete, delamination, and low strength.

As stated in previous chapters, current laboratory curing effectiveness evaluation protocol has certain defects that limit complete engineering of the curing process or its sensitivity to different ambient conditions. In this chapter, a new laboratory curing membrane effectiveness evaluation protocol is presented. This protocol has the capability to guide field curing practice. A specified application rate should be applied to achieve a certain level of curing effectiveness as a function of the ambient weather conditions and type of curing compound used in the field. Since construction weather conditions can be rather variable, a variant application rate needs to be applied as it would apply to different conditions, which requires more fundamental approach to curing compound characterization.

LAB TEST PROTOCOL

Curing is an important activity to produce delamination free concrete pavements. Properly conducted curing ensures the potential for young concrete to gain strength and durability. On the contrary, improper curing can result in low strength at the evaporative surface and drying shrinkage induces damage as well as delamination and spalling. Factors that affect curing quality fall into two categories. One is related to the quality of the curing compound, and the other is related to the quality of the concrete. One aim of the laboratory protocol is to provide a means of ranking curing effectiveness based on the quality of the curing compound.

The laboratory-based test protocol consists of test procedures, analysis, and curing compound effectiveness evaluation as shown in Fig. III-1. A curing monitor

system and a high accuracy weighing scale are used to monitor the weight of mortar specimen consisting of a height of 2 inches and a diameter of 12 inches. Weight loss, relative humidity and temperature at three locations (ambient, surface and concrete) are recorded. The evaporation rate and the effective curing thickness (ECT) are described under the heading of "Theoretical Basis". Based on calculated results, curing compound performance under lab conditions is ranked; as well related to its ingredients; furthermore the regressed evaporation model can be used for field evaluation of a curing compound.

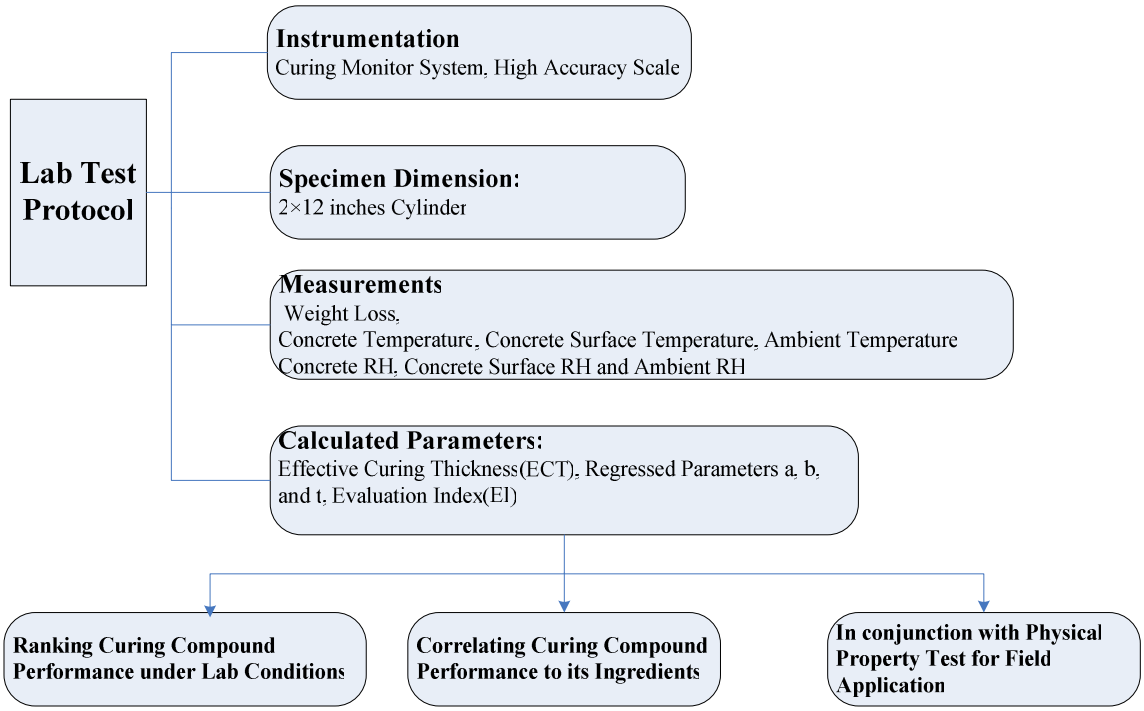

Fig. III-1. Diagram of Lab Test Protocol

Test Design

Moisture loss of concrete pavement is typically only manifest within the top inch of a concrete surface. A cylindrical mold with an inside diameter of 12 inches and a height of 1.5 inches, and a set of weighing scales with 0.1 gram accuracy are used along with the curing monitor system (CMS). The mold consists of 0.5 inch thick PVC wall and an

end plate with a thickness of 0.25 inch. Fig. III-2 shows the entire test setup for the proposed protocol.

The occurrence of evaporation is mainly due to the vapor pressure difference between air and concrete surface. The bigger the difference, the faster the evaporation rate is. Wind can continuously replace the saturated air near the evaporating surface with less saturated air, which increases the vapor pressure difference and evaporation rate. Ambient relative humidity is a direct indicator of the ambient water vapor pressure. The lower the ambient relative humidity, the lower the ambient water vapor pressure and the larger the vapor pressure difference across the membrane leading to a higher evaporation rate. Temperature increases the saturated vapor pressure level and the relative differences in vapor pressure. If the water vapor pressure in the air remains the same, the increased concrete temperature would decrease the vapor pressure difference which decreases the evaporation rate. For consistency purposes, the test is carried out under standard conditions, shown in Table III-1.

Fig. III-2. Laboratory Test Setup

Since (1) weight loss (2) concrete relative humidity and temperature near the evaporative surface, (3) concrete surface relative humidity and temperature, (4) ambient

relative humidity and temperature are recorded, the evaporation rate can be calculated, as well as the hourly ECT.

Table III-1. Standard Testing Conditions

Wind Speed	**Ambient Relative Humidity**	**Water/Cement Ratio**	**Application Rate**
10 mph	30%	0.40	180 ft^2/gallon

Instrumentation

Weight loss data and relative humidity data are two primary test measurements. A weighing scale, shown in Fig. III-3, with 0.1 gram accuracy was used. The CMS device is manufactured by A-Tek Co. in Dallas, TX. The detailed view of all the sensors is in Fig. III-4. It has three relative humidity sensors arranged to measure ambient relative humidity, concrete surface humidity and concrete relative humidity. the concrete RH sensor is a chilled mirror hydrometer type, sometimes called an optical condensation hygrometer, is the most accurate, reliable, and fundamental hygrometer commercially available. As a result, it is widely used as calibration standard. Since the moisture state inside young concrete is mostly saturated, the chilled mirror hygrometer is the most suitable sensor to measure the relative humidity inside concrete. Recent modifications of the CMS has added the capacity to monitor wind speed and solar radiation, which are another two important factors to affect evaporation and curing quality. Those two sensors are also shown in Fig. III-4.

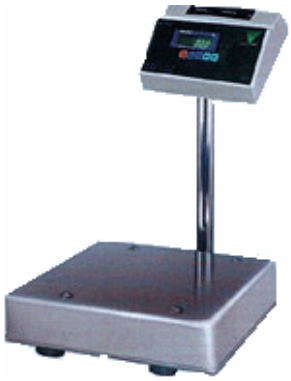

Fig. III-3. Weighing Scale

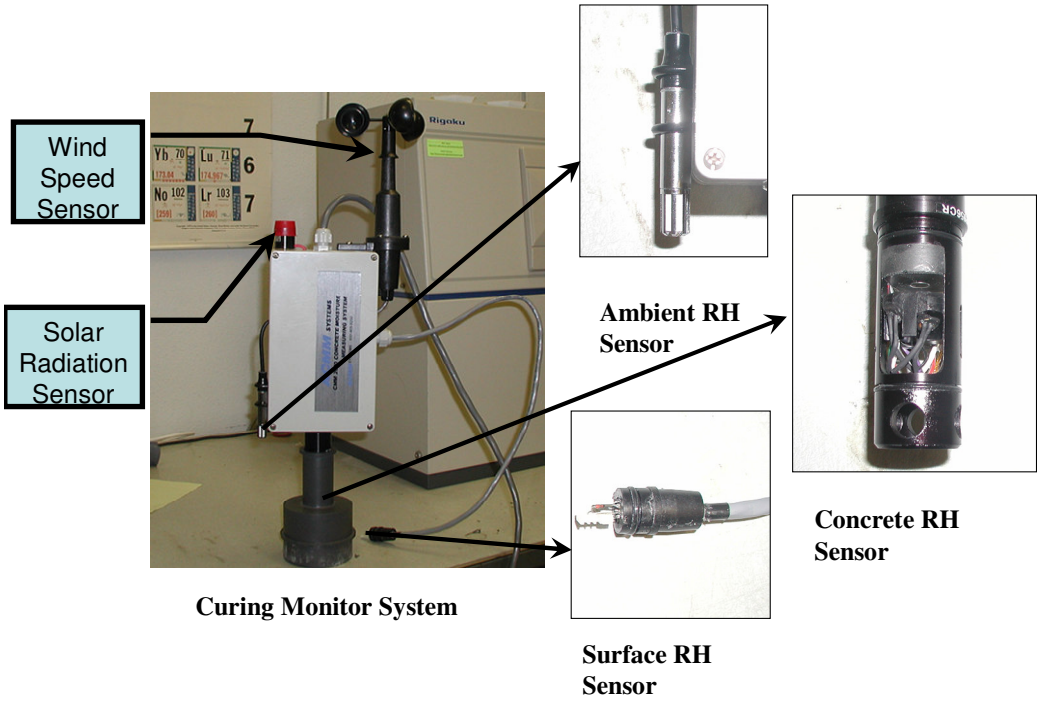

Fig. III-4. CMS Sensors

Relative humidity measurements at the concrete surface and 1 inch below require sampling chambers that have water vapor pressure equilibrating with the pore pressure of the concrete. Sampling chambers are shown in Fig. III-5 and Fig. III-6. The chamber for chilled mirror sensor is inserted 1 inch into the concrete. The chamber for concrete

surface humidity rests on the surface of the fresh concrete and it consists of a filter paper (Fig. III-5 (a)) on which a layer of curing compound is sprayed. The relative humidity in the surface humidity chamber represents the humidity of concrete surface immediately below the curing membrane.

(a)Filter Paper Cover (b) Surface Chamber

Fig. III-5. Surface Chamber Setup

Fig. III-6. Chilled Mirror Chamber

Sample Data Presentation

An example of the data collected during an evaporation test of a given compound is shown in the figures below. Relative humidity data and weight loss data are presented in

Fig. III-7 and Fig. III-8. As previously noted, the ambient RH and the wind speed are fixed at 30% and 10 mph. The surface relative humidity experienced an increase, which corresponds to bleeding action, and then gradually decreases. The rate of water loss from the surface of the specimen was initially high then decreased with time.

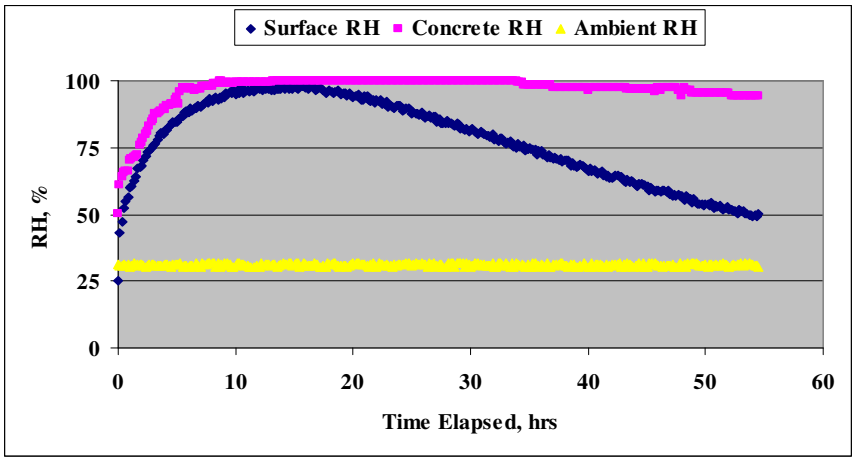

Fig. III-7. Relative Humidity Data

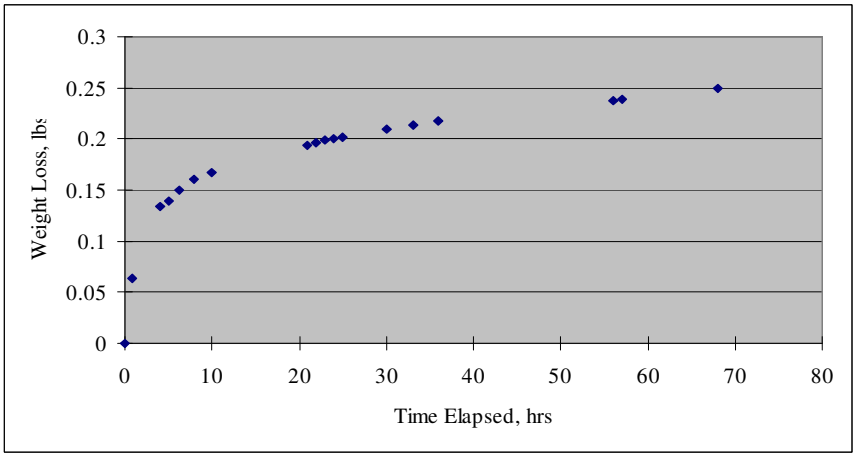

Fig. III-8. Weight Loss Data

Theoretical Basis

Gibbs' free energies per unit mass of water in the concrete and in the environment, which are determined by concrete relative humidity and ambient relative humidity respectively, governs the rate of moisture exchange between the concrete and the ambient air. It can be described by equation (III-1).

$$\vec{n} \cdot \vec{J} = -B\left(\ln(RH_a) - \ln(RH_s)\right) \tag{III-1}$$

where

B = surface emissivity which is property of curing membrane,

$\vec{n}$ = unit outward normal at the concrete surface,

RH_a = ambient relative humidity,

RH_s = surface relative humidity, and

$\vec{J}$ = water evaporation rate.

From the lab data, we can calculate B by rewriting equation (III-1) to equation (III-2).

$$B = -\frac{\vec{n} \cdot \vec{J}}{\left(\ln(RH_a) - \ln(RH_s)\right)} \tag{III-2}$$

Since $\vec{J}$ could be expressed in equation (2-28), equation (III-1) can be written as equation (III-3).

$$c \cdot grad\left(RH\right)\vec{n} = B\left(\ln(RHa) - \ln(RHs)\right) \tag{III-3}$$

Under isothermal and pressure conditions, the effective curing thickness (ECT) is defined by rewriting equation (III-3), which is shown in equation (III-4) (Bažant and Najjar 1972).

$$ECT = {}^{c}\!/_{B} \cdot = \frac{\left(\ln(RHa) - \ln(RHs)\right)}{grad\left(RH\right)\vec{n}} \qquad \text{(III-4)}$$

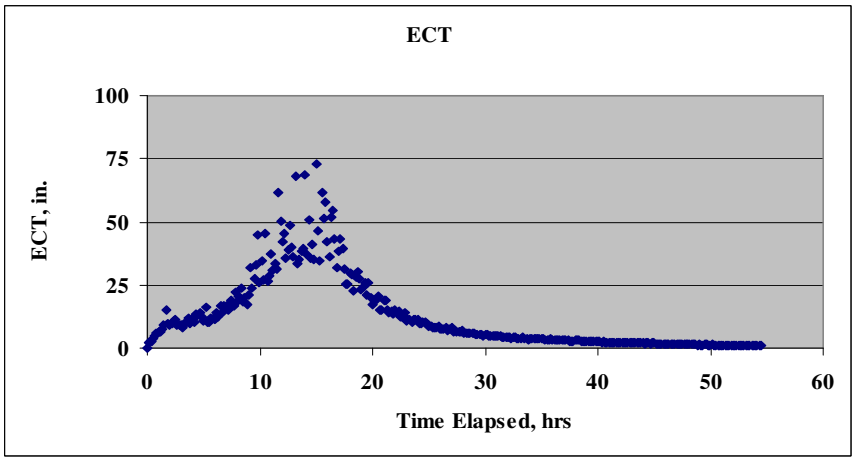

Fig. III-9. ECT vs. Time

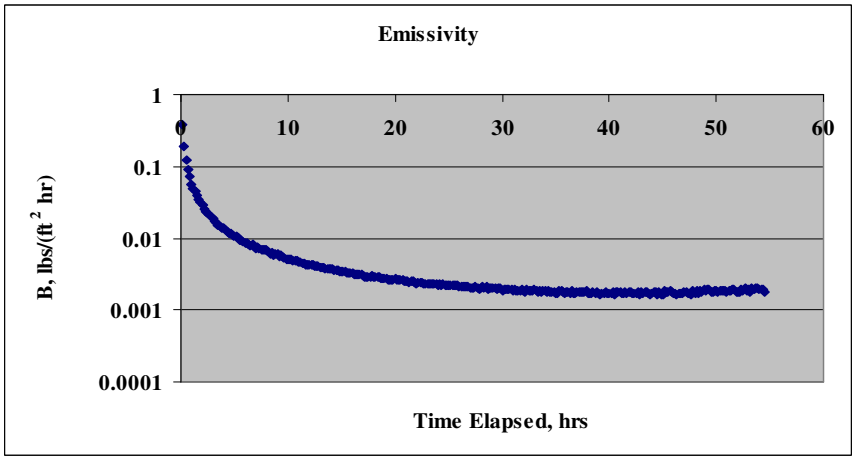

Fig. III-10. Emissivity vs. Time

ECT and Emissivity are presented in Fig. III-9 and Fig. III-10, respectively. Under lab condition, ECT is a direct measure of curing compound effectiveness. After bleeding, ECT decreased gradually, which is the sign of the deterioration of curing

compound. Equation (III-2) is used to calculate emissivity and equation (III-4) is used to calculate ECT.

The Weibull accumulative distribution is widely used in reliability and life data analysis due to its versatility. Depending on the values of the parameters, the Weibull distribution can be used to model a variety of life behaviors. ECT falls into the category of life behaviors. Equation (III-5) shows the general utility function form that we modified from the Weibull function.

$$W(t,\alpha,\beta,\tau) = \tau \cdot \left[1 - e^{-\left(t/\beta\right)^{\alpha}}\right] \qquad \text{(III-5)}$$

where,

τ = amplifying parameter

β = scaling parameter, and

α = shift parameter.

Equation (III-5) is the Weibull accumulative distribution function, which is used to approximate ECT with time. The resulting parameters are listed in Table III-2. The comparison between actual ECT curve from the measured lab data and approximation curve is shown in Fig. III-11. For this curing compound, the EI is 0.945 at the age of 24 hours.

Table III-2. Regressed Parameters

α	0.348
β	1.019
τ	739049

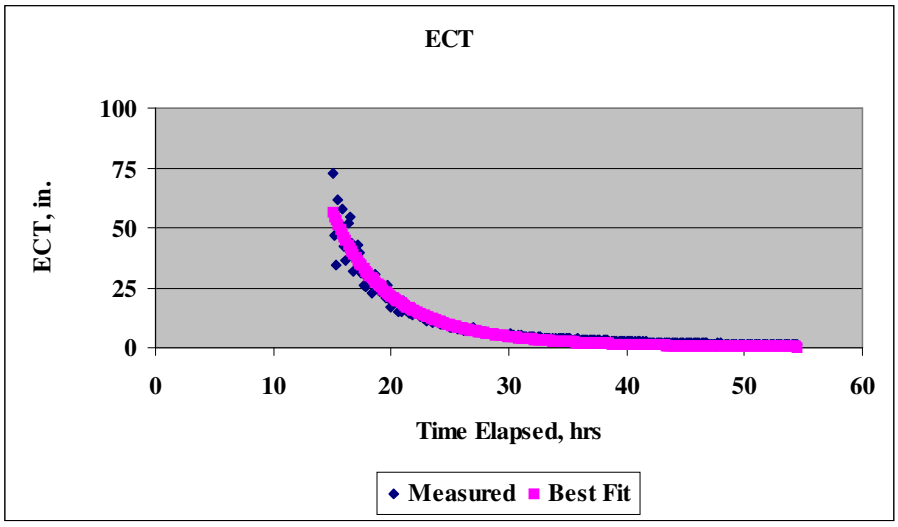

Fig. III-11. Measured ECT vs. Modeled ECT

The following will discuss about how the parameters τ, α, and β affect the shape of the curve, as shown in Fig. III-12, Fig. III-13, and Fig. III-14. ECT vs. time data are regressed based on equation (III-5) and as time increases, the value of w decreases. As the curing compound ages, the curve goes through an inflection point and decreases sharply. The Weibull function relates well to the degradation of the curing compound as it ages (governed by the α parameter), the rate of application (governed by the τ parameter), and the duration of the curing (governed by the β parameter).

Evaluation Index

The life time behavior for the curing compound is regressed into three parameters, i.e. α, β, and τ. Each one of them has a meaning to depict the curing compound performance, thus it is more comprehensive to establish an index with a combination of α, β, and τ. By far, the proposed evaluation index is presented in (III-6).

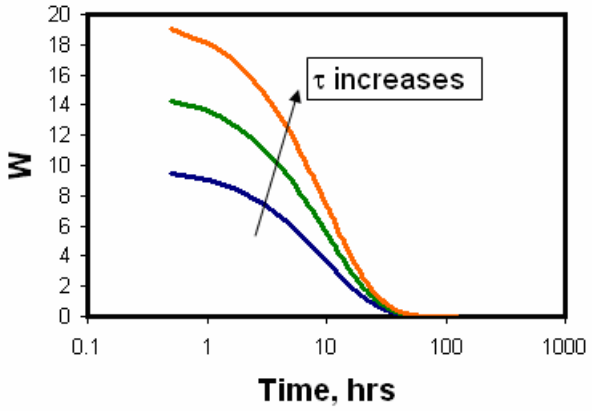

Fig. III-12. τ's Effect on the Curve

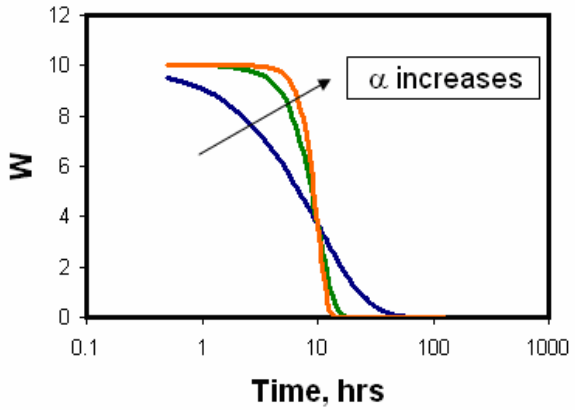

Fig. III-13. α's Effect on the Curve

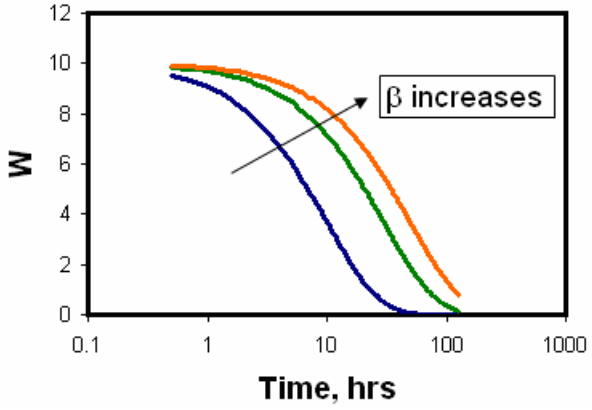

Fig. III-14. β's Effect on the Curve

$$EI = \frac{ECT}{\tau} = \left[1 - e^{-\left(t/\beta\right)^{\alpha}}\right] \quad \text{(III-6)}$$

where, EI = evaluation index.

EI ranges between 1 and 0 when a perfectly performing curing compound would reflect an ET=1. Since α, β, and τ are regressed from the data for a duration of 72 hours, EI is more instructive as a evaluation index than total water loss rate, which is the index of ASTM C 156.

CURING COMPOUND RANKING

TxDOT uses only Type 2 curing compound. However, in this test program, five different curing compounds, three of which were resin-based and the other two were wax-based, were tested. The classifications of the tested curing compound samples are listed in Table III-3. Type 2 denotes white pigmented curing compounds. Class B denotes the solids in the compounds are resin-based and there is no restriction for Class A.

Table III-3. Classification of Curing Compounds

Manufacture/designation	Type	Comments
WR Meadow 2255	Type 2—Class B	High Reflective
WR Meadow 2250	Type 2—Class B	High Reflective
WR Meadow 1640	Type 2—Class A	Wax-based
WR Meadow 1600	Type 2—Class A	Wax-based
WR Meadow 1250	Type 2—Class B	Normal Resin-based
ECO	Type 2—Class A	
Concrete Chemical	Type 2—Class A	

The ranking of these tested curing compounds are shown in Table III-4. High reflective curing compound and wax based curing compounds showed the best EIs over

other curing compounds. Concrete Chemical and ECO curing compounds showed similar performance. And 1250 had the worst EI.

Table III-4. Ranking of Curing Compounds

Type	α	β	τ	EI	Ranking
WR Meadow 2255	0.48911	1.4074	748.462	0.98176	1
WR Meadow 2250	0.47563	1.42356	823.233	0.97835	2
WR Meadow 1640	0.46131	1.41747	328.217	0.97498	3
WR Meadow 1600	0.4423	1.6023	408.213	0.96351	4
Concrete Chemical	1.1236	18.632	632.123	0.73527	5
ECO	1.13012	21.321	375.83	0.68118	6
WR Meadow 1250	1.96394	24.9162	19.0712	0.60508	7

FIELD APPLICATION

Similar to the ASTM C 156, which specifies the moisture loss limit relative to the strength of concrete as would be determined by compressive cylinders (ASTM C 39 1999), a series of physical properties were planned to be conducted to give a basis for applying the curing membrane ranking to conditions in the field. Thin specimens were used instead of cylinder specimens. The objective is to establish the basis for curing effectiveness on the physical properties for field application. These tests were conducted through a full factorial of combinations of two factors, potential of evaporation (PE), which is calculated by equation (III-7), and application rate.

$$PE = [T_c^{2.5} - (R * T_a^{2.5})] [1 + 0.4 V] * 10^{-6} \quad \text{(III-7)}$$

where

PE = Potential of Evaporation rate, $lb/ft^2/hr$

T_c = Concrete Temperature, ^oF

T_a = Air Temperature, ^oF

R = (Relative Humidity %) / 100, and

V = Wind Velocity, mph.

Physical Properties Tests

The physical properties of interest are mortar strength and porosity as would be determined by the mercury intrusion porosimetry (MIP) test. The dimension for mortar strength is a 2 by 2 in. cube, while for the MIP test specimen shown in Fig. III-15 can be used.

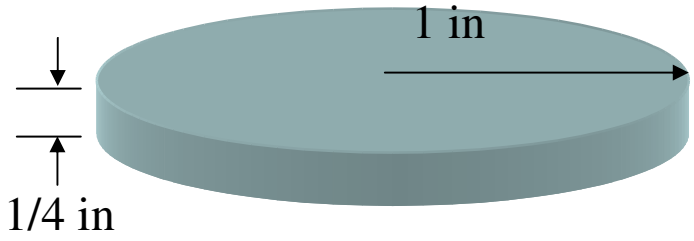

Fig. III-15. Diagram for MIP Test Specimen

Curing Effectiveness Index

The total porosity was measured for the specimens under a full factorial of environmental conditions (variant PE) and curing conditions (curing compounds application rate). The total porosity of sealed specimen and exposed specimen was also measured. Thus the curing effectiveness index can be calculated based on a relative scale, which is presented in equation (III-8).

$$CE = \frac{S_C - S_E}{S_S - S_E} \tag{III-8}$$

where

S_C = total porosity of cured sample,

S_E = total porosity of exposed sample, and

S_S = total porosity of sealed sample.

Test Design and Results

MIP specimens were designed to be cured under different potential of evaporation (PE) conditions and curing conditions (application rate). To encompass the extreme of ambient condition that might occur in the field, different potential of evaporations (PE) should be applied in the lab. As stated earlier, temperature, relative humidity, and wind are the three main factors that affect PE. To achieve different PEs, three different wind conditions were. Under some field conditions, PE could be less than 0.066 lb/ft^2/hr, but the range of the test parameters shown in Table III-5 encompasses a broad range of field conditions. Fig. III-16 shows how the specimens were cured under the conditions shown in Table III-5 and different rates of application.

Table III-5. Wind Speed and PE

Wind Speed, mph	**PE, lbs/ft^2/hr**
0	0.066
10	0.331
20	0.596

(a) high wind speed.

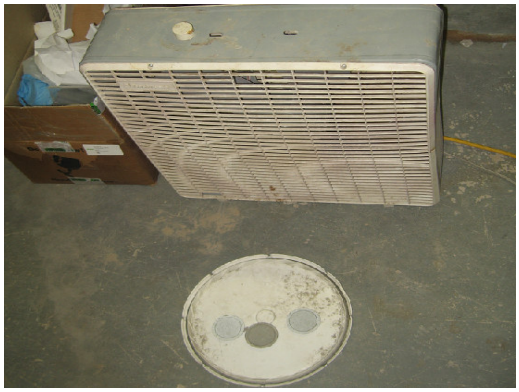

(b) medium wind speed.

(c) no wind.

(d) sealed specimen

Fig. III-16. Samples Cured under Different PEs

TxDOT requires two time curing membrane applications with an application rate of 180 ft^2/gallon each time. The variable application rates are listed in Table III-6.

Table III-6. Levels of Application Rate

	Low	**Medium**	**High**
Application Rate, ft^2/gallon	180	90	60

Fig. III-17 shows the total porosity for samples under different conditions. As expected, intruded mercury volume is high under high wind speed and low application rate conditions.

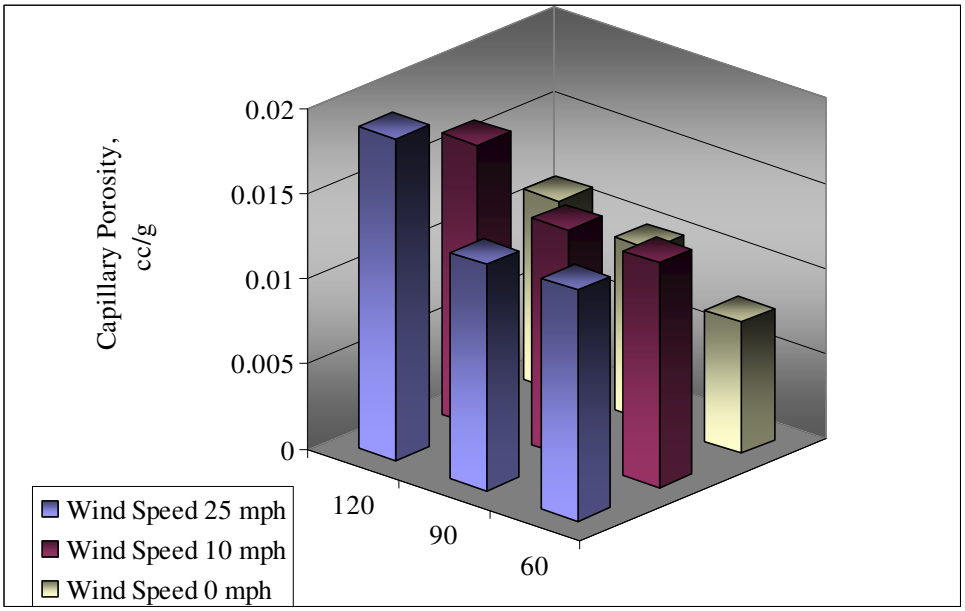

Fig. III-17. Capillary Porosity (cc/gram)

The curing effectiveness index can be defined in terms of the application rate (AR) and potential of evaporation (PE) in the form of equation (III-9). The increase of either of AR or PE would cause CE to decrease. The regressed parameters are listed in Table III-7.

$$\ln(CE) = -\left(\frac{AR}{a}\right)^{b} - \left(\frac{PE}{c}\right)^{d} \qquad \text{(III-9)}$$

where

a, b, c, d = regressed parameters,

AR = application rate, and

PE = potential of evaporation.

Table III-7. Regressed Parameters

a	**b**	**c**	**d**
179.744	4.223	0.968	1.192

A nomograph is created from equation (III-9) as shown in Fig. III-18. This nomograph comprises of two charts. The values on each chart are curing effectiveness (CE) and potential evaporation (PE) respectively. To use this nomograph, one starts from the evaluation index (EI), then draws a vertical line till meeting the designed CE, then draws a horizontal line towards the chart on the right till hitting the curve with the PE value of actually ambient conditions, and then draw a vertical line towards the axis of application rate.

Field Application Example

The following example describes how to determine AR to satisfy required CE.

The ambient weather conditions are as follows: temperature = 104 ºF (40 ºC), relative humidity = 30%, and wind speed = 10 mph. Suppose 1250 and 2255 types of curing compound will be used, and the designed CE is 0.70.

The EIs for 1250 and 2255 are 0.61 and 0.98 respectively. From equation (III-7), the PE is 0.395 lbs/ft^2/hr. As shown in Fig. III-18, the application rates should be 57 ft^2/gal. and 144 ft^2/gal., respectively, for curing compounds 1250 and 2255 to achieve 0.70 CE under the ambient conditions which correspond to a PE of 0.395 lbs/ft^2/hr.

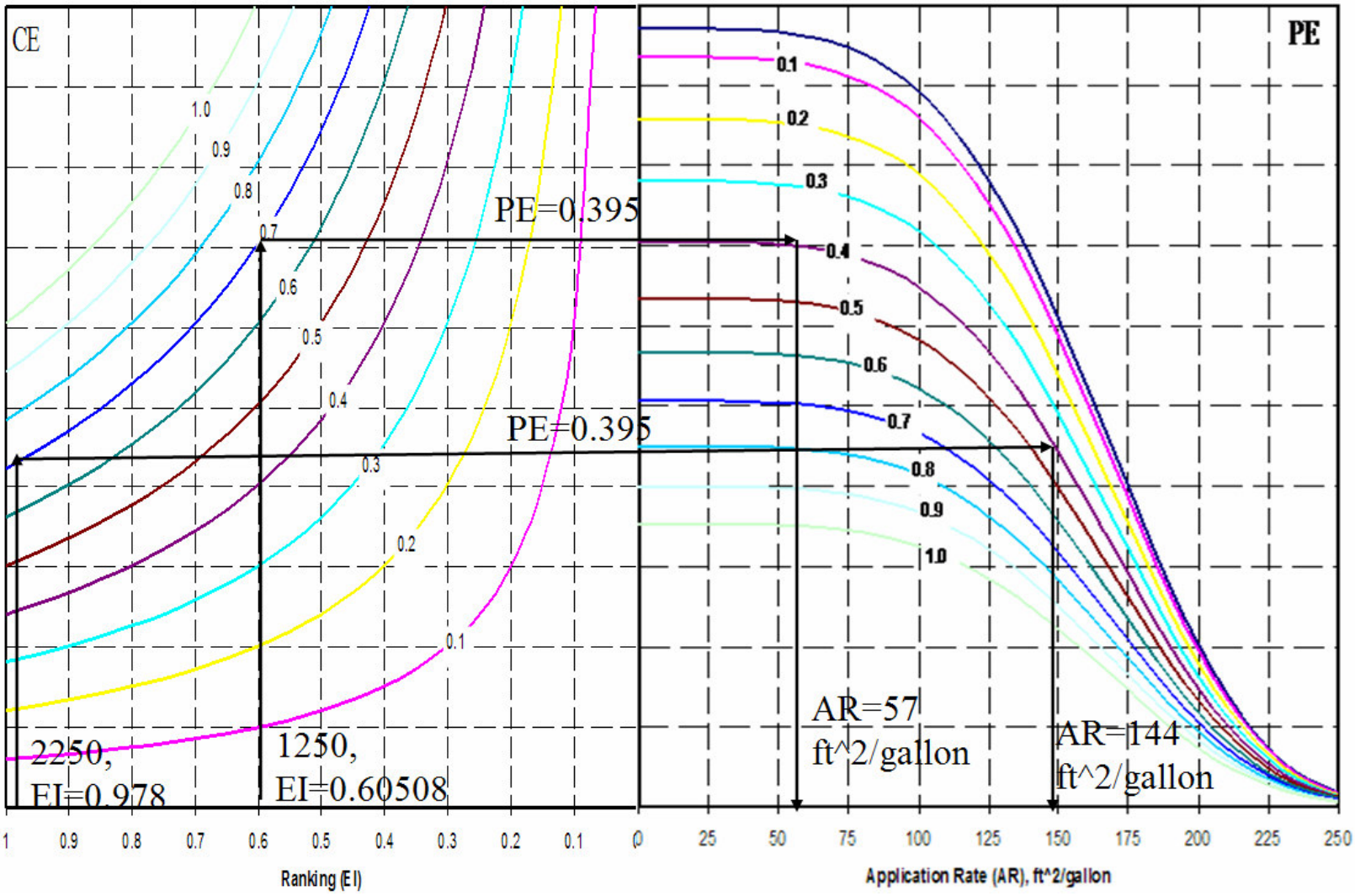

Fig. III-18. Nomograph for AR Determination

COMPARISON OF ASTM C 156 AND THE NEW PROTOCOL

As stated before, ASTM C 156 is less efficient to serve as a curing effectiveness evaluation method. The new protocol is designed dedicatedly to overcome those deficiencies that ASTM C 156 possesses, and it is more sensitive to capture the subtle difference created by curing and direct curing practice according to the field weather conditions and the curing compound. The comparisons about two methods are listed in Table III-8.

Table III-8. Comparison of ASTM C 156 & the New Protocol

	Instrumentation/ Equipment	**Effectiveness Basis of Curing**	**Dependant Parameters**	**Standard Conditions**	**Physical Properties**
ASTM C 156	Weighing Scale	Moisture Loss	None	Temperature, and Relative Humidity	Strength of Thick Cylinders
New Protocol	CMS and Weighing Scale	RH Measurements at 3 Locations	PE, AR	Temperature, Relative Humidity, and Wind	Porosity of Thin Samples

SUMMARY

This chapter presents a new laboratory protocol which has a field application. A series of curing compounds were tested and ranked through this protocol. In conjunction with physical property test, the new protocol has the potential to guide field curing practice even under various ambient weather conditions.

CHAPTER IV
FIELD TESTING ON CURING EFFECTIVENESS EVALUATION

A good curing practice in the field consists of three components: lab approved curing compound, good field application, and appropriate ambient conditions, as shown in Fig. IV-1.

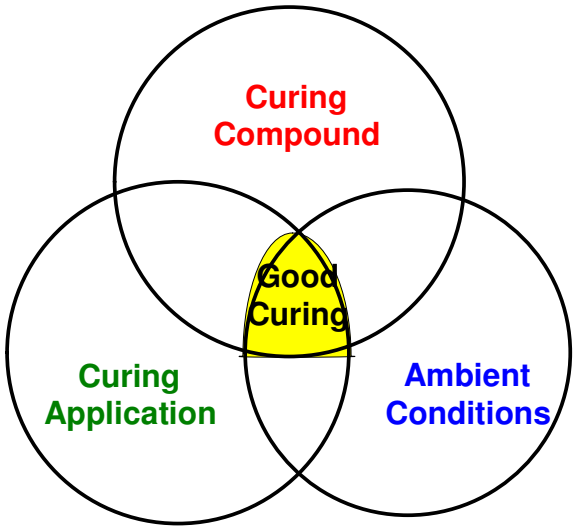

Fig. IV-1. Diagram of Good Curing Practice

A high ranked curing compound doesn't guarantee a good curing practice in the field, provided the curing compound is not properly applied. Under severe ambient conditions, an appropriate higher curing compound application rate should be applied to achieve designed curing effectiveness.

A series of field tests have been carried under the TxDOT Project 5106. Type of curing compound, application scheme, application method and ambient condition, are under investigation for their effects on curing effectiveness from both a curing membrane moisture retention standpoint and a concrete physical property standpoint. Field test data will be presented in this chapter. Synthesis of the field tests and findings will be discussed thereafter in this chapter.

CMS SETUP PROCEDURES IN THE FIELD

The use of CMS requires placing two sampling chambers, one for surface relative humidity and the other for concrete relative humidity at 1 inch below the concrete surface. In order to properly install the CMS and not to intervene the surface finishing and curing compound application activities, certain procedures need to be followed, as shown in Fig. IV-2.

(a) Dummy Casing and Filter Paper Cover

(b) Removing Dummy Casing

(c) After Removing Dummy Casing

(d) Filter Paper Cover

(e) Surface Humidity Sample Chamber

(f) Setup of CMS

Fig. IV-2. Procedures for CMS Setup in Field

Procedures:

1. Place dummy casing and filter paper cover when tining is finished, seeing Fig. IV-2 (a);
2. Remove dummy casing and take off paper filter after curing compound application(Fig. IV-2 (b) and (c));
3. Place chilled mirror sensor casing;
4. Insert chilled mirror sensor into casing and screw the filter paper cover onto surface relative humidity chamber(Fig. IV-2 (d) and (e)).

FIELD TEST AT THE FRONT ROAD OF LOOP 610

Field tests were carried out on a Loop 610 frontage road construction site near Stella Link Rd, in the Houston District during the month of September 2005 to investigate the performance of ECO cure and AHT cure under field conditions.

Two 150 feet sections were placed with the first section cured by AHT cure and the second section cured by ECO cure. Three coats were applied for both AHT cure section and ECO cure section. The first coat was applied immediately after the bleeding was over and the second coat was applied right after the first coat with the time delayed less than 30 minutes. The third coat for AHT cured section was applied 5 hours later after the second coat and that for the ECO cured section was applied 12 hours after the second coat. All the applications were conducted manually.

Two CMSs were set up to monitor the relative humidity at three different locations, i.e. ambient relative humidity, surface relative humidity, and concrete relative humidity at 1 inch below the concrete surface, to help characterize the behaviors of the curing membrane. Temperature information at three locations could be acquired as well. In addition, two more functions were added to CMS to monitor solar radiation intensity and wind speed, which have large influence on the behaviors of the curing membrane.

Ambient Conditions

The ambient weather conditions were characterized by ACI 308. The potential of evaporation (PE) is shown in Fig. IV-3. PE normally reaches its peak values during

noon hours when air temperature is high, air relative humidity is low, solar radiation is high, and probably wind speed is high. In this field test, the highest PE was about 0.20 lb/ft^2/hr.

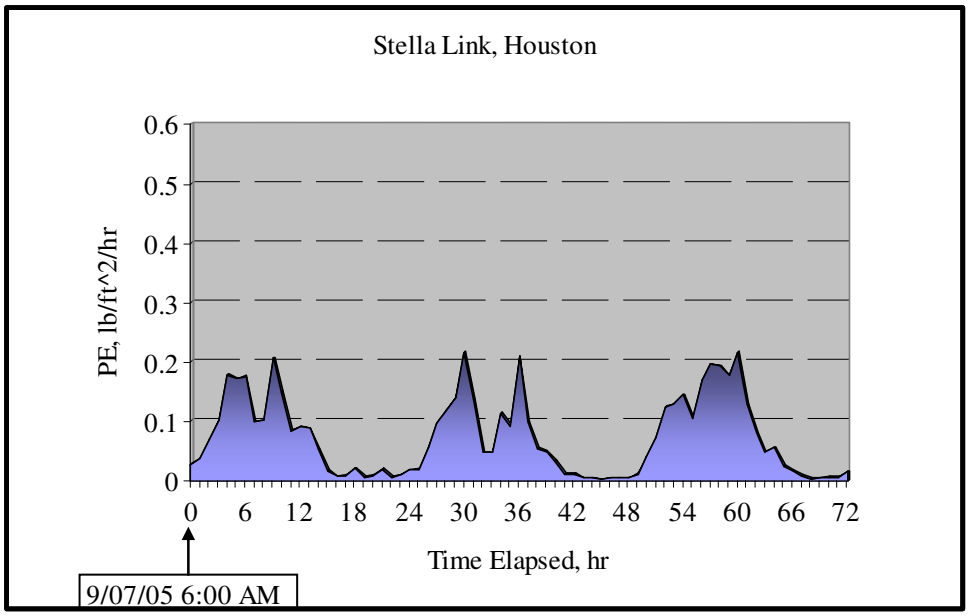

Fig. IV-3. Potential of Evaporation @ Loop 610

Data Presentation

Relative humidity data for AHT cured section are presented in Fig. IV-4. From Fig. IV-4, it is observed that the surface relative humidity stayed at a high level during night hours and it began to fluctuate when day time came in the second day. When the curing membrane experienced the first day time, surface relative humidity just fluctuated without dropping too much. During the third day time, it, however, dropped dramatically.

Relative humidity data for ECO cured section are presented in Fig. IV-5. The surface relative humidity followed the same pattern as that of the AHT cured section. Thus, it is evident the effectiveness for these two curing compounds were about the same in this field test.

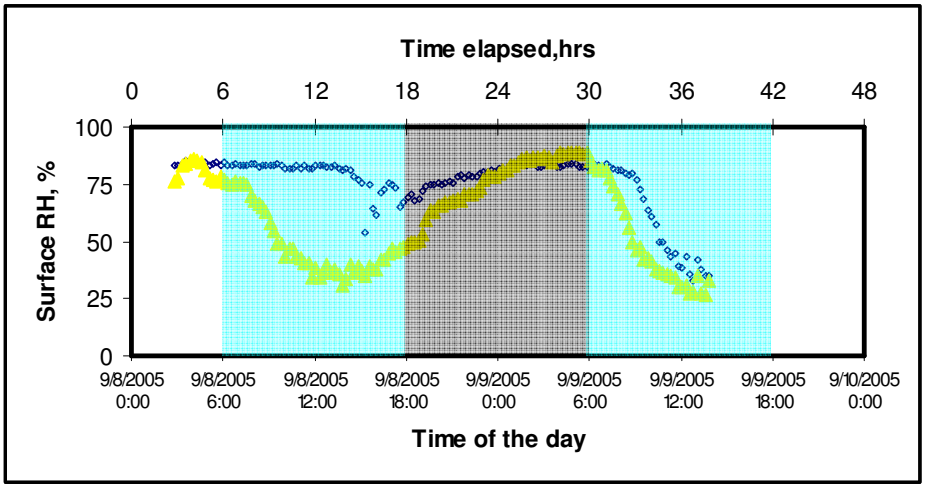

Fig. IV-4. Relative Humidities for the Section Cured with AHT

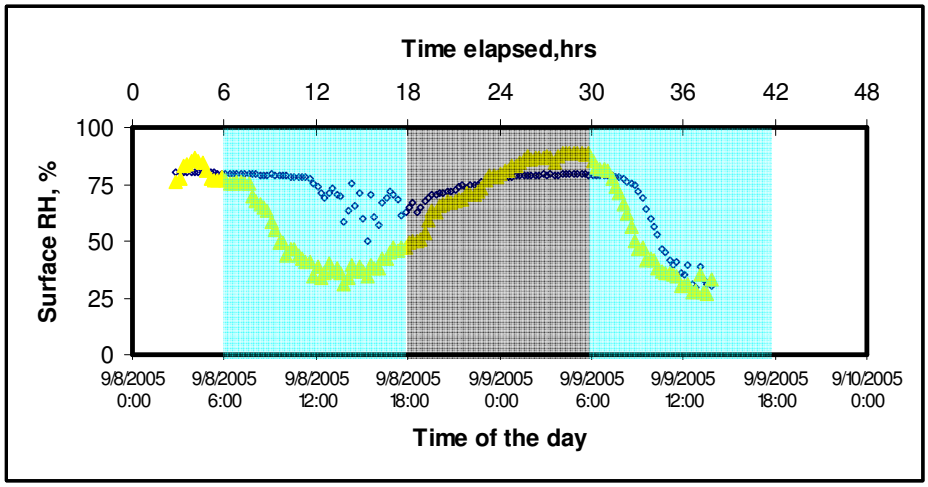

Fig. IV-5. Relative Humidities for the Section Cured with ECO

FIELD TEST AT SH 130 ROUND ROCK

Field test was carried out on SH130 construction site near FM 685, in the Round Rock during the month of September 2005 to compare the performance of high reflective curing compound (Sealtight® 2255) and normal resin based curing compound (Sealtight® 1200) under field conditions.

Two sections were placed with the first section cured with Sealtight® 1200 cure and the second section cured with Sealtight® 2255 cure. Two coats were applied for both sections according to TxDOT specifications. The third coat was applied manually when the drop of the surface humidity was observed.

Ambient Conditions

The ambient weather conditions were characterized by ACI 308. The potential of evaporation (PE) is shown in Fig. IV-6. In this field test, the highest PE was about 0.33 lb/ft^2/hr. It was about 0.1 lb/ft^2/hr higher than that of the ambient conditions at Loop 610.

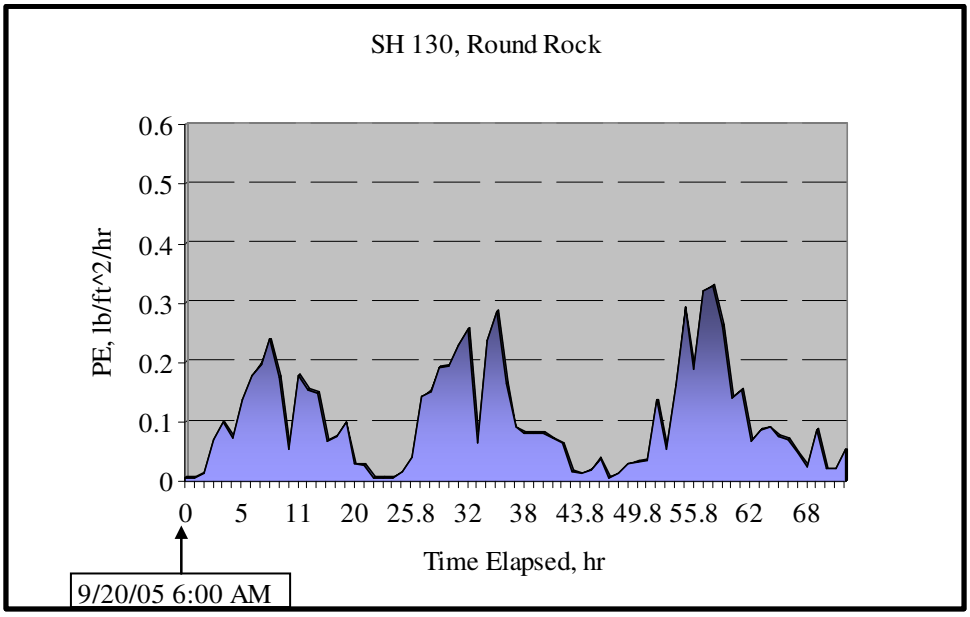

Fig. IV-6. Potential of Evaporation @ SH 130

Data Presentation

Relative humidity data for normal curing compound cured section are presented in Fig. IV-7. It is observed that the surface relative humidity was beginning to break in the second day. But it began to recover when night time came. It began to break again when day time came in the third day.

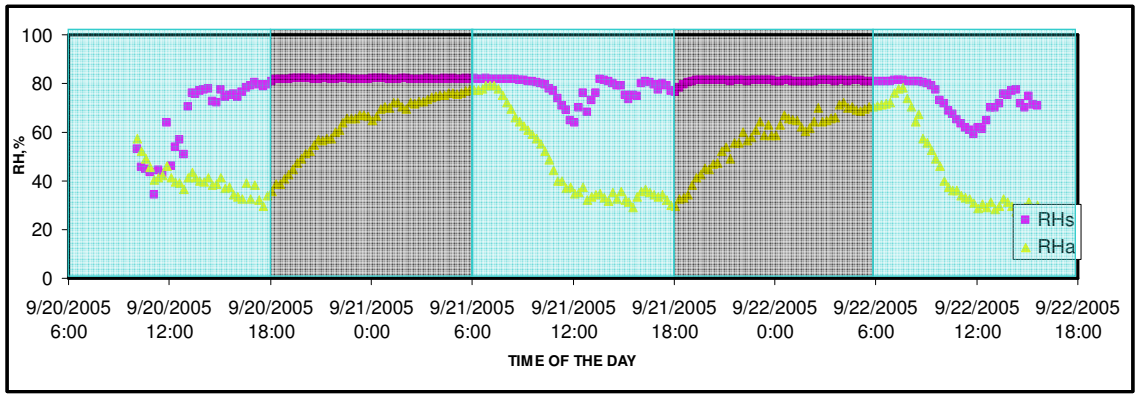

Fig. IV-7. Relative Humidities for High Reflective Curing Compound

Relative humidity data for high reflective curing compound cured section are presented in Fig. IV-8. It was expected to have better performance. But it is observed that the surface relative humidity was beginning to break in the second day. After a third coat was applied, there was an increase in the surface relative humidity. However, it just maintained a couple of hours then it broke again.

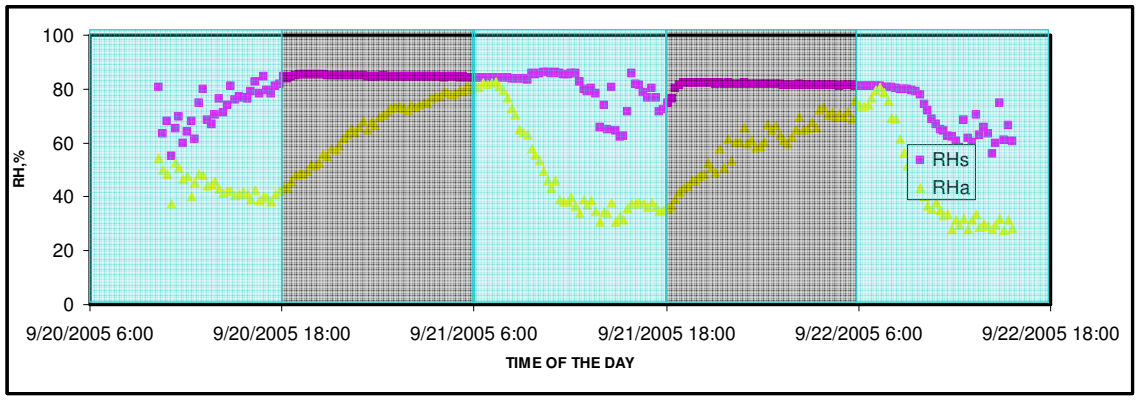

Fig. IV-8. Relative Humidities for High Reflective Curing Compound

For this field test and the field tests thereafter, dielectric constant (DC) measurements were conducted to assess the curing effectiveness. Percometer was used to collect DC values, as shown in Fig. IV-9.

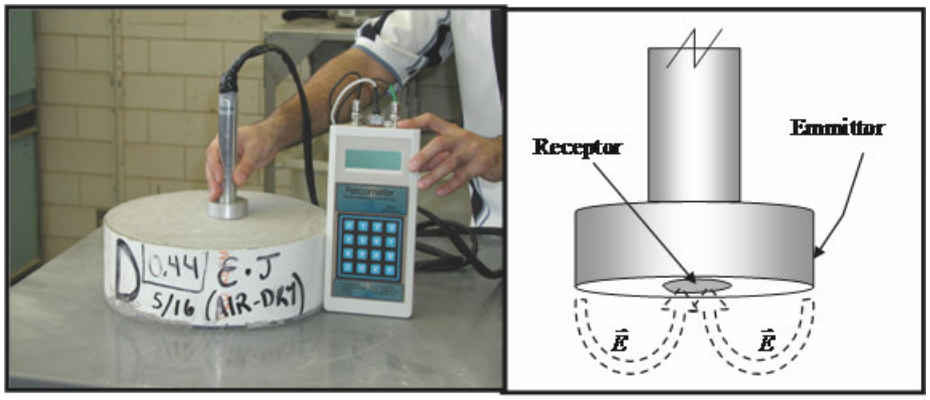

Fig. IV-9. Percometer

The relative dielectric constant of a material under given conditions is a measure of the extent to which it concentrates electrostatic lines of flux. It is the ratio of the amount of stored electrical energy when a potential is applied, relative to the permittivity of a vacuum. It is also called relative permittivity. The dielectric constant is represented as ε_r. It is defined as

$$\varepsilon_r = \frac{\varepsilon_s}{\varepsilon_0} \tag{IV-1}$$

where ε_s is the static permittivity of the material, and ε_0 is vacuum permittivity. Vacuum permittivity is derived from Maxwell's equations by relating the electric field intensity E to the electric flux density D. In vacuum, the permittivity ε is just ε_0, so the dielectric constant is 1.

DC exhibits a decaying trend as concrete hardens. The decease is corresponding to the decrease of water content in the concrete. There are two main factors causing this decrease. One is the self-desiccation since hydration process and the other the water loss into the air.

DC slope is the decaying rate of DC value in the first a couple days. It is help to evaluate the curing effectiveness under the same ambient conditions. If DC slopes are

intended to evaluate the curing effectiveness under different ambient conditions, normalization is needed to offset the effect of ambient conditions.

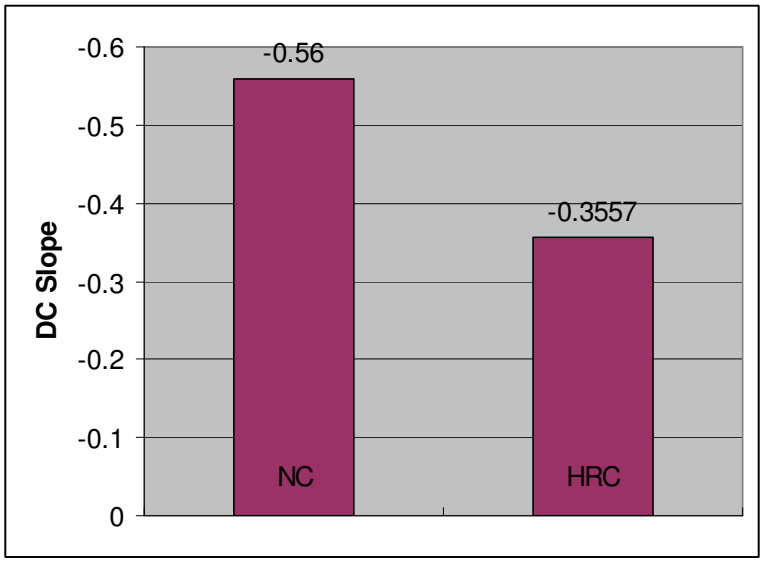

Fig. IV-10. DC Slopes for SH 130 Field Test

Based on DC slope, high relative curing compound (HRC) had better performance than normal curing compound (NC).

FIELD TEST AT SH 288 PEARLAND

Field test was carried out on SH 288 construction site, in the Pearland during the month of November 2005 to compare the performance of high reflective curing compound (Sealtight® 2255) and normal resin based curing compound (Sealtight® 1200) under field conditions.

There were four test sections for curing effectiveness evaluation (Table IV-1). High reflective curing compound (HRC) was applied only in section 2 and it was applied manually. All other sections were using machine to spray the curing compound.

Table IV-1. Curing Facts in SH 288

	Curing Compound	**Spray Method**
Section 1	NC	Machine Spray
Section 2	HRC	Manual Spray
Section 3	NC	Machine Spray
Section 4	NC	Machine Spray

Ambient Conditions

The ambient weather conditions were characterized by ACI 308. The potential of evaporation (PE) is shown in Fig. IV-11. Since it was conducted in November, the highest PE was about 0.15 lb/ft^2/hr, which was relatively mild.

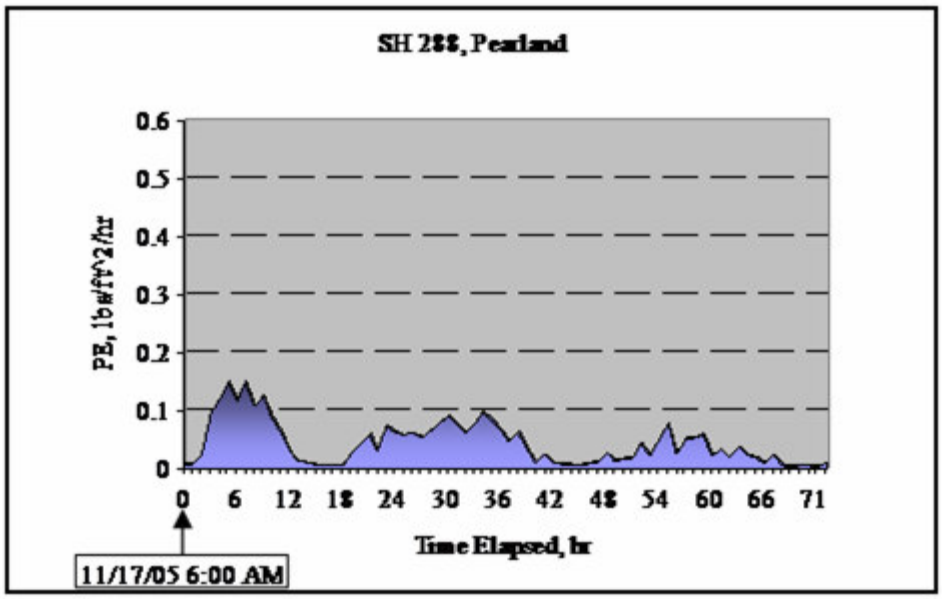

Fig. IV-11. Potential of Evaporation @ SH 288

Data Presentation

Relative humidity data are presented in Fig. IV-12, Fig. IV-13, Fig. IV-14, and Fig. IV-15, respectively. WS/RH is the ratio between the wind speed and the air relative humidity. It is also an indicator of ambient weather condition.

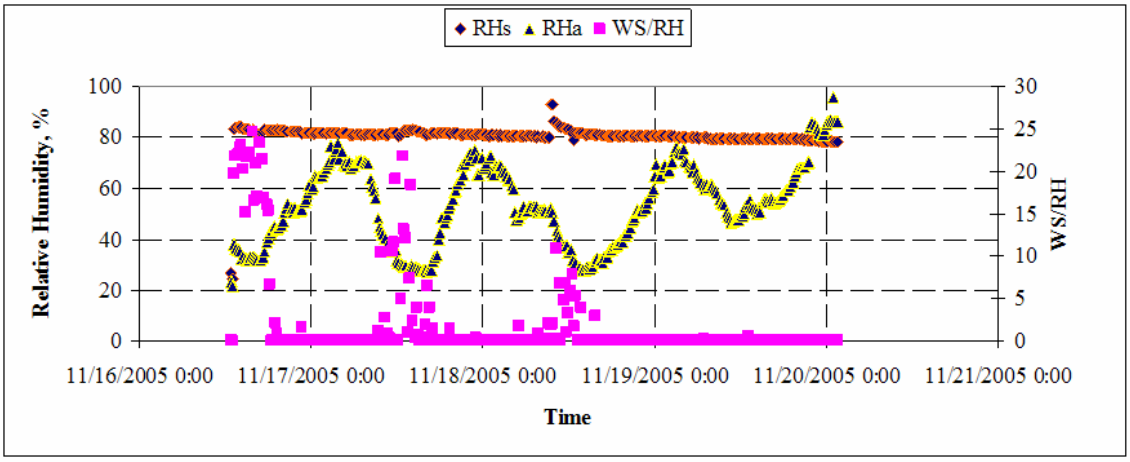

Fig. IV-12. Relative Humidities for Section 1(SH 288)

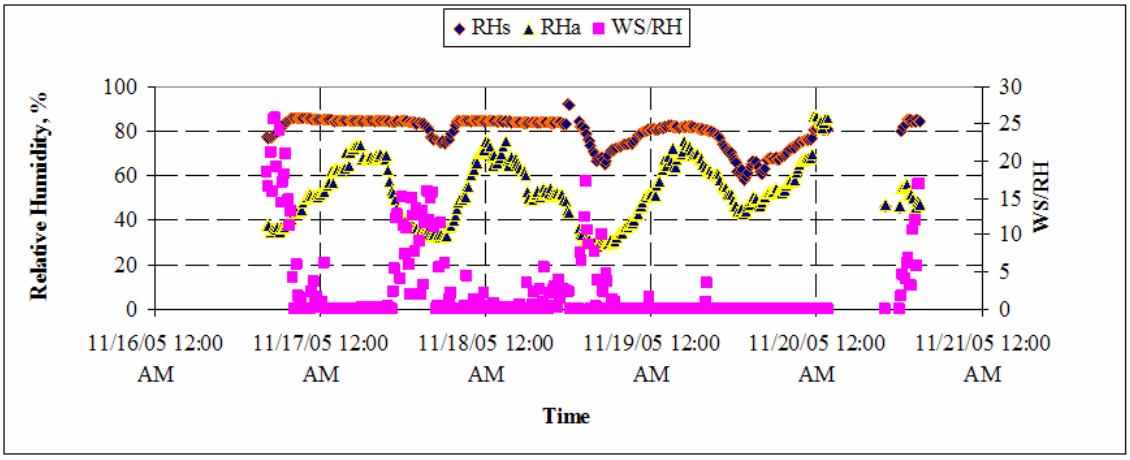

Fig. IV-13. Relative Humidities for Section 2(SH 288)

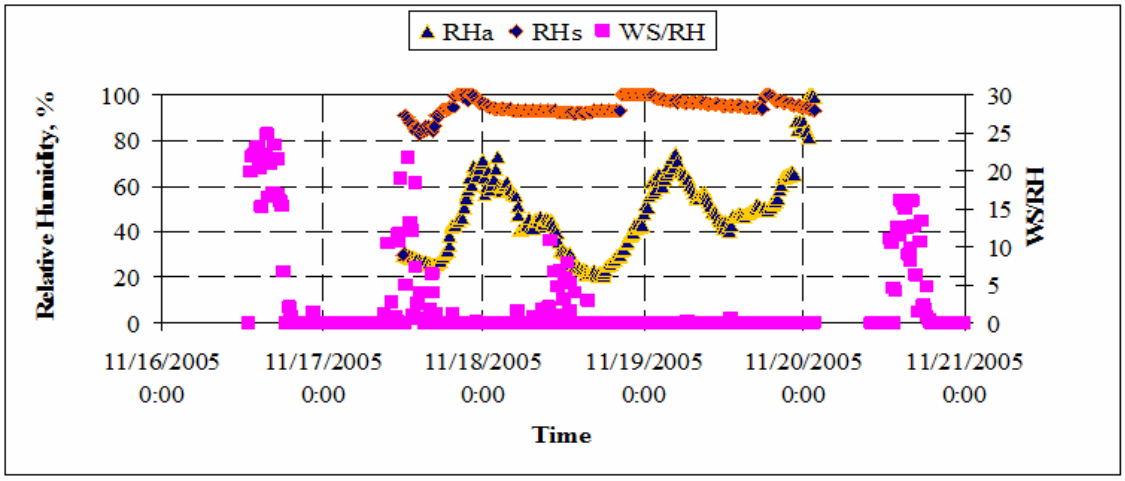

Fig. IV-14. Relative Humidities for Section 3(SH 288)

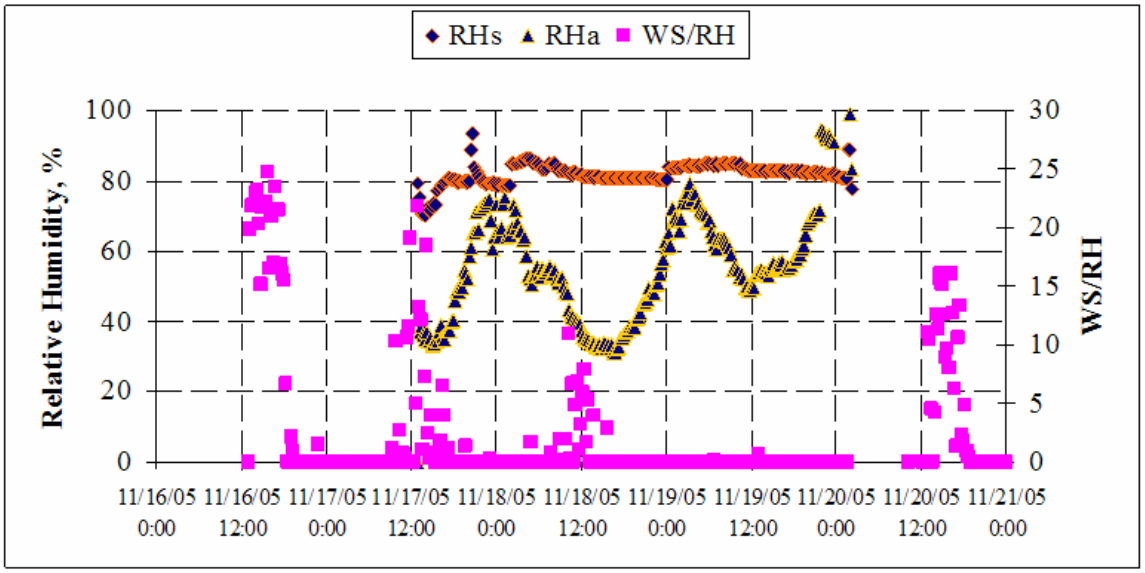

Fig. IV-15. Relative Humidities for Section 4(SH 288)

Surface relative humidity data for normal curing compound cured sections were all above 80%, which is an indicator of good curing. On the contrary, relative humidity data for high reflective curing compound cured section (Fig. IV-13) was beginning to break in the second day and the drop was getting more and more severe in the second day and in the third day. Under laboratory rankings, high reflective curing compounds

rank higher than normal resin-based curing compound. However the manual spray for high reflective curing compound might account for the bad performance in the field. The problem with manual spray is that it cannot ensure uniformity of the curing membrane. It might get excessive curing compound on some spots but less curing compound on the other spots.

The DC data is shown in Fig. IV-16. The DC slopes for normal curing compound cured sections range from -0.2 to -0.3, while the slope for high reflective curing compound cured section is the lowest. This might due to the fact the spot, where the DC measurements were taken, had excessive curing compound sprayed due to the manual spray.

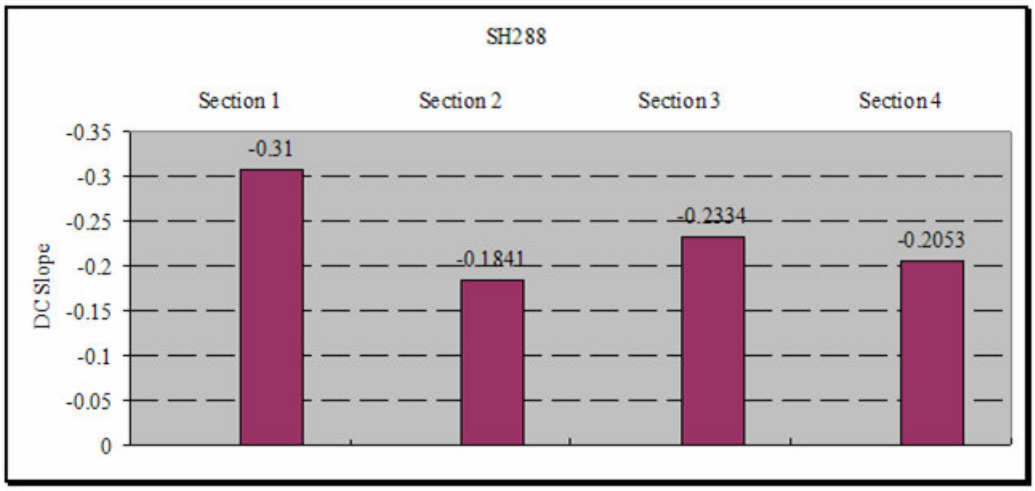

Fig. IV-16. DC Slopes for SH 288 Field Test

FIELD TEST AT SH 35 (APRIL)

Field test was carried out on SH 35 construction site, in the West Columbia during the month of April 2006 to compare the performance of high reflective curing compound (Sealtight® 2255) and normal resin based curing compound (Sealtight® 1200) under field conditions.

There were four test sections for curing effectiveness evaluation (Table IV-2). Manual spray was used for all sections.

Table IV-2. Curing Facts in SH 35 (April)

	Curing Compound	**Spray Method**
Section 1	NC	Manual Spray
Section 2	HRC	Manual Spray
Section 3	NC	Manual Spray
Section 4	NC	Manual Spray

Ambient Conditions

The ambient weather conditions were characterized by ACI 308. The potential of evaporation (PE) is shown in Fig. IV-17. The highest PE was about 0.20 lb/ft^2/hr. During the first two days the PE was mild and it became stronger in the third day.

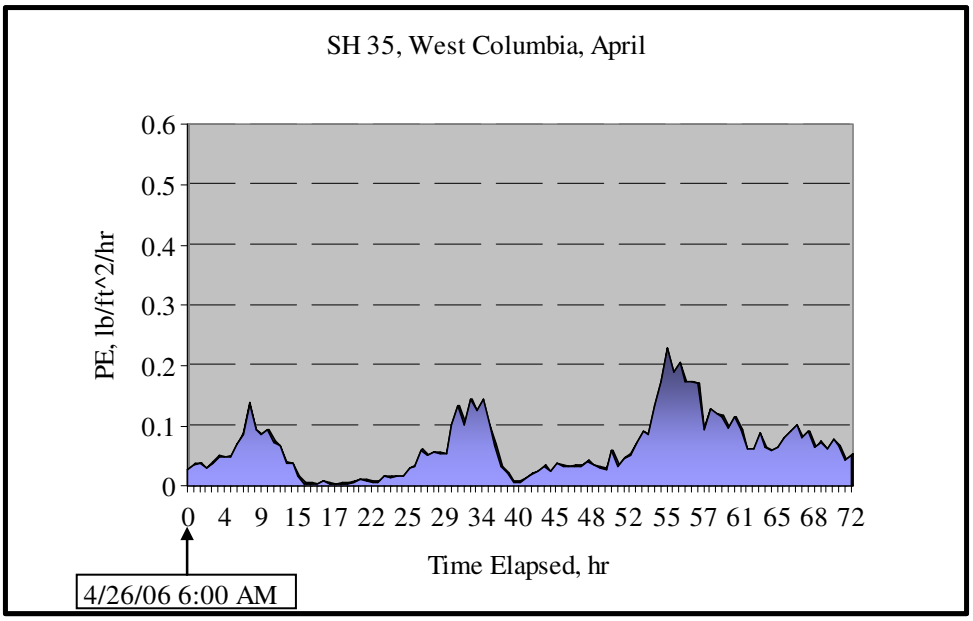

Fig. IV-17. Potential of Evaporation @ SH 35 (April)

Data Presentation

Relative humidity data are presented in Fig. IV-18, Fig. IV-19, Fig. IV-20, and Fig. IV-21, respectively.

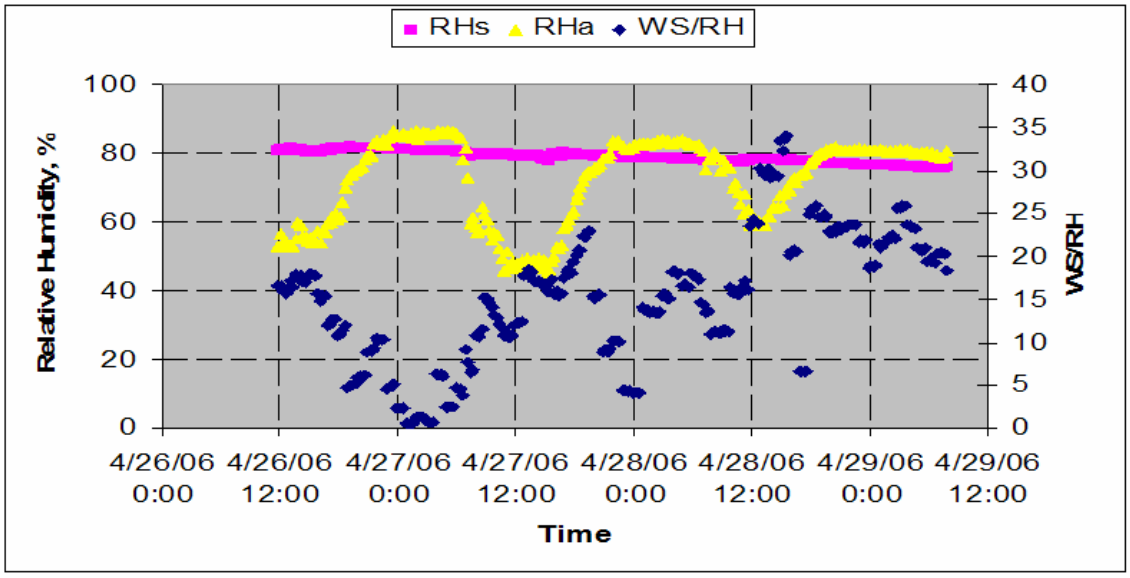

Fig. IV-18. Relative Humidities for Section 1 (SH 35, April)

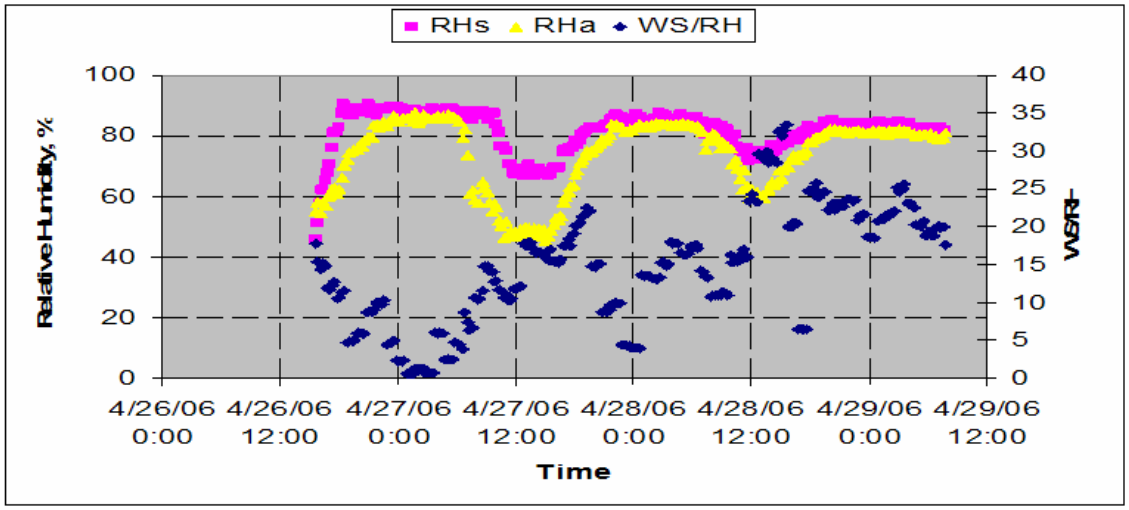

Fig. IV-19. Relative Humidities for Section 2 (SH 35, April)

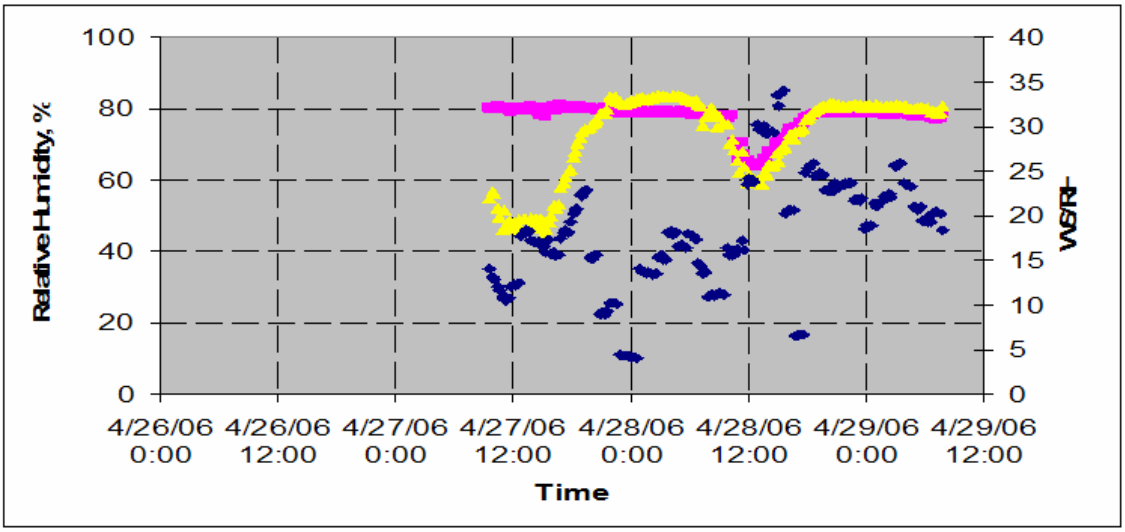

Fig. IV-20. Relative Humidities for Section 3 (SH 35, April)

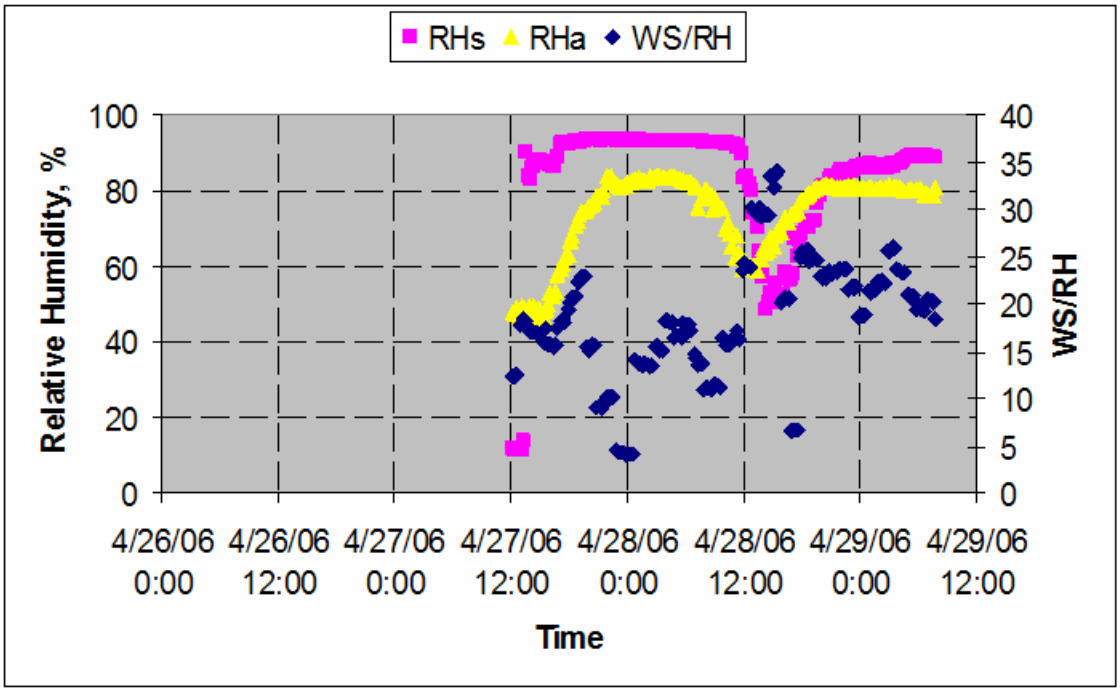

Fig. IV-21. Relative Humidities for Section 4 (SH 35, April)

Based on surface relative humidity, it is observed that only section 1 had good curing. In all other sections, the surface relative humidities just broke in the second day after concrete placement.

DC measurements are available only in section 1 and section 2. The DC slopes are shown in Fig. IV-22. These slopes match well with moisture data. DC slope in the section 1 was much smaller than that in the section 2.

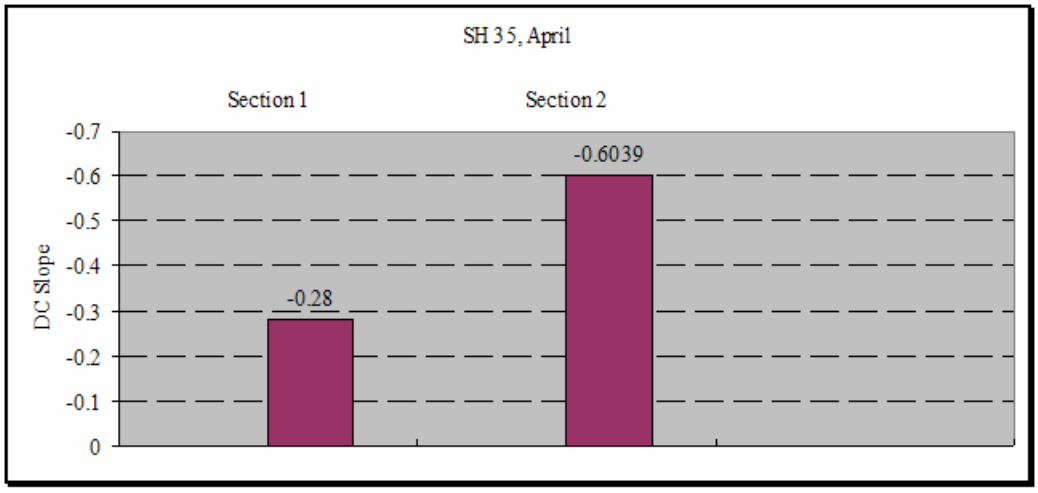

Fig. IV-22. DC Slopes for SH 35 Field Test (April)

FIELD TEST AT SH 35 (MAY)

Field test was carried out on SH 35 construction site, in the West Columbia during the month of May 2006 to the effects of delayed application and reapplication in the second day on curing effectiveness.

The application scheme is shown in Table IV-3. The application schemes for the section 1 and section 2 were the same, except that section1 was placed in the morning and section 3 was placed in the afternoon. Normal curing compound and manual spray were used in this field test.

Table IV-3. Application Scheme SH 35 (May)

	First Coat	**Second Coat**	**Third Coat**
Section 1	1 hr after concrete placement	Second day 10 am	
Section 2	1 hr after concrete placement	5 hrs after concrete placement	Second day 10 am
Section 3	1 hr after concrete placement	Second day 10 am	

Ambient Conditions

The ambient weather conditions were characterized by ACI 308. The potential of evaporation (PE) is shown in Fig. IV-23. The highest PE was about 0.35 lb/ft^2/hr.

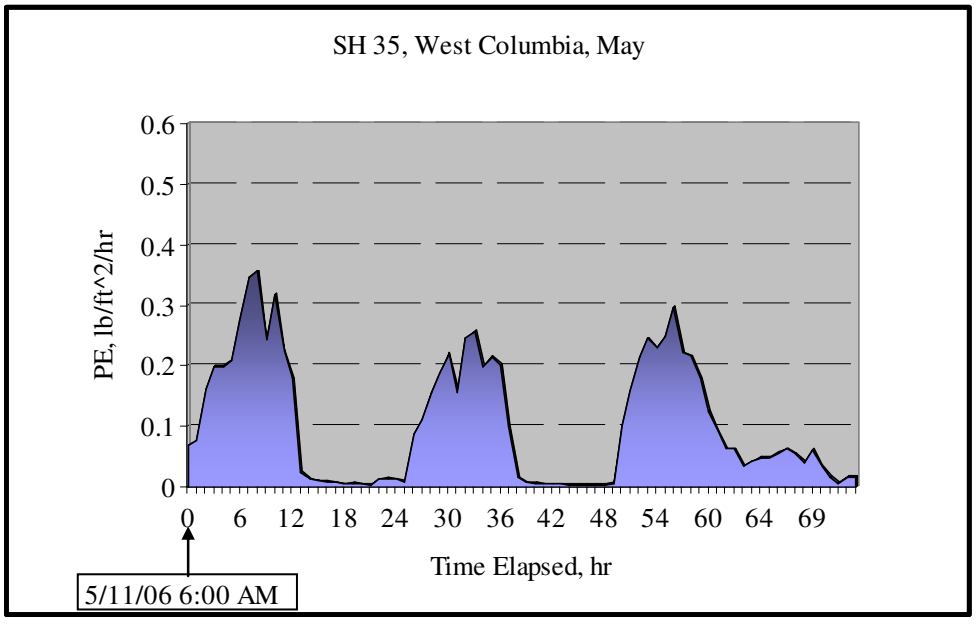

Fig. IV-23. Potential of Evaporation @ SH 35 (May)

Data Presentation

Relative humidity data are presented in Fig. IV-24, Fig. IV-25, and Fig. IV-26, respectively. The pink curves are surface relative humidity and the yellow curves are ambient relative humidity.

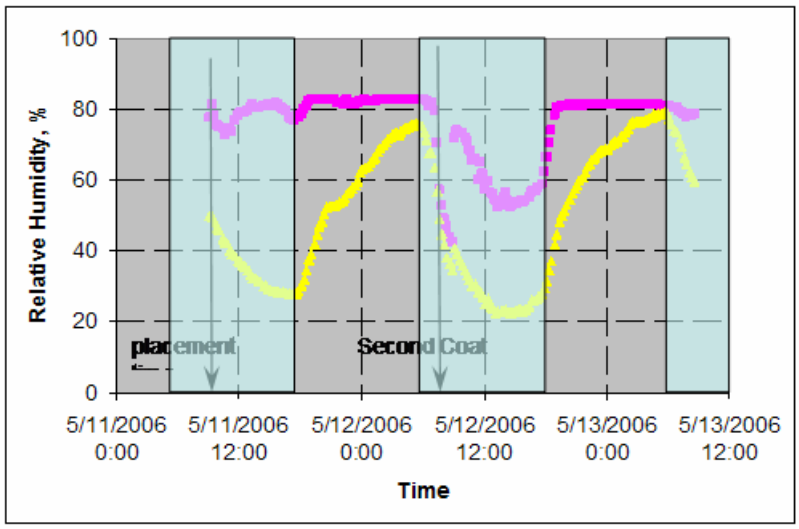

Fig. IV-24. Relative Humidities for Section 1 (SH 35, May)

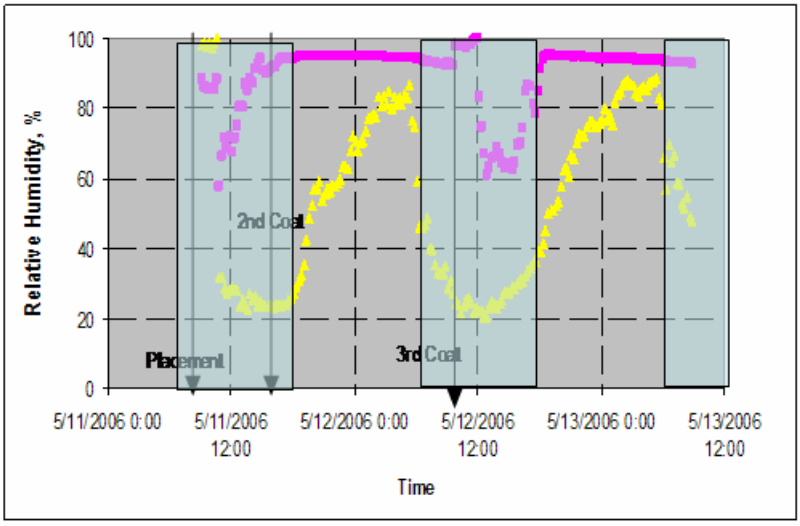

Fig. IV-25. Relative Humidities for Section 2 (SH 35, May)

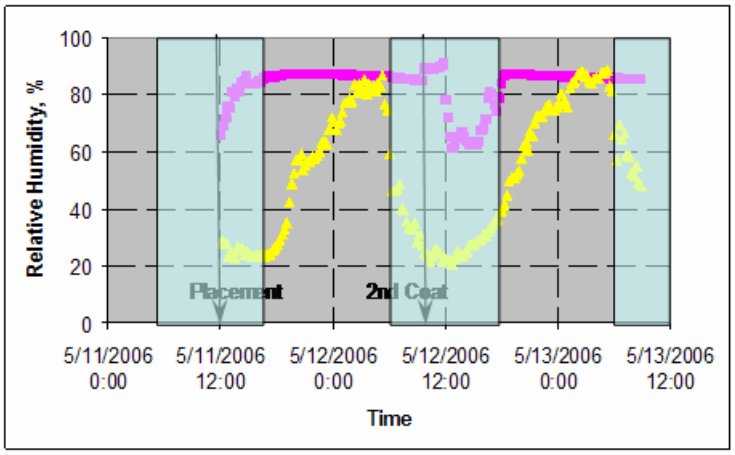

Fig. IV-26. Relative Humidities for Section 3 (SH 35, May)

From the surface humidity data, it is found that neither of the sections provided good curing on the second day, which was due to the bad application of manual spray, second day application couldn't improve the curing quality, and the application scheme in the section 2 showed the best curing quality among three sections. DC slopes are shown in Fig. IV-27. Again, due to non-uniformity of manual spray cause the data less representative.

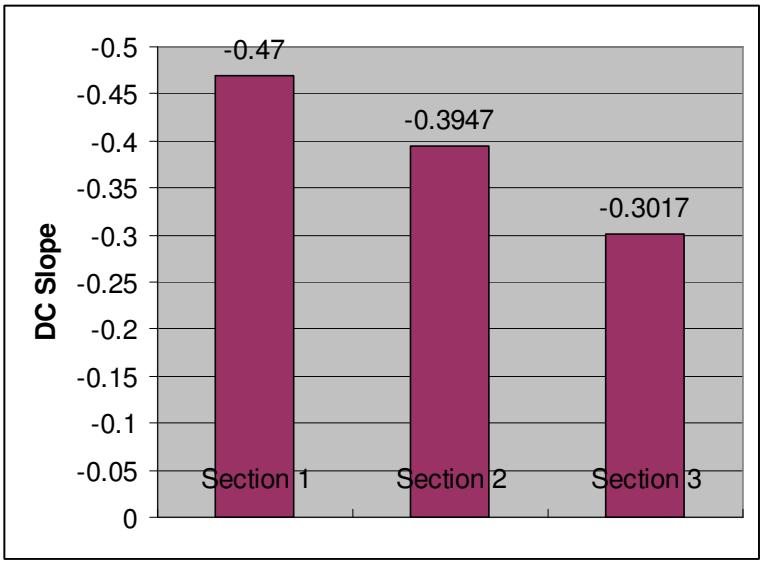

Fig. IV-27. DC Slopes for SH 35 Field Test (May)

FIELD TEST AT SH 35(JUNE)

Field test was carried out on SH 35 construction site, in the West Columbia during the month of June 2006 to the effects of retardant and reapplication of high reflective curing compound in the second day on curing effectiveness.

Three sections were investigated. The application scheme is shown in Fig. IV-28. The application schemes for the section 1 and section 2 were the same, except that section1 was placed in the morning and section 3 was placed in the afternoon. Manual spray was used in this field test. Retardant was applied immediately after surface finishing.

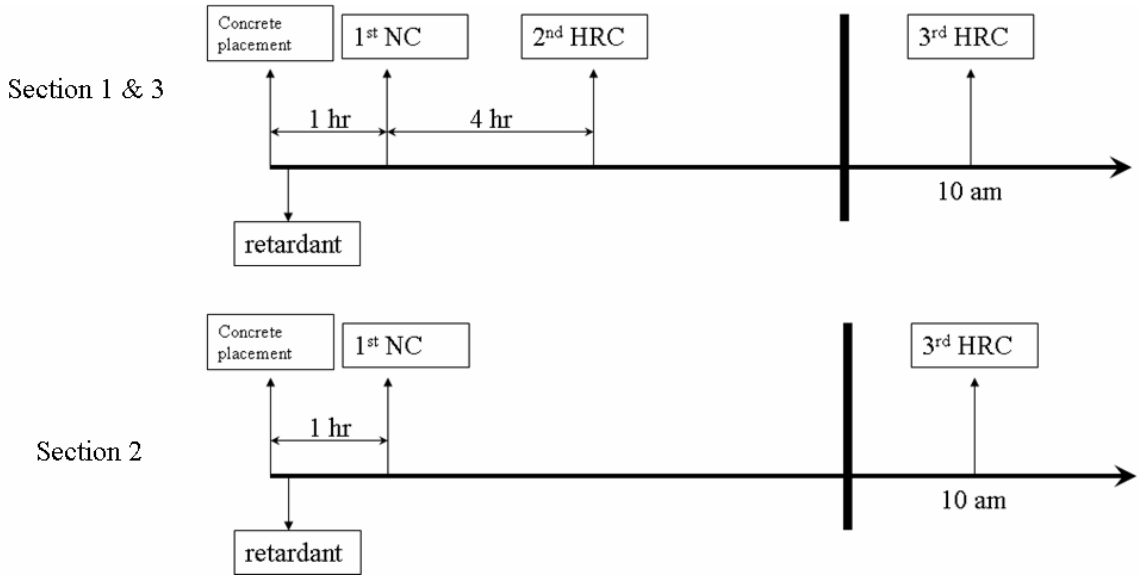

Fig. IV-28. Application Scheme SH 35 (June)

Ambient Conditions

The ambient weather conditions were characterized by ACI 308. The potential of evaporation (PE) is shown in Fig. IV-29. The highest PE was about 0.20 lb/ft^2/hr.

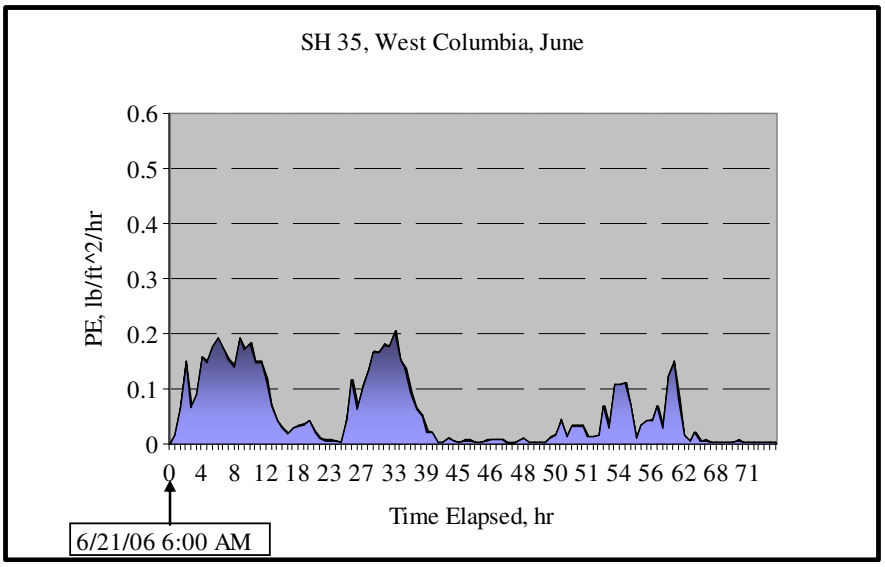

Fig. IV-29. Potential of Evaporation @ SH 130

Data Presentation

Relative humidity data are presented in Fig. IV-30, Fig. IV-31, and Fig. IV-32, respectively. The pink curves are surface relative humidity and the yellow curves are ambient relative humidity.

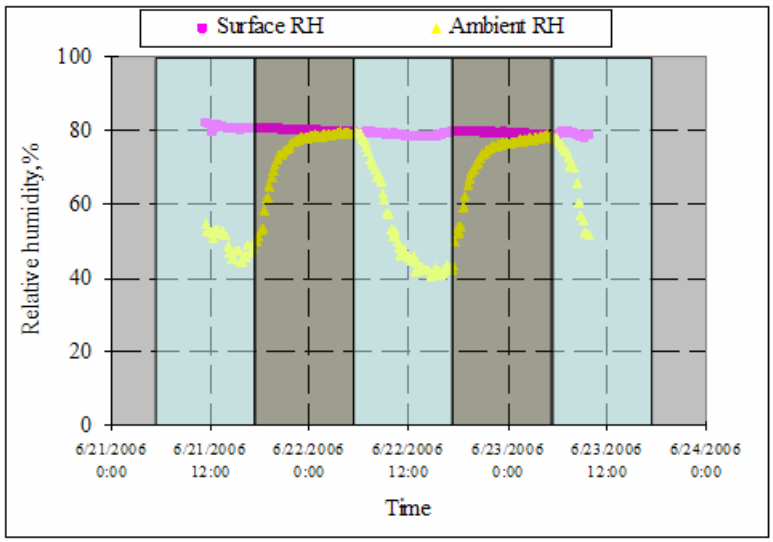

Fig. IV-30. Relative Humidities for Section 1 (SH 35, June)

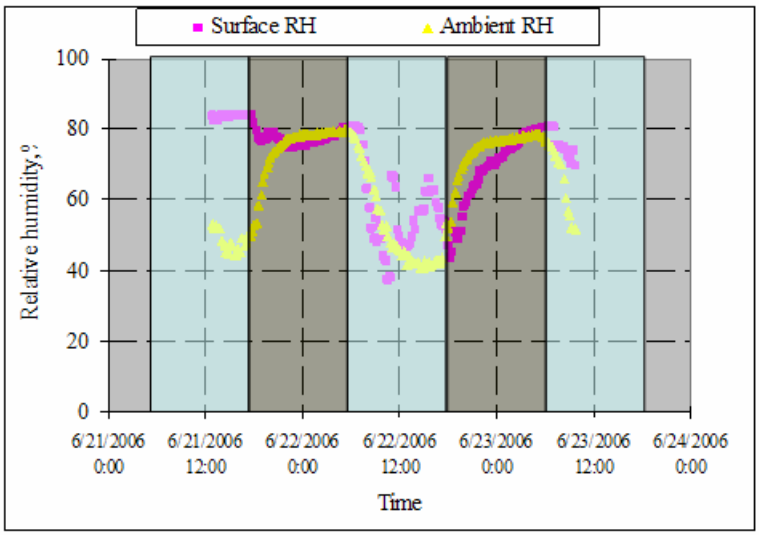

Fig. IV-31. Relative Humidities for Section 2 (SH 35, June)

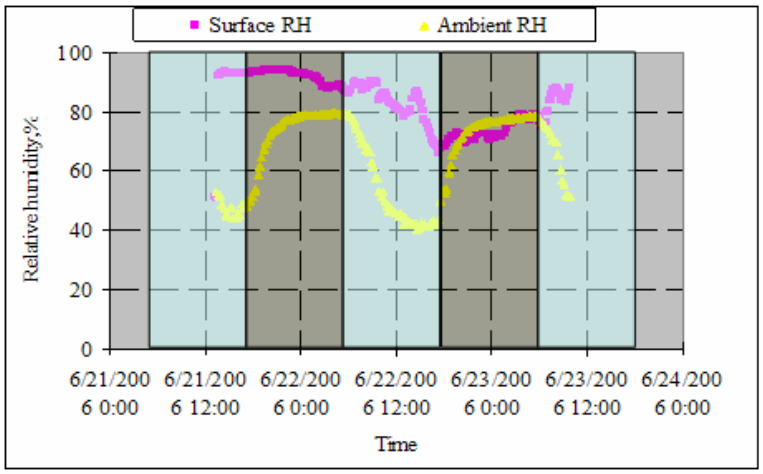

Fig. IV-32. Relative Humidities for Section 3 (SH 35, June)

Section 1 and Section 3 showed good curing quality, which means double manual spray increase the uniformity of curing membrane. One single manual sprayed normal curing compound coat cannot ensure curing quality in the second day. Second day curing compound application could not improve curing quality, even if high reflective curing compound is applied.

DC slopes are shown in Fig. IV-33. From DC slopes, there was not too much difference between each section.

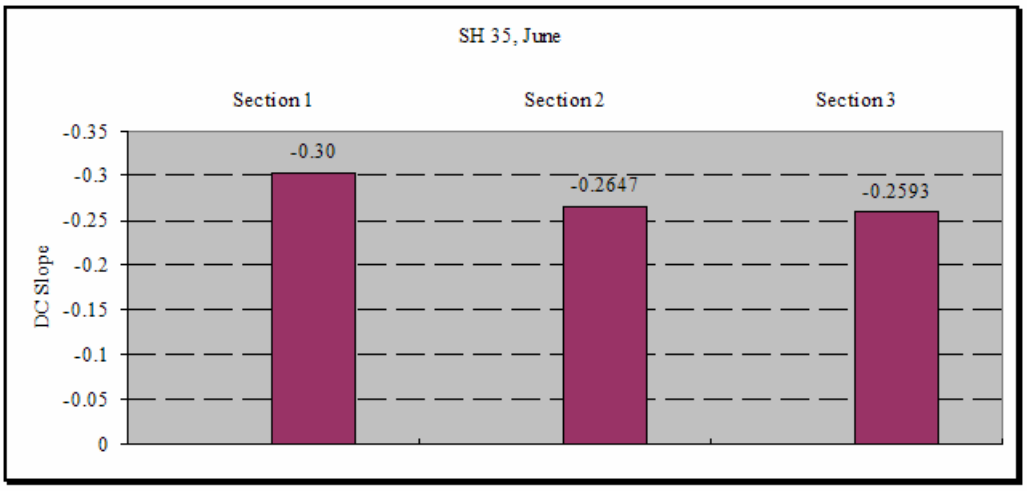

Fig. IV-33. DC Slopes for SH 35 Field Test (June)

FIELD TEST AT I 40 AMARILLO

An extensive field test was carried out on I 40 construction site, in Amarillo during the month of August 2006 to compare the effectiveness of high reflective curing compound, wax-based curing compound, and normal resin-based curing compound. Besides relative humidity and DC measurements, mortar cubes strength was obtained to justify the curing effectiveness from physical properties standpoint of view.

Six sections were investigated. The information for each section is present in Table IV-4. The effectiveness of single coat versus double coats was investigated. For this job site, normal resin-basined curing compound was used by the contractor so machine spray was adopted. It was not practical to switch tank on the machine to the wax-based curing compound and reflective curing compound, as a result hand spray was used for these two types of curing compounds.

Table IV-4. Facts in Each Section

	# of Coats	Type of Curing Compound	Application
Section 1	Single	Normal Resin-based	Machine
Section 2	Double	Normal Resin-based	Machine
Section 3	Single	Wax-based	Manual
Section 4	Double	Wax-based	Manual
Section 5	Single	High Reflective	Manual
Section 6	Double	High Reflective	Manual

Ambient Conditions

The ambient weather conditions were characterized by ACI 308. The potential of evaporation (PE) is shown in Fig. IV-34. The highest PE was about 0.40 lb/ft^2/hr. It dropped dramatically due to the rain.

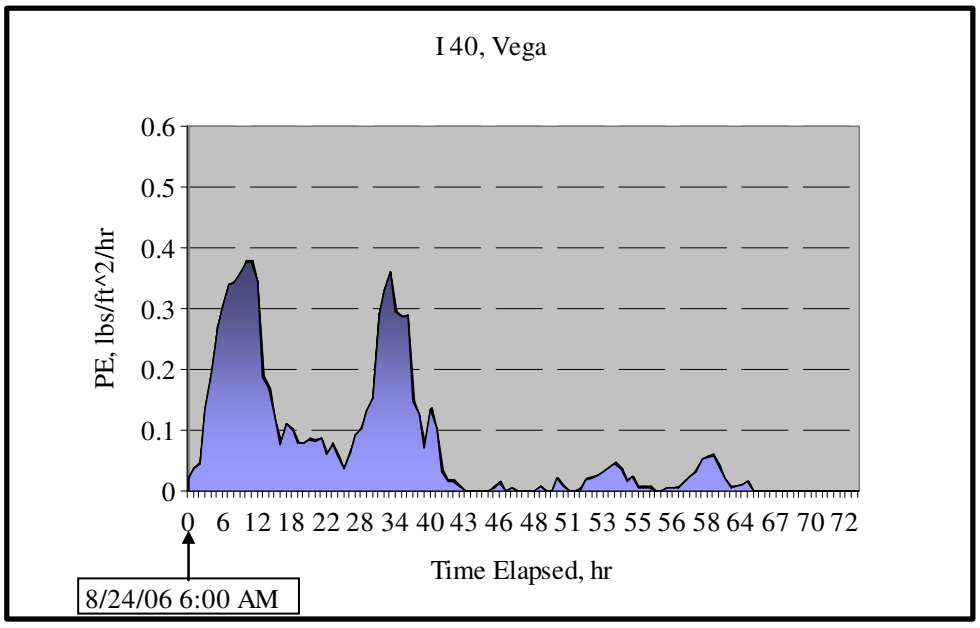

Fig. IV-34. Potential of Evaporation @ I 40

Data Presentation

Relative humidity data are presented in Fig. IV-35, Fig. IV-36, Fig. IV-37, Fig. IV-38, Fig. IV-39, and Fig. IV-40, respectively. The pink curves are surface relative humidity and the yellow curves are ambient relative humidity.

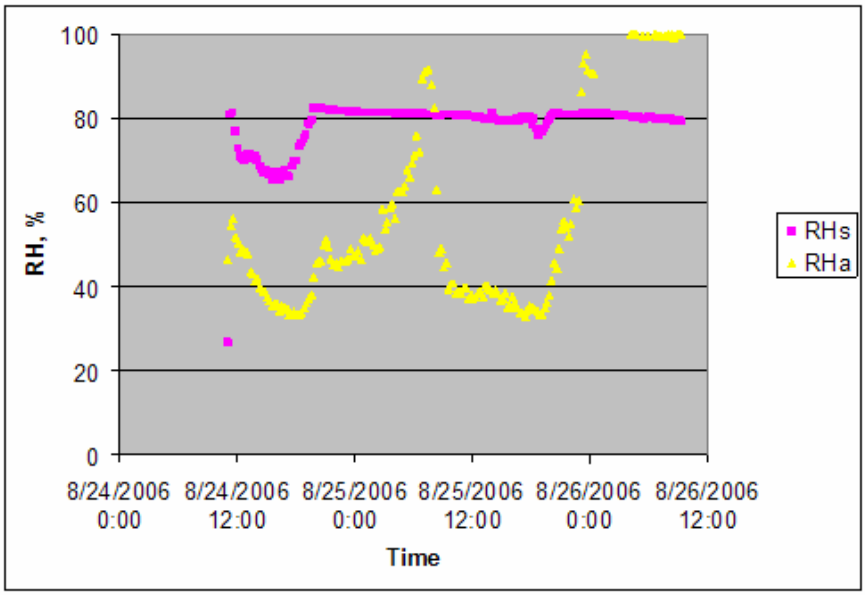

Fig. IV-35. Relative Humidities for Section 1 (I 40)

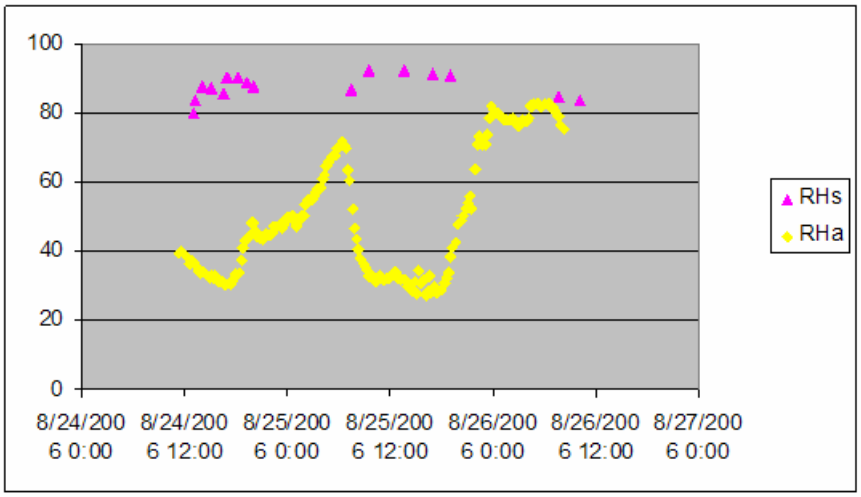

Fig. IV-36. Relative Humidities for Section 2 (I 40)

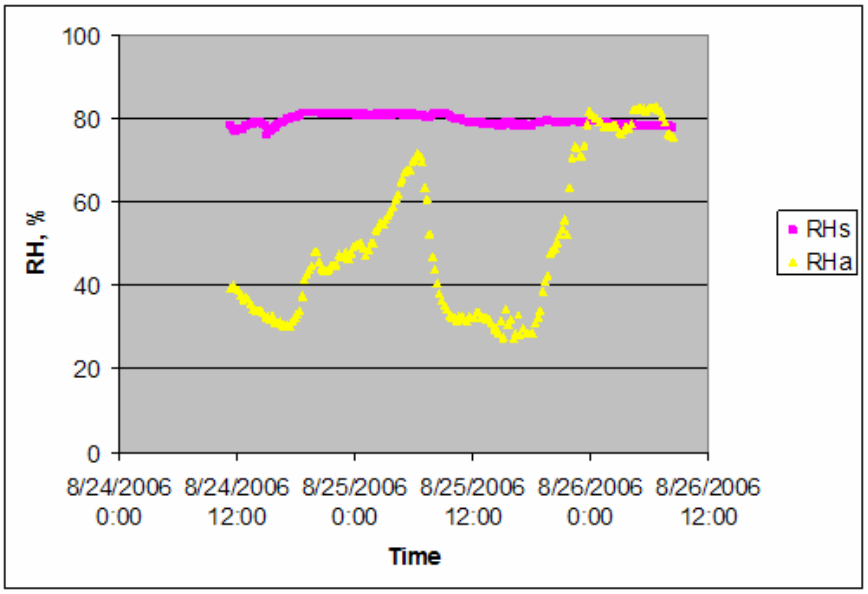

Fig. IV-37. Relative Humidities for Section 3 (I 40)

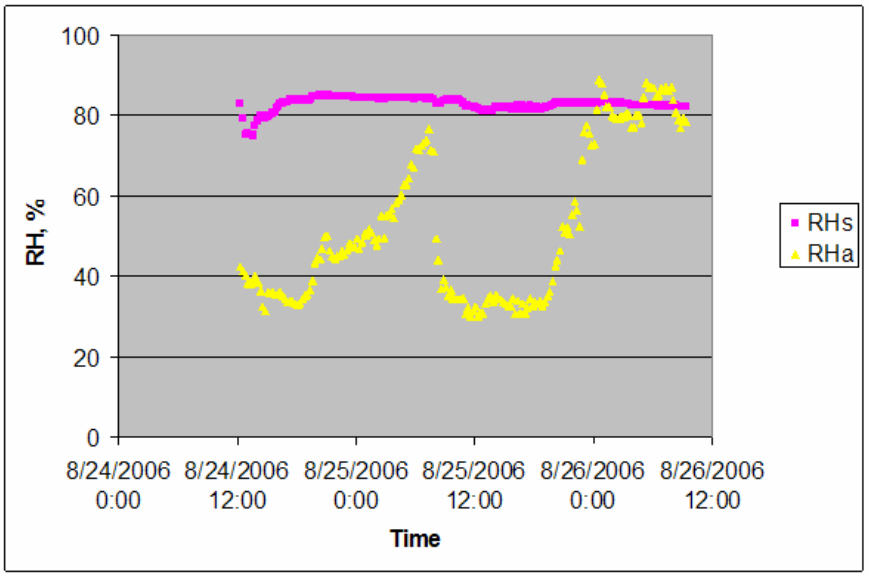

Fig. IV-38. Relative Humidities for Section 4 (I 40)

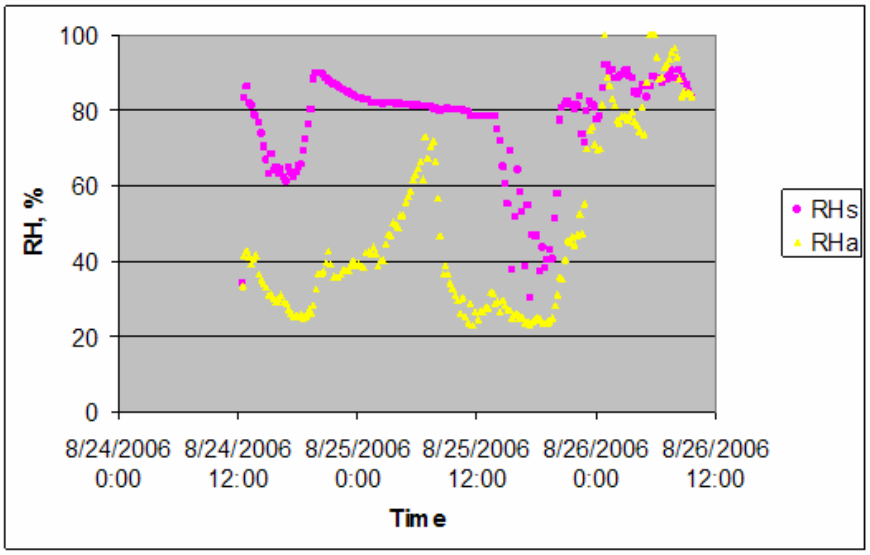

Fig. IV-39. Relative Humidities for Section 5 (I 40)

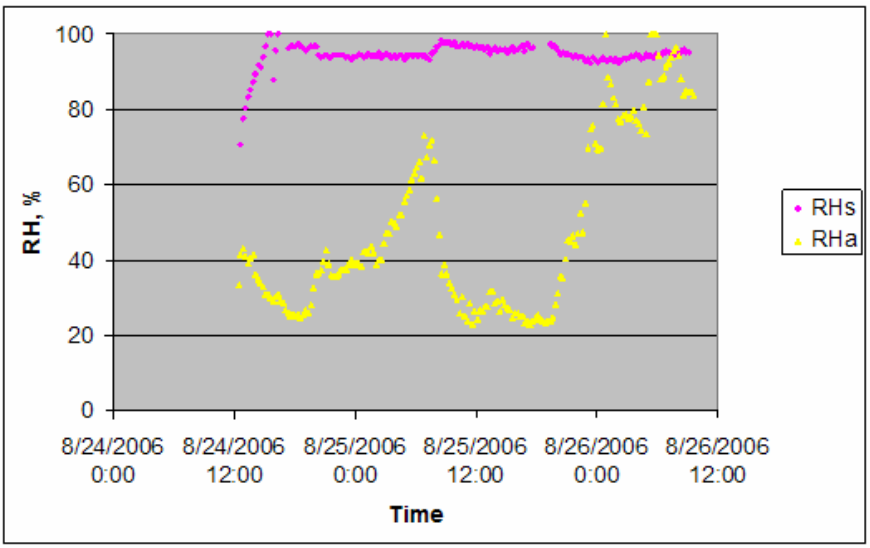

Fig. IV-40. Relative Humidities for Section 6 (I 40)

Surface relative humidity showed that the curing application for section 5 was bad. All other sections showed the surface humidities were above 80%, even the single coat of normal resin-based curing compound in section 1. This should be accredited to the machine spray, which is capable to apply a uniform curing membrane.

DC slopes were obtained for section 1, section 3, section 4, section 5, and section 6, shown Fig. IV-41. It is evident that double coats increased the curing quality, as also shown in the moisture data.

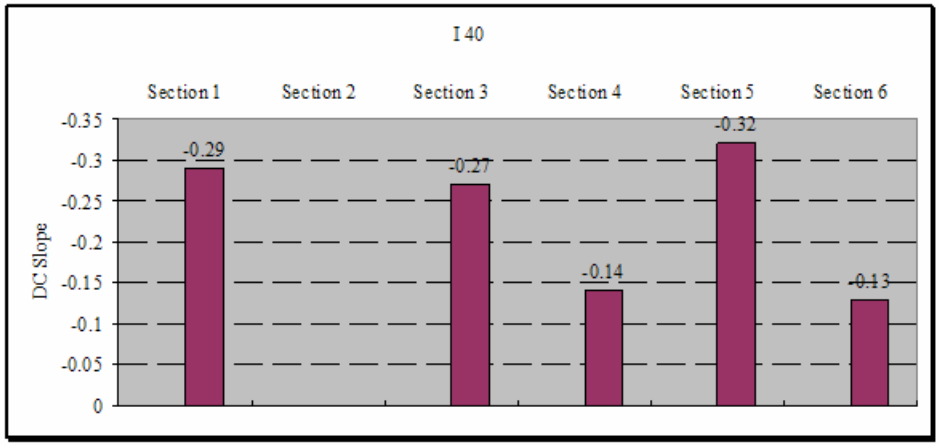

Fig. IV-41. DC Slopes for I 40 Field Test

Six sets of mortar cubes were prepared for each section. Three types of cubes were prepared for each section, shown in Fig. IV-42. Sealed specimens gave the strength under perfect curing conditions; curing compound cured specimens gave the actual strength by field curing; and the exposed specimens gave the strength under worst conditions. The curing effectiveness can be obtained from a relative scale (Fig. IV-43).

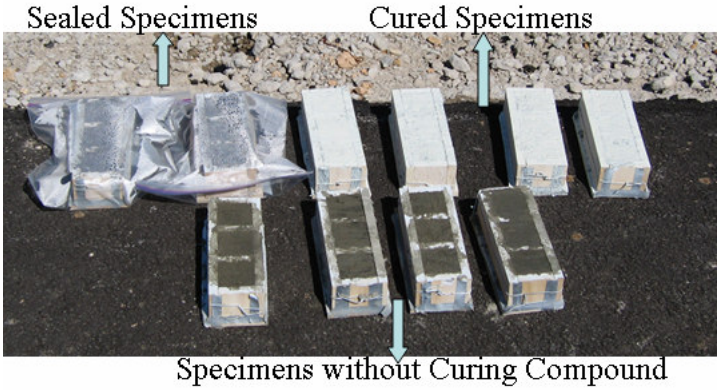

Fig. IV-42. Mortar Cubes

$$CE = \frac{S_C - S_E}{S_S - S_E}$$

Where,

S_C- strength of cured sample

S_E- strength of exposed sample

S_S- strength of sealed sample

Fig. IV-43. DC Slopes for I 40 Field Test

The mortar cubes were tested after curing in the field for 3 days. The results are presented in Fig. IV-44. As expected, the sealed specimens gave the highest strength while the exposed specimens gave the lowest strength.

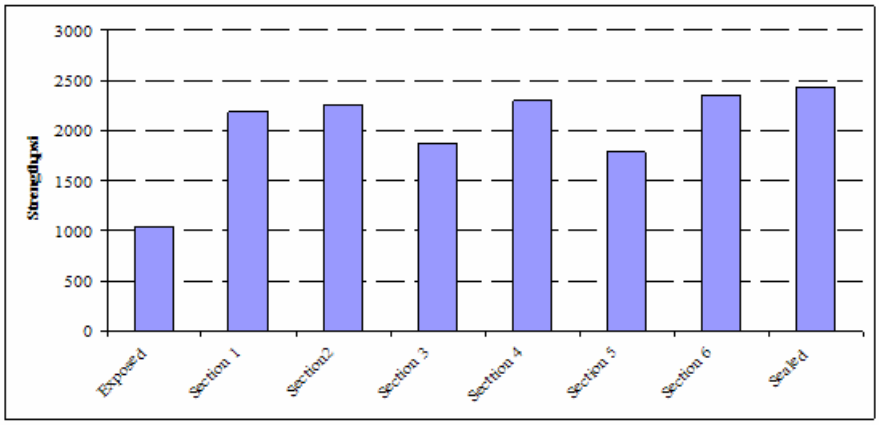

Fig. IV-44. Mortar Cube Strength (I 40)

The curing effectiveness (CE) was thus calculated. The CEs are presented in Fig. IV-45. The CEs for section 4 and section 6 were the best. However, the CEs for section 3 and section 5 were the worst. It should be noticed that manual spay was used from section 3 to section 6. Single coat of manual spray resulted in bad curing membrane uniformity and even high laboratory ranked curing compound without good application

can cause bad curing. On the other hand, the CE for section 1 indicates desirable good curing, even it was single coat application and low laboratory ranked curing compound was used. This concludes that uniformity of curing compound application is key to success in curing practice in the field.

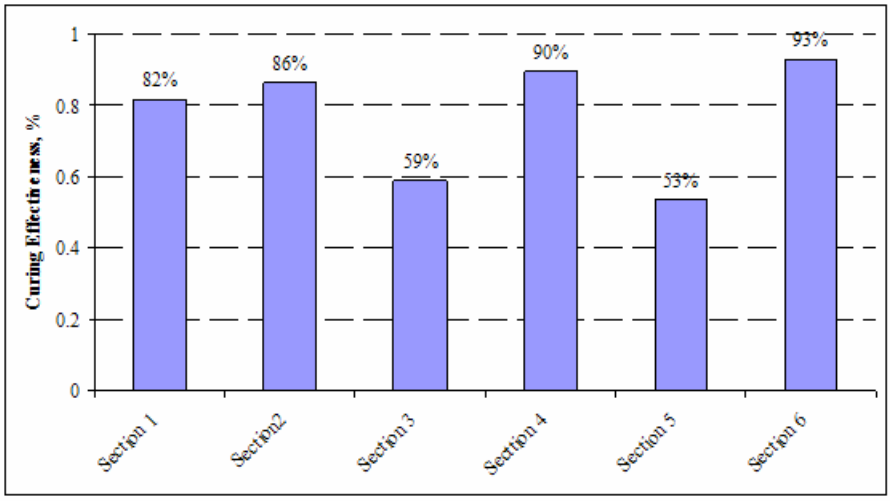

Fig. IV-45. Cure Effectiveness (I 40)

FIELD TEST AT US 290

Field test was carried out on US 290 construction site during the month of October 2006. Two sections were investigated. The application rate for section 1 was designed to 60 ft^2/gallon and it was 90 ft^2/gallon for section 2. The actual application rates were measured in the field.

Ambient Conditions

The ambient weather conditions were characterized by ACI 308. The potential of evaporation (PE) is shown in Fig. IV-46. The highest PE was about 0.20 lb/ft^2/hr.

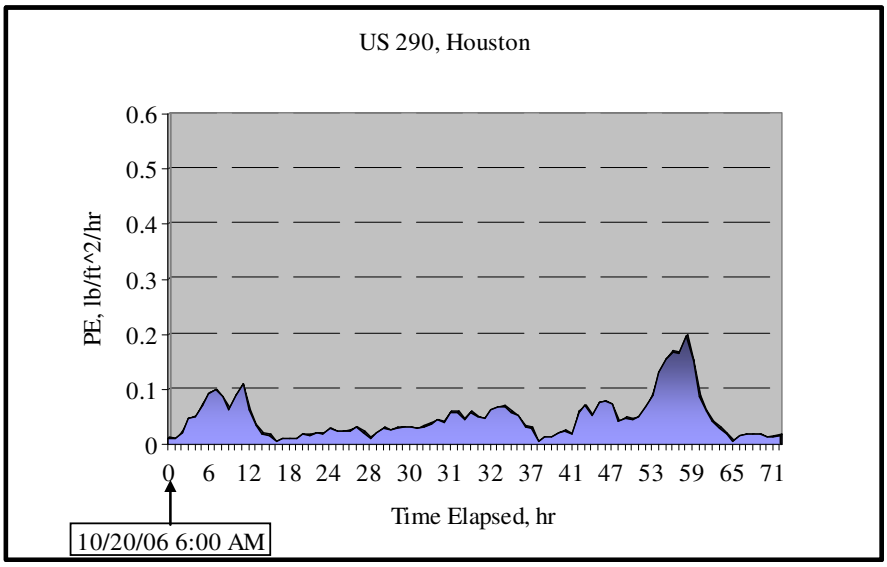

Fig. IV-46. Potential of Evaporation @ US 290

Data Presentation

Relative humidity data are presented in Fig. IV-47 and Fig. IV-48, respectively. Chilled mirror sensors were also inserted in the surface chamber to justify the measurements from the capacitance type of sensor.

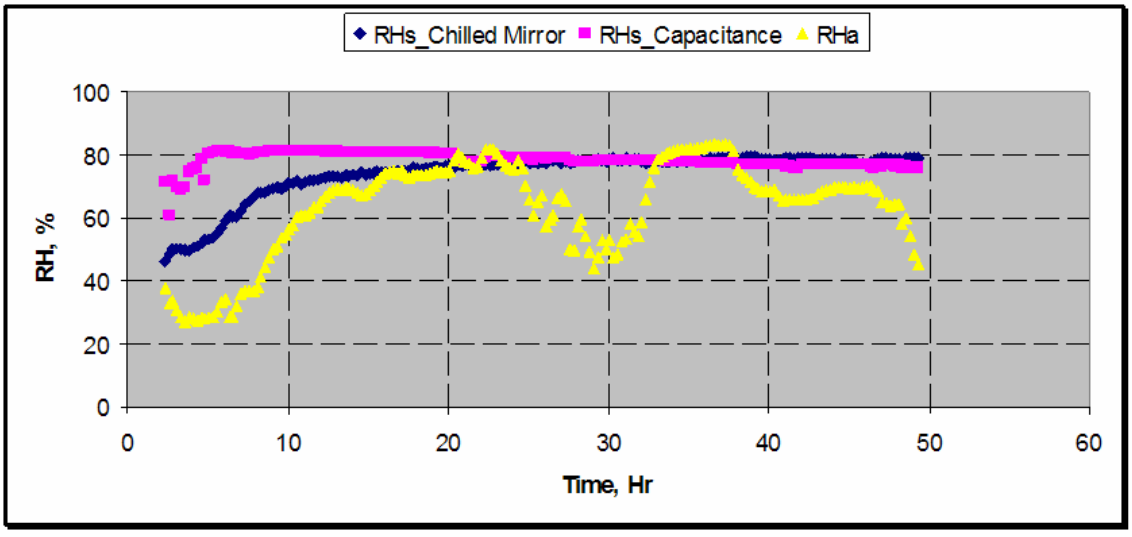

Fig. IV-47. Relative Humidities for Section 1 (US 290)

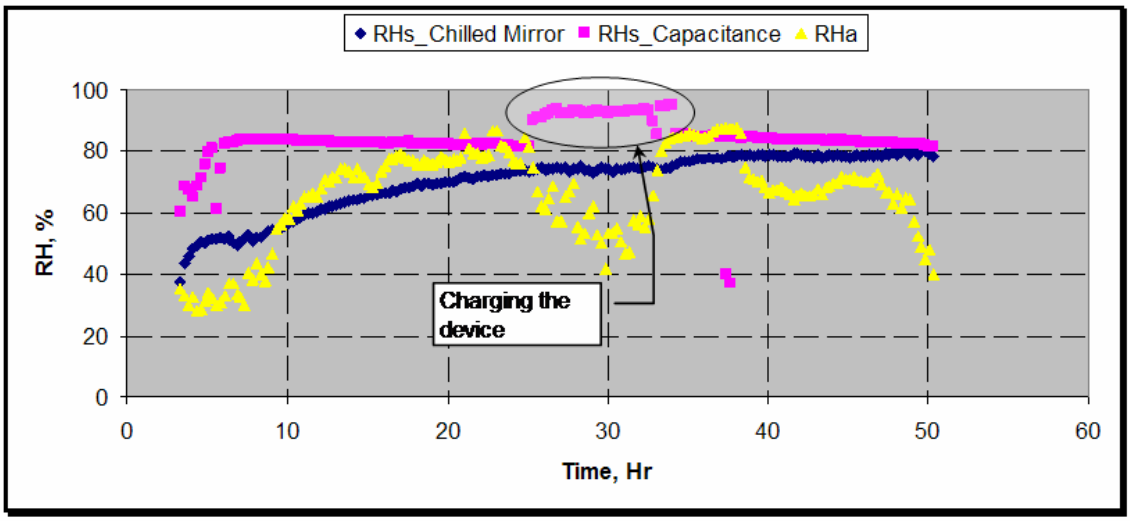

Fig. IV-48. Relative Humidities for Section 2 (US 290)

It is observed that chilled mirror measurements started off low but eventually matched with the measurements from the capacitance sensor. It is believed that the chilled mirror measures the true vapor pressure in the surface chamber. The moisture buildup in the chamber takes time. However, it is much saturated when concrete is fresh, so there is always water available to condense on the sensor. For capacitance type of sensor, it gives false reading once it is condensed with water; while for chilled mirror sensor, there is a heating and cooling system to maintain the water membrane on the mirror, thus it is capable of capturing the vapor buildup process.

DC slopes are presented in Fig. IV-49. Two slopes were obtained for each section. It is observed that the slopes of section1 are slightly smaller than those of section 2.

Application rates were measured in the field. Circular plates were to receive the curing compound sprayed from the machine, as shown in Fig. IV-50. The weights of plates were taken before and after the curing compound application. Table IV-5 is the calculation table. The application rate of section 1 was around 40 ft^2/gallon and the application rate of section 2 was around 60 ft^2/gallon.

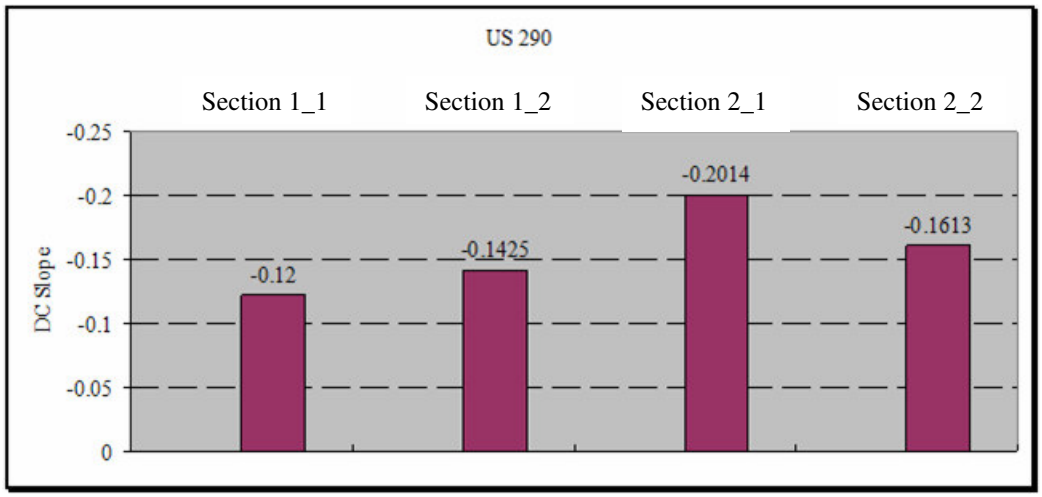

Fig. IV-49. DC Slopes for US 290 Field Test

Fig. IV-50. Plates for Application Rate Determination

Table IV-5. Application Rate Calculation

	Section I: 3 coats		Section II: 2 coats	
Initial Weight, Lbs.	0.0700	0.0700	0.0700	0.0700
Final Weight, Lbs.	0.1100	0.1075	0.0955	0.0975
Net Weight,Lbs	0.0400	0.0375	0.0255	0.0275
Dry weight, Lbs	0.0850	0.0865	0.0800	0.0800
Water Evaporated, Lbs	0.0250	0.0210	0.0155	0.0175
Area, ft^2	0.1963	0.1963	0.1963	0.1963
Density, Lbs/Gallon	8.3300	8.3300	8.3300	8.3300
Application, Gallon	0.0048	0.0045	0.0031	0.0033
Rate, ft^2/gallon	40.8898	43.6158	64.1409	59.4761
Rate per Application, ft^2/gallon	122.6694	130.8473	128.2817	118.9521

Mortar cubes were also prepared for this field test. Strength data and curing effectiveness are presented in Fig. IV-51 and Fig. IV-52, respectively. From the strength data, there is not much difference in curing effectiveness for the two sections, which implies that it is not beneficial and economical to apply too much curing compound as long as a uniform curing membrane is applied.

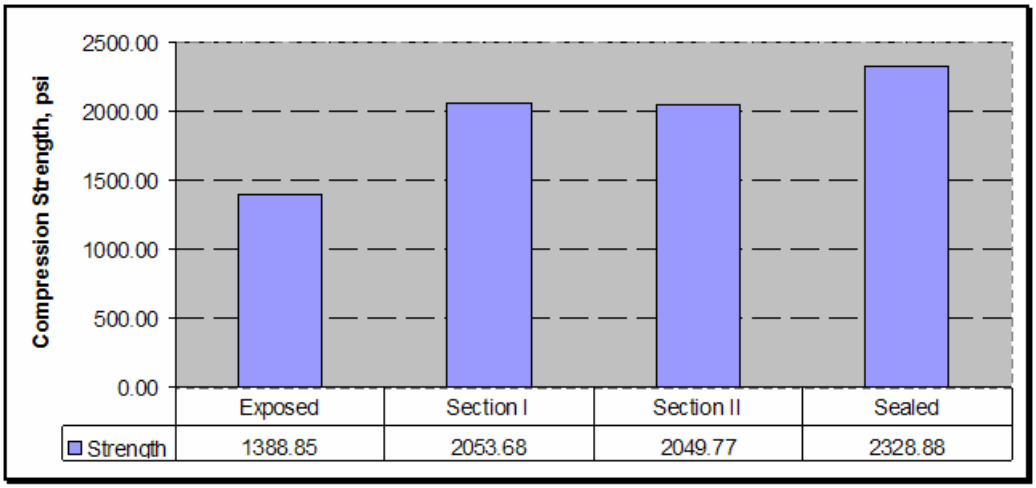

Fig. IV-51. Mortar Cube Strength (US 290)

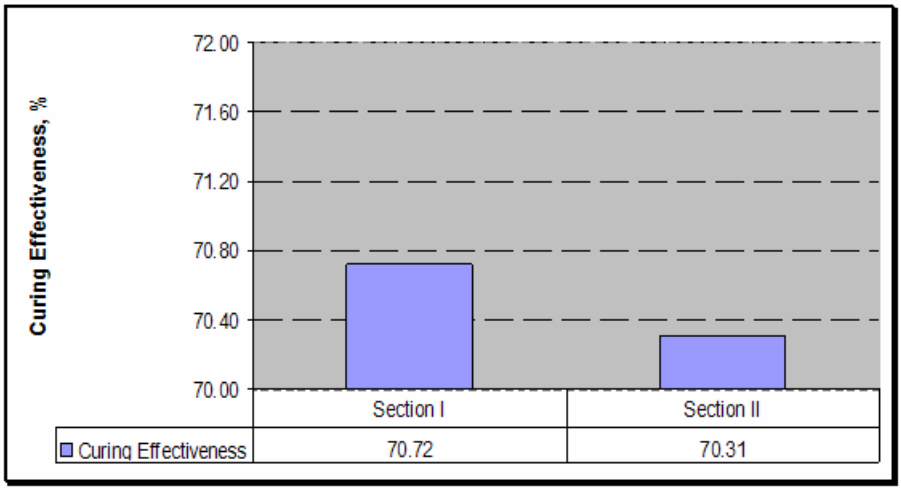

Fig. IV-52. Curing Effectiveness (US 290)

FIELD TEST SYNTHESIS

A comprehensive series of field tests have been conducted under the TxDOT Project 0-5106. Eight field tests were conducts comprising of a wide range of geographical locations and weather patterns in Texas. The geographical distribution of the field tests is illustrated in Fig. IV-53. Fig. IV-54 shows the accumulated PE for the all the field tests. The accumulated PE ranges from 3.09 lb/ft^2 (November of 2005) to 12.36 lb/ft^2 (August of 2006).

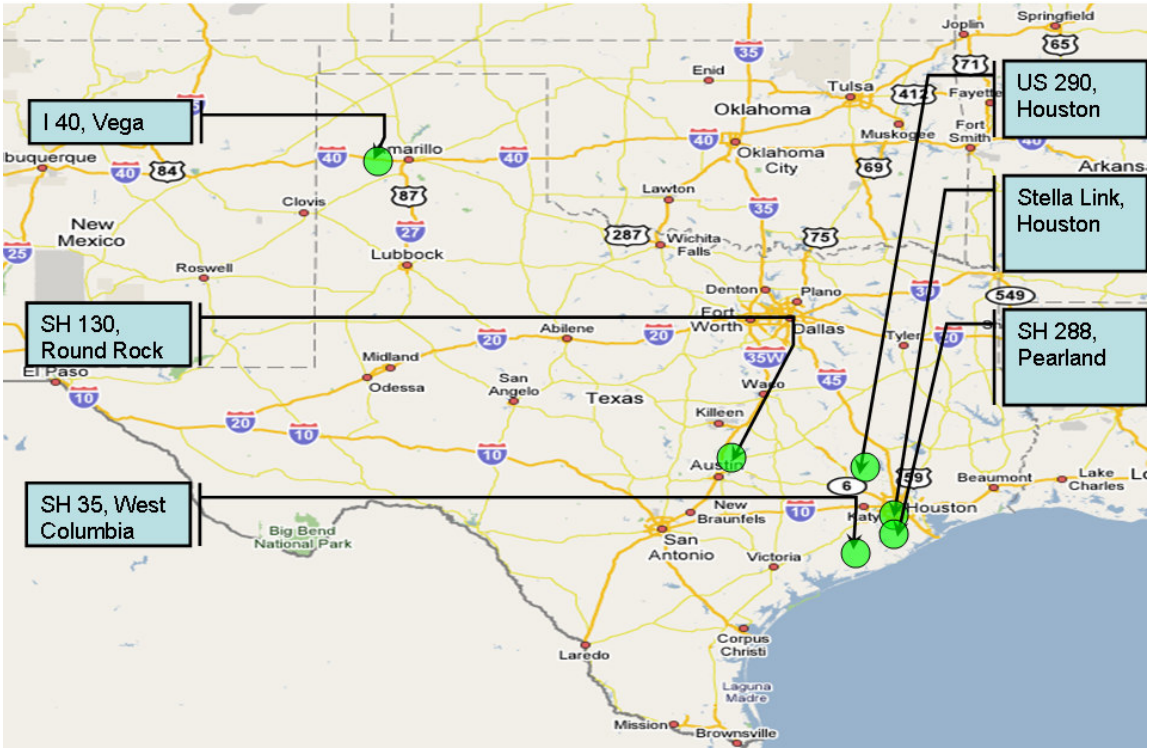

Fig. IV-53. Geographical Distribution of All Field Tests

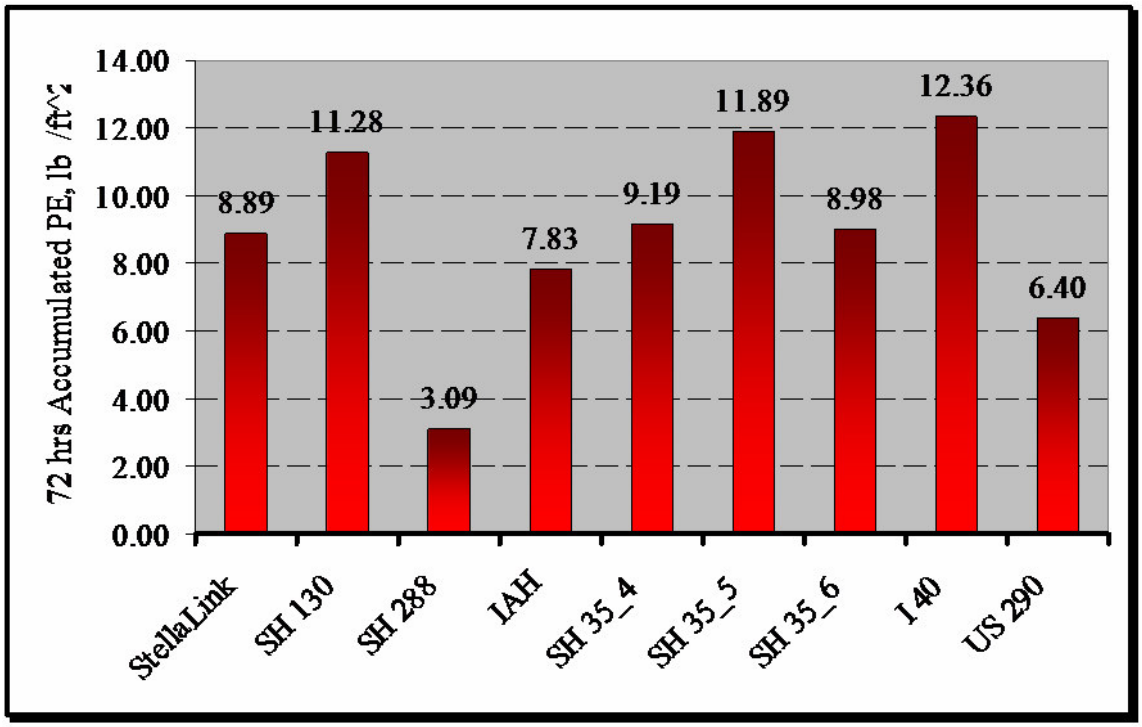

Fig. IV-54. Ambient Weather Conditions of All Field Tests

As stated earlier, the field curing effectiveness is dependent upon the curing compound quality, the curing application quality, and the ambient conditions. Each one of the three components needs to be satisfied to constitute a good field curing practice.

The findings are as follows:

- Uniformity of curing membrane is of most important factor affecting curing quality. Manual spray has higher possibility to result non-uniform curing membrane
- The second coat in the same day when concrete is placed helps to increase curing quality, especially for manual spray.
- Curing compound application in the second does not help to increase the curing quality.

SUMMARY

This chapter presents the data of all the field tests. A synthesis of all the field tests and findings are given in chapter as well.

CHAPTER V
TEMPERATURE AND MOISTURE ANALYSIS FOR CURING CONCRETE

Mechanistic models characterizing the behavior of on-site concrete are becoming more and more prevalent. This chapter integrates the most updated models about the early age concrete heat transfer and moisture transport. Thermal conductivity and moisture diffusivity are considered as a function of concrete temperature, concrete moisture and degree of hydration, which makes this nonlinear and coupled. The induction of moisture capacity in the formulation makes it possible to simulate the relative humidity drop due to self-desiccation. Since temperature and moisture would vary mostly in the vertical direction for concrete pavement, a one dimensional simplification is adopted. The finite element formulae are derived based on this simplification. At last, a full scale on-site early-age evaluation of concrete pavements is presented.

CONCRETE AGING CHARATERIZATION

The strength of concrete is a function of its age, temperature history and most probably the moisture history as well. The technique for estimating the strength development of concrete based on the temperature history is based upon maturity method (ASTM C 1074 1999). The equivalent age is an important concept, which is described in equation (V-1).

$$t_e = \int_0^t \beta_T \beta_{RH} dt \tag{V-1}$$

where

t_e = equivalent age,

β_T = temperature weighing factor based on, and

β_{RH} = moisture weighing factor.

Equation (V-2), which was suggested by Freiesleben Hansen and Pederson based on the Arrhenius equation, is one of the many models for β_T. The activation energy values range from 41,000 to 67,000 /mol (Carino 1991) and they vary depending on the type of cementitious materials in the mixture.

$$\beta_T = \exp\left(-\frac{E}{R}\left(\frac{1}{273+T}-\frac{1}{273+T_r}\right)\right) \tag{V-2}$$

where

T = concrete temperature, ºC,

T_r = reference temperature, ºC,

E = activation energy, J/mol, and

R = universal gas constant, 8.3144 J/(mol K).

β_{RH} is shown in equation (V-3), where RH is the concrete relative humidity, and a, b are adjustable coefficients. Bažant (1970) assigned a = 7.5 and b = 4, while Jeong (2003) reported that a = 5 and b =1 had better prediction. The illustration of β_{RH} vs. RH is shown in Fig. V-1.

$$\beta_{RH} = \frac{1}{1+(a-aRH)^b} \tag{V-3}$$

Degree of hydration α can be expressed in a couple of ways: the current strength over the ultimate strength, the hydrated cementious materials over the total cementious materials, the heat generated over the total heat etc. It is characterized by equation (V-4).

$$\alpha(t_e) = \alpha_u \cdot \exp\left(-\left(\tau/t_e\right)^{\beta}\right) \tag{V-4}$$

where

α_u = ultimate degree of hydration,

τ = hydration time parameter, hrs, and

β = hydration shape parameter.

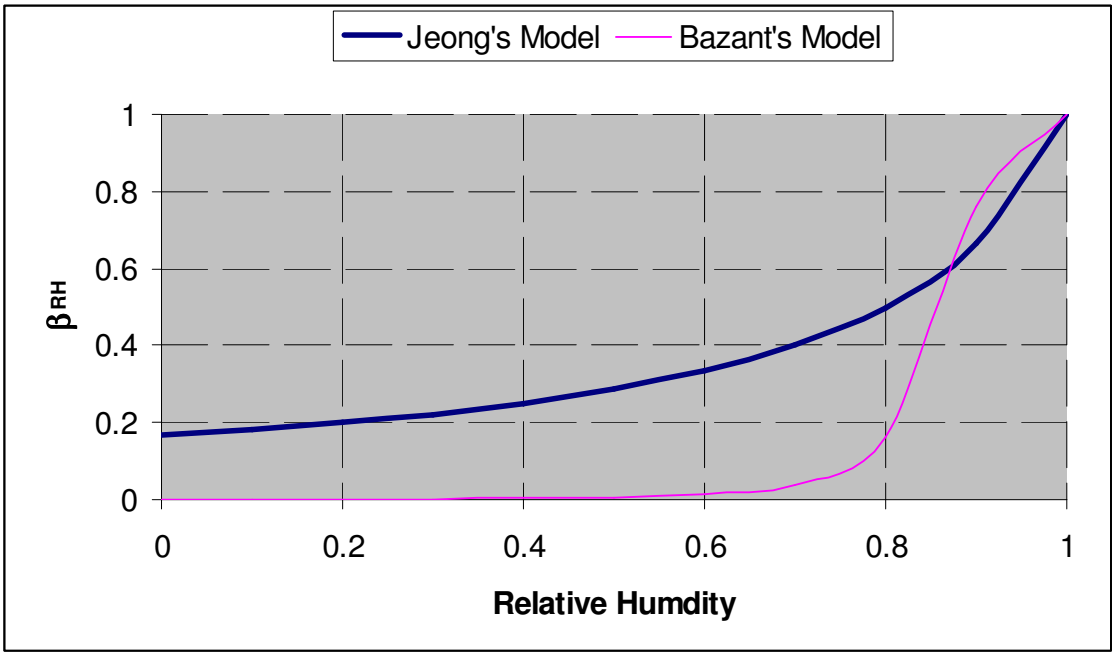

Fig. V-1. β_{RH} vs. RH

These parameters can be determined with the information of mixture design (Schindler and Folliard 2003). Since heat generation rate and self-desiccation rate are dependent on the derivative of degree of hydration with respect to time, this derivative is presented in equation:

$$\frac{\partial \alpha}{\partial t} = \frac{(\tau / t_e)^{\beta} \beta_T \beta_{RH} \alpha}{t_e} \tag{V-5}$$

CONCRETE TEMPERATURE

Concrete temperature is controlled mostly by the ambient weather conditions and the concrete thermal conductivity. If it is young concrete, the hydration process would affect the concrete temperature as well.

Governing Equation for Heat Transfer

From the view of conservation of energy, the governing equation for heat transfer inside a concrete body is formulated in equation (6).

$$div \cdot \left(K \cdot grad\left(T\right)\right) + Q = \rho c \dot{T} \tag{V-6}$$

where

K = thermal conducivity,

Q = heat generation rate by hydration,

ρ = concrete density, and

c = specific heat.

From the definition of degree of hydration, the total heat generated by hydration upon the time of t_e could be obtained from equation (V-7).

$$H = H_u \cdot \alpha\left(t_e\right) \tag{V-7}$$

where H_u is the total heat that can be generated and H is the heat generated. In order to get the heat generation rate, the equation (V-7) was taken the first derivative with respect to time. The heat generation rate was obtained as shown in equation (8).

$$Q = dH/dt = H_u \cdot \frac{\left(\tau/t_e\right)^{\beta} \beta_T \beta_{RH} \alpha}{t_e} \tag{V-8}$$

The boundary conditions for the heat transfer in young concrete have been discussed in the previous chapter.

CONCRETE MOISTURE

Governing Equation for Moisture Diffusion

Concrete moisture diffusion can be characterized by the law of conservation of moisture mass as shown in equation (19). The term on the left side states the moisture content change rate inside any point of a media while the first term on the right side represents the moisture content change due to moisture transport and the second term on the right side characterizes the moisture content change due to self-desiccation. In previous version of TMAC2, there are no inclusion of volume-gravimetric water content and hydrated volume-gravimetric water content in the formulation. Thus it was unable to predict the concrete relative humidity drop due to self-desiccation.

$$\frac{\partial \hat{\rho}}{\partial t} = div\left(\hat{\rho} \cdot D \cdot grad\left(RH\right)\right) + \frac{\partial \hat{\rho}_S}{\partial t} \tag{V-9}$$

where,

$\hat{\rho}$ = volume-gravimetric water content, g/cm^3,

D = moisture diffusivity, cm^2/sec,

$\hat{\rho}_S$ = hydrated volumetric water, g/cm^3, and

RH = relative humidity.

Equation (V-9) states that the moisture transport is governed by the differential of *RH*, which is an index of Gibbs free energy, and the change of moisture state at one point is affected by both the moisture transport and self-desiccation. Using chain rule, equation (V-9) is rewritten as:

$$\frac{\partial RH}{\partial t} = \frac{\partial RH}{\partial \hat{\rho}} div\left(\hat{\rho} \cdot D \cdot grad\left(RH\right)\right) + \frac{\partial RH}{\partial \hat{\rho}} \frac{\partial \hat{\rho}_s}{\partial t} \tag{V-10}$$

where $\frac{\partial RH}{\partial \hat{\rho}}$ is known as moisture capacity, which is discussed later.

Applying the concept of degree of hydration again, degree of hydration could be expressed as:

$$\alpha = \frac{\hat{\rho}_s}{\hat{\rho}_u} \tag{V-11}$$

where $\hat{\rho}_u$ is the total water needed for a full hydration. So equation (V-10) can be further revised into equation (18).

$$\frac{\partial RH}{\partial t} = \frac{\partial RH}{\partial \hat{\rho}} div\left(\hat{\rho} \cdot D \cdot grad\left(RH\right)\right) + \hat{\rho}_u \frac{\partial RH}{\partial \hat{\rho}} \frac{\partial \alpha}{\partial t} \tag{V-12}$$

where $\hat{\rho}_u$ is a constant for a certain type of concrete mixture and $\frac{\partial \alpha}{\partial t}$ is given in equation (V-5).

Composition in Hydrating Concrete

A fresh concrete mix contains aggregate, cement (or cementious materials), water and some voids that taking the volumetric space. The block diagram of Fig. V-2 illustrates the volumetric and gravimetric composition of a fresh concrete mix. As hydration is going on, cement combined with water produces hydration products. Approximately the combined water, determined under specified conditions, is 23% of the mass of the hydrated cement (Copeland and Hayes 1953), however, this ratio is as low as 18% if Type II cement is used. The hydration products take greater volume than the absolute volume of unhydrated cement but smaller volume than the sum of the volumes of the unhydrated

cement and the non-evaporable water (Neville 1996). The empirical equation to calculate the hydration products is shown in equation (V-13).

$$V_H = \left[V_C + (1 - VRR) \cdot V_W\right] \cdot \alpha \tag{V-13}$$

where,

V_H = the volume of hydration products,

V_C = the volume of hydrated cement in anhydrous state,

VRR = volume reduction ratio (0.254),

V_W = the volume of combined water, and

α = degree of hydration.

The reduction in volume due to hydration becomes capillary voids. Hydration products have a characteristic porosity of around 28% (Neville 1996), where gel water is held in even under very low relative humidity conditions, while capillary water disappears when relative humidity falls below about 45% (Verbeck 1955). This indicates gel water contributes little to the water vapor pressure inside concrete. The volume of gel water can be assessed by the equation (V-14).

$$\frac{V_G}{V_G + V_H} = GP \tag{V-14}$$

where,

V_G = the volume of gel water, and

GP = gel porosity.

As shown in Fig. V-2, the total volume of voids is the sum of the volumes of the empty voids and the evaporable water. Since the volume of hydration products is greater than that of the anhydrous cement, the total volume of the voids will decrease during the hydration process, as a result of which the concrete porosity is decreasing.

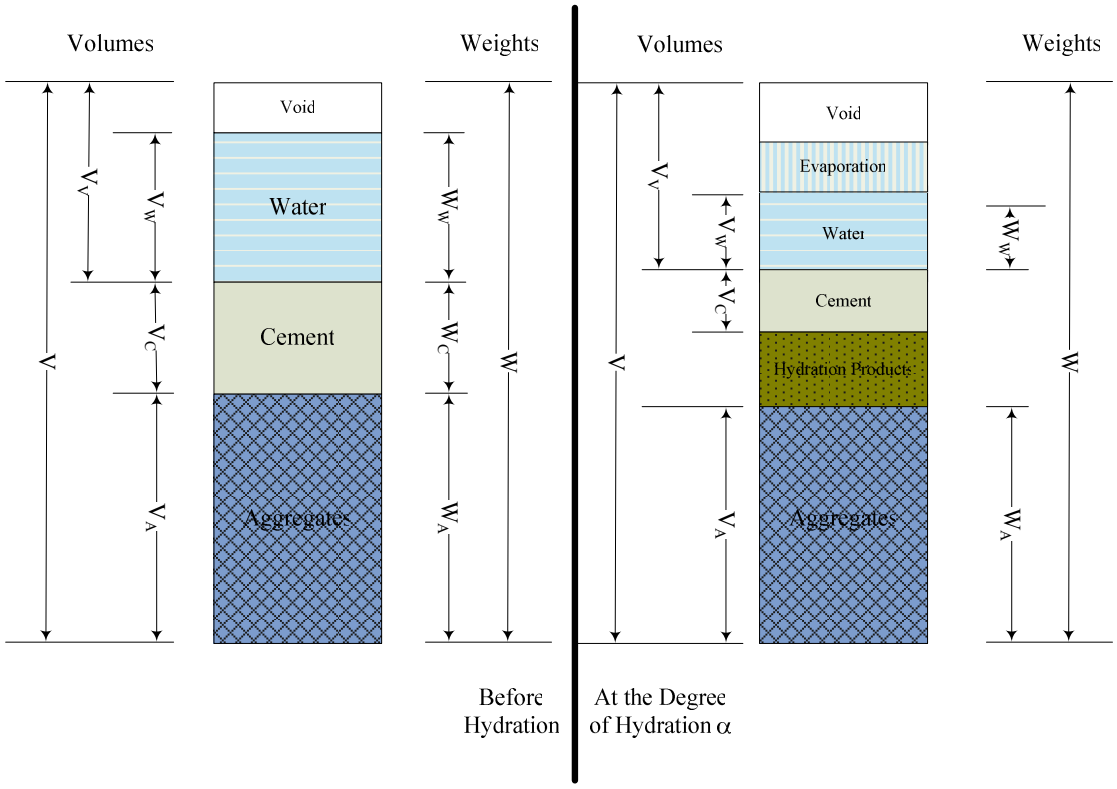

Fig. V-2. Block Diagram of Concrete Composition before and after Hydration

$$\theta = \frac{V_V^{'}}{V} = \frac{V_V - VRR \cdot V_W \cdot \alpha}{V} \tag{V-15}$$

where,

θ = concrete porosity.

The concrete porosity is given by equation (V-15). It is evident that the physical composition of young concrete is an evolving process. Even if the concrete porosity is decreasing, the water consumption due to hydration is faster so that the ratio of total evaporable water over total void is decreasing. This means that hydration process dries out the concrete (self-desiccation).

Moisture Capacity

Equation (V-12) requires the inclusion of moisture capacity, which is the relationship between relative humidity and water content within concrete at a constant temperature and the degree of hydration. The Brunauer-Emmett-Teller (BET) model is the best known isotherm model. However, it is claimed that the ranges of validity of BET model covers only from 0.01 to 0.1 (Gregg, Sing et al. 1967; Mikhail 1983). In this study, the three-parameter BET model is used.

$$W = \frac{CkV_m RH}{[1+(C-1)kRH](1-kRH)} \tag{V-16}$$

where

W = the quantity of water in grams of water per gram of cement paste,

k = is the third constant,

V_m = monolayer capacity,

C $= \exp\left(\frac{E_1 - E_l}{RT}\right)$,

E_1 = the total heat of adsorption per mole of vapor,

E_l = the latent heat of condensation per mole, and

R = the gas constant.

Xi, Bažant et al (1994) presented the models to characterize the parameters used in (V-17). The moisture capacity can be obtained by taking the first derivative of equation (V-17). Fig. V-3 shows the changing of moisture capacity due to aging of the concrete.

$$\frac{\partial RH}{\partial W} = \frac{CkV_m + Wk[1+(C-1)kRH] - Wk(1-kRH)(C-1)}{(1-kRH)[1+(C-1)kRH]} \tag{V-17}$$

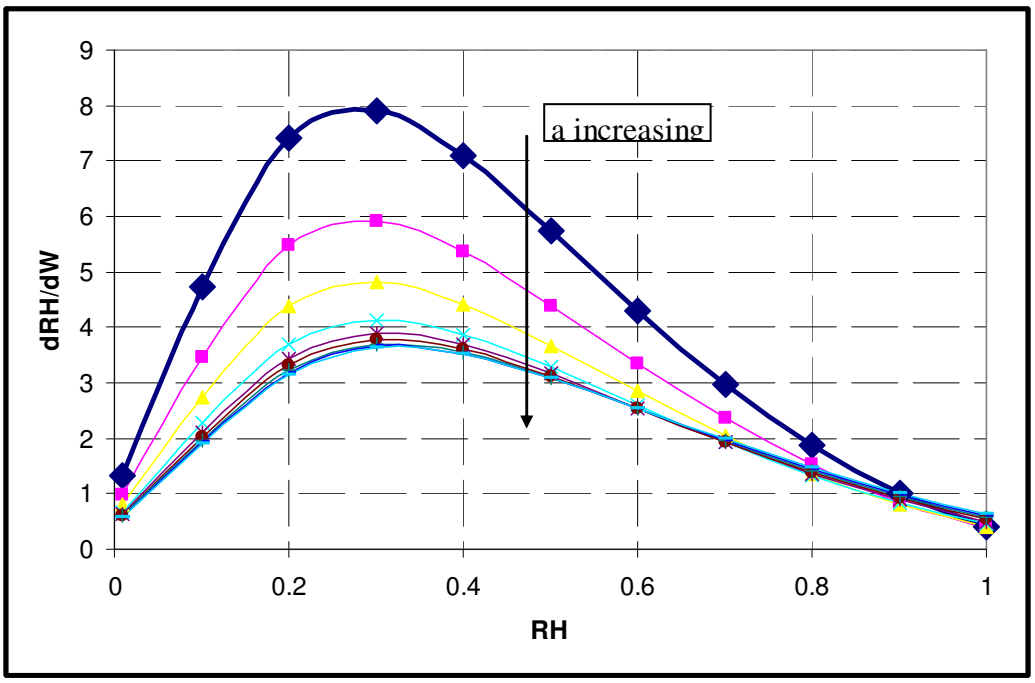

Fig. V-3. Effect of Age on Reciprocal of Moisture Capacity

FEM FORMULATION

Finite element method is a very powerful tool to solve differential equations based on variational principles. Since the temperature and moisture distributions in concrete are mostly dependent on the depth, it is thus simplified by assuming a one-dimension flow.

Variational Derivation

Variational derivation is very useful to derive finite element formulae. The one dimensional variation formulation of equation (V-6) is

$$\int \left[\frac{d}{dx}\left(K \frac{dT}{dx} \right) + Q - \rho c \dot{T} \right] \delta T dx = 0 \qquad \text{(V-18)}$$

By integrating by parts, equation (V-18) becomes:

$$\int\left[-K\frac{dT}{dx}\delta\left(\frac{dT}{dx}\right)+Q\delta T-\rho c\dot{T}\delta T\right]dx+K\frac{dT}{dx}\delta T\Big|_{x=a}^{x=b}=0 \qquad \text{(V-19)}$$

T is approximated by the following equation.

$$T=T_i^m N_i \qquad \text{(V-20)}$$

where N_i is the approximation function and T_i^m is the nodal temperature at time step m. The approximation of T in time dimension adopted forward finite difference formulation. So equation (21) becomes:

$$\int\left[KN_{ix}N_{jx}\right]dxT_j^m+\frac{\int\rho cN_iN_j dxT_j^{m+1}-\int\rho cN_iN_j dxT_j^m}{\Delta t}=\int QN_j dx \qquad \text{(V-21)}$$

where N_{ix} means the first derivative of N_i with respect to x and Δt is the time interval. It should be noticed that K and Q in the above the equation are not constant throughout the integrating domain. For the boundary terms, all the external heat at the boundary node should be added to the right side of equation (V-21) with accordance to the node number. To obtain the FEM formulae for moisture diffusision, the same process needs to be followed. The one dimensional variational formula of equation (V-16) is given by equation (V-22).

$$\int_a^b\left[\frac{\partial RH}{\partial t}-\frac{\partial RH}{\partial\bar{\rho}}\frac{\partial}{\partial x}\left(\bar{\rho}\cdot D\cdot\frac{\partial RH}{\partial x}\right)-\bar{\rho}_u\frac{\partial RH}{\partial\bar{\rho}}\frac{\partial\alpha}{\partial t}\right]\delta RHdx=0 \qquad \text{(V-22)}$$

Integrating by parts, equation (V-22) becomes:

$$\int \left[\begin{array}{l} -\dfrac{\partial RH}{\partial \hat{\rho}\cdot}\hat{\rho}\cdot D\dfrac{dRH}{dx}\delta\left(\dfrac{dRH}{dx}\right)-\dfrac{\partial^2 RH}{\partial\hat{\rho}\cdot\partial x}\hat{\rho}\cdot D\dfrac{dRH}{dx}\delta RH \\ +\hat{\rho}_u\cdot\dfrac{\partial RH}{\partial\hat{\rho}\cdot}\dfrac{\partial\alpha}{\partial t}\delta RH-\dfrac{dRH}{dt}\delta RH \end{array} \right] dx \\ +\frac{\partial RH}{\partial\hat{\rho}}\hat{\rho}\cdot D\frac{dRH}{dx}\delta RH\Big|_{x=a}^{x=b}=0 \tag{V-23}$$

Because the moisture capacity is function of *x*, the resulting diffusivity matrix becomes nonsymmetrical. *RH* is approximated by the following equation.

$$RH = RH_i^m N_i \tag{V-24}$$

where N_i is the approximation function and RH_i^m is the nodal relative humidity at time step m. Again use forward difference method to approximate the first derivative of *RH* with respect to time.

$$\int\left[\frac{\partial RH}{\partial\hat{\rho}}\hat{\rho}\cdot DN_{ix}N_{jx}+\frac{\partial^2 RH}{\partial\hat{\rho}\,\partial x}\hat{\rho}\cdot DN_iN_{jx}\right]dxRH_j^m \\ +\frac{\int N_iN_j dxRH_j^{m+1}-\int N_iN_j dxRH_j^m}{\Delta t}=\int\hat{\rho}_u\frac{\partial RH}{\partial\hat{\rho}}\frac{\partial\alpha}{\partial t}N_j dx \tag{V-25}$$

Shape Functions and Matrix Formulation

Quadratic functions are used as shape functions. Fig. V-4 illustrates a one-dimension quadratic element with a length of 2a. It comprise of three nodes with two nodes at both ends and one node in the middle. The shape functions are presented in equation (V-26), (V-27), and (V-28), respectively. N_1 is for the nodal on the left, N_2 is for the node in the middle, and N_3 is for the node on the right. Fig. V-5 shows the plots of the shape functions.

Fig. V-4. Quadratic Element.

$$N_1 = \frac{1}{2a^2} x(x-a) \tag{V-26}$$

$$N_2 = -\frac{1}{a^2}(x+a)(x-a) \tag{V-27}$$

$$N_3 = \frac{1}{2a^2} x(x+a) \tag{V-28}$$

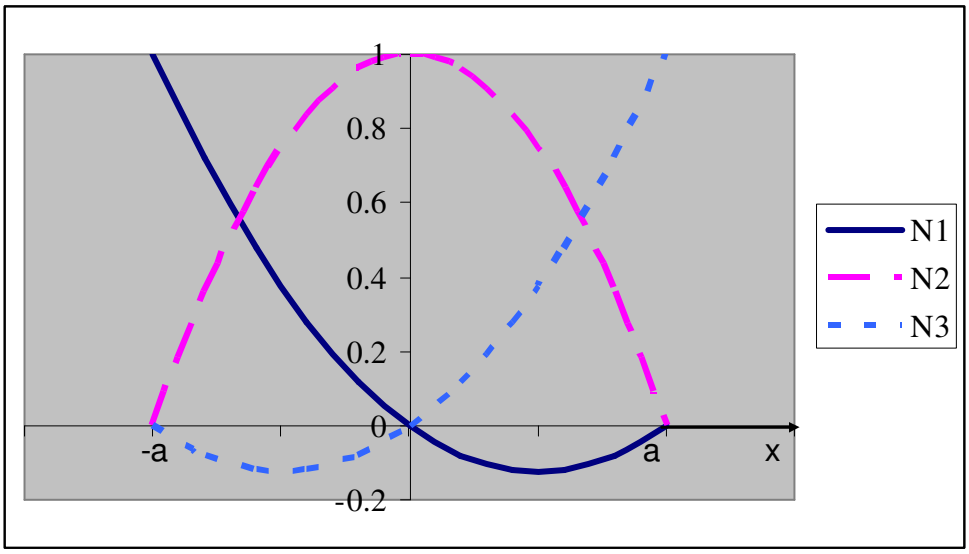

Fig. V-5. Quadratic Shape Functions

It is observed from equation (V-21) and (V-25) that there are four types of integrations needed to be evaluated, as shown from equation (V-29) through (V-32).

$$\int_{-a}^{a} UN_{ix}N_{jx}dx \tag{V-29}$$

$$\int_{-a}^{a} UN_{i}N_{j}dx \tag{V-30}$$

$$\int_{-a}^{a} UN_{j}dx \tag{V-31}$$

$$\int_{-a}^{a} UN_{i}N_{jx}dx \tag{V-32}$$

where U is a dummy term and a function of x. For example, U is replaced by K in order to evaluate the first term of equation (V-21). For simplicity, U is approximated by shape functions as well.

$$U = U_i N_i \tag{V-33}$$

U_i is evaluated at each node. The explicit form of equation (V-29) is given as matrix in equation (V-34).

$$\begin{bmatrix} \frac{1}{60}\frac{37U_1+36U_2+3U_3}{a} & -\frac{1}{15}\frac{11U_1+8U_2+U_3}{a} & \frac{1}{60}\frac{7U_1-4U_2+7U_3}{a} \\ -\frac{1}{15}\frac{11U_1+8U_2+U_3}{a} & \frac{4}{15}\frac{3U_1+4U_2+3U_3}{a} & -\frac{1}{15}\frac{U_1+8U_2+11U_3}{a} \\ \frac{1}{60}\frac{7U_1-4U_2+7U_3}{a} & -\frac{1}{15}\frac{U_1+8U_2+11U_3}{a} & -\frac{1}{60}\frac{3U_1-36U_2-3U_3}{a} \end{bmatrix} \tag{V-34}$$

The U term in equation (V-30) is constant throughout the integrating domain. As a result, equation (V-30) gives a simpler matrix as shown in equation (V-35).

$$U\begin{bmatrix} \frac{4}{15}a & \frac{2}{15}a & -\frac{1}{15}a \\ \frac{2}{15}a & \frac{16}{15}a & \frac{2}{15}a \\ -\frac{1}{15}a & \frac{2}{15}a & \frac{4}{15}a \end{bmatrix} \tag{V-35}$$

The right sides of equation (V-21) and (V-25) can be evaluated by equation (V-36).

$$\begin{bmatrix} \frac{1}{15}a(4U_1 + 2U_2 - U_3) \\ \frac{2}{15}a(U_1 + 8U_2 + U_3) \\ \frac{1}{15}a(-U_1 + 2U_2 + 4U_3) \end{bmatrix} \tag{V-36}$$

Equation (V-32) gives a non-symmetric matrix as shown in equation (V-37).

$$\begin{bmatrix} -\frac{1}{3}U_1 - \frac{1}{5}U_2 + \frac{1}{30}U_3 & \frac{2}{5}U_1 + \frac{4}{15}U_2 & -\frac{1}{15}U_1 - \frac{1}{15}U_2 - \frac{1}{30}U_3 \\ -\frac{1}{5}U_1 - \frac{8}{15}U_2 + \frac{1}{15}U_3 & \frac{4}{15}U_1 - \frac{4}{15}U_3 & -\frac{1}{15}U_1 + \frac{8}{15}U_2 + \frac{1}{5}U_3 \\ -\frac{1}{30}U_1 + \frac{1}{15}U_2 + \frac{1}{15}U_3 & -\frac{4}{15}U_2 - \frac{2}{5}U_3 & -\frac{1}{30}U_1 + \frac{1}{5}U_2 + \frac{1}{3}U_3 \end{bmatrix} \tag{V-37}$$

COMPUTER IMPLEMENTATION

This section discusses the basic steps involved in the development of TMAC^2 program. Most FEM programs include three parts: preprocessor, processor, and postprocessor. TMAC^2 also has these three parts.

The flow chart of TMAC^2 is presented in Fig. V-6. The preprocessor phase of TMAC^2 includes the input of geometry & mesh, materials, initial conditions & boundary conditions, and analysis duration & start time. In the processor phase, the nodal variables are first updated according to the initial conditions. Then element conductivity matrix and diffusivity matrix are calculated based on the updated nodal variables.

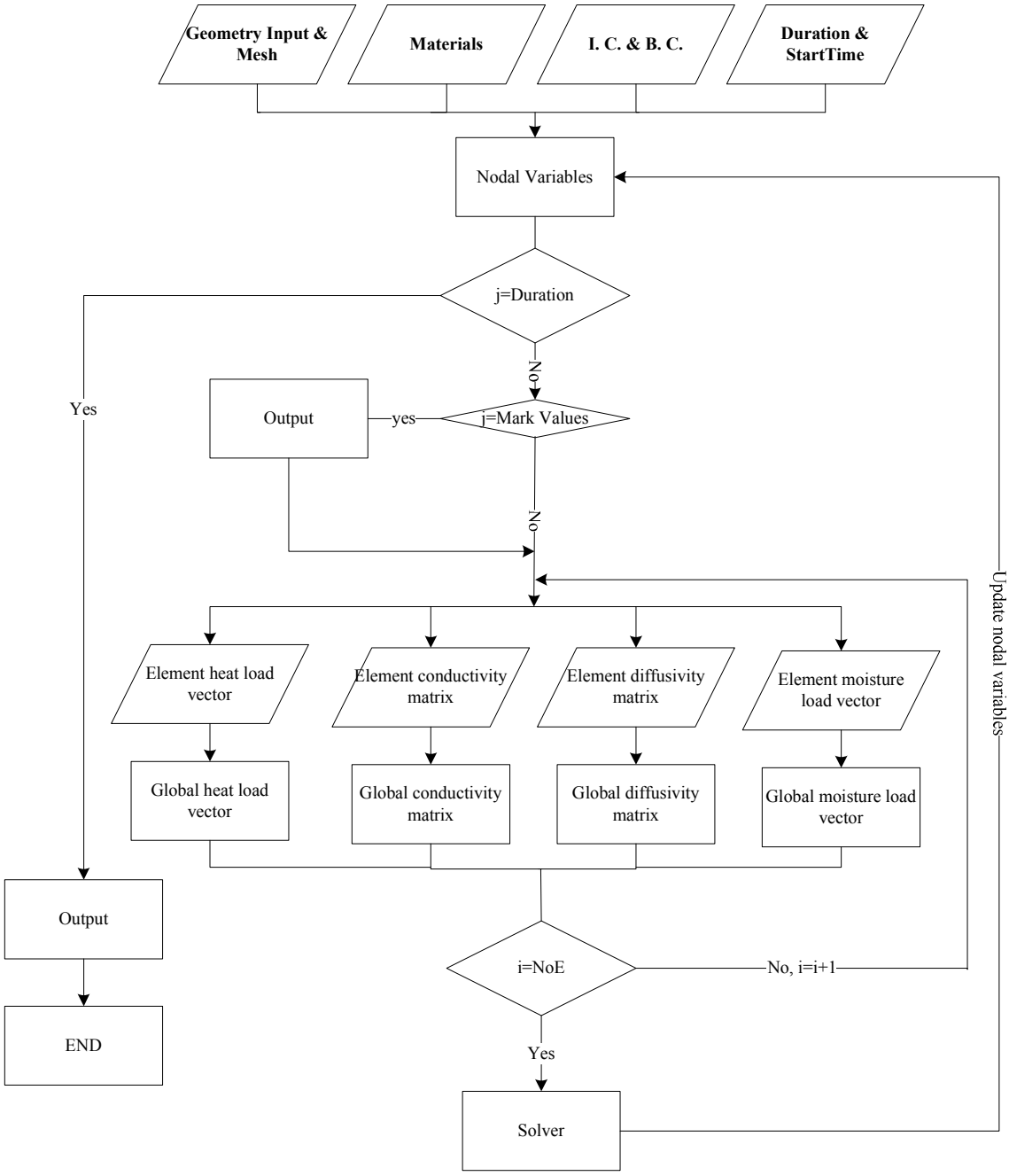

Fig. V-6. Flow Chart of TMAC[2]

The global matrixes and load vectors are assembled thereafter. The solution of the nodal variables is echoed so that the conductivity and diffusivity matrixes are

updated synchronically. The program ends when the analysis duration is reached and the nodal variables are recorded in the output file.

A FULL SCALE ON-SITE EARLY-AGE EVALUATION OF CONCRETE PAVEMENTS

A full scale concrete test pavement was cast at the FAA National Airport Pavement Test Facility (NAPTF) near Atlantic City, New Jersey to investigate the fatigue life of a two-layer concrete pavement structure with variable thicknesses. There were three structural configurations, which were 6" + 9" (section 1), 7.5 + 7.5" (section 2), and 9" + 6" (section 3) as shown in Fig. V-7. An asphalt bond breaker was placed between the concrete layers so that the assumption of relatively unbounded conditions between the layers can be established.

TTI was asked to assist in the monitoring of the on-site curing history and characterization of early-age concrete behavior. Penetration testing (ASTM C 803 1999) and free shrinkage testing (ASTM C 157 1999) were conducted. The following lists the measurements and tests conducted by TTI:

- Relative humidity monitoring in three sections,
- Penetration testing, and
- Free shrinkage testing.

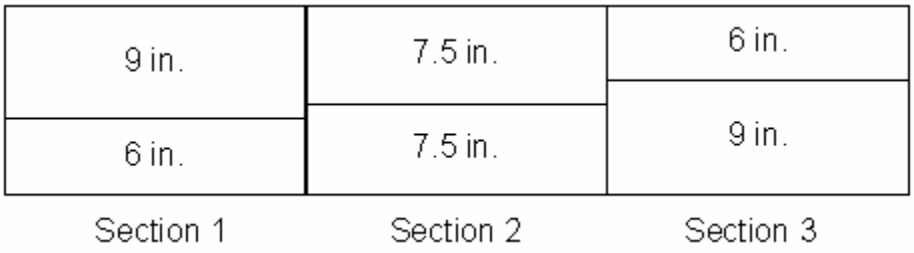

Fig. V-7. Diagram of Concrete Pavement Configuration

Instrumentation and Test Setup

Curing Monitor System (CMS) was used to monitor relative humidity at three different vertical locations. It has three relative humidity sensors to measure ambient relative humidity, concrete surface humidity and concrete relative humidity. The on-site setup is shown in Fig. V-8.

Fig. V-8. On-site CMS Setup

ASTM C803 (1999) *Standard Test Method for Penetration Resistance of Hardened Concrete* was conducted to determine the initial setting and final setting of the on-site concrete mix. The test set up is shown in Fig. V-9.

Vibrating wire gage EM-5 (Fig. V-10) was used to measure the free shrinkage strain (ASTM C 157 1999), which is a volumetric internal strain due to moisture loss. Relative humidity measurement was taken within the same specimen in order to establish the relationship between moisture content (relative humidity) and shrinkage. The setup is shown in Fig. V-11.

Fig. V-9. Penetration Test Setup

Fig. V-10. Vibrating Wire Gage EM-5

Fig. V-11. Free Shrinkage Test Setup

Data Presentation

Results of penetration, free shrinkage and relative humidity monitoring are presented in this section. These results are used to determine the final concrete set maturity, establish the relationship between free shrinkage and relative humidity, and to carry out an assessment of curing quality.

Penetration Test

A penetration specimen was prepared on Feb. 27th, but due to the low temperature conditions, the concrete strength development was delayed during the first day after placement. All penetration resistance data points were obtained in the second day after concrete placement. According to the specifications (ASTM C 803 1999), the resistances for initial and final set are 450 psi and 4000 psi respectively. The resulting initial set maturity was 295 $^{\circ}$C-hr and the final set maturity was 395 $^{\circ}$C -hr. The penetration test results relating penetration resistance and concrete maturity are presented in Fig. V-12.

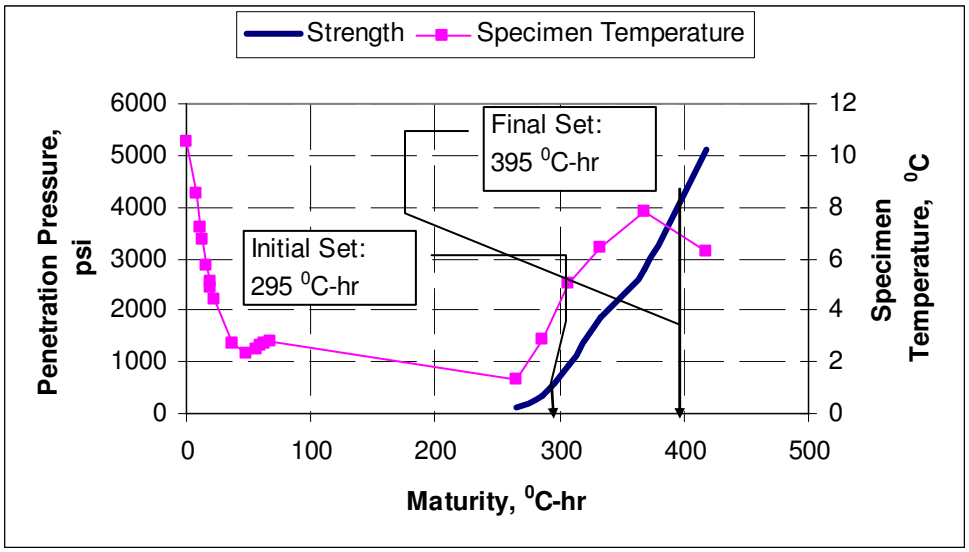

Fig. V-12. Penetration Test Results

Free Shrinkage Test

The ASTM C 157 (1999) was employed to measure the shrinkage due to moisture loss. A relative humidity sensor was inserted in the specimen to acquire moisture data and a vibrating wire gage was embedded inside the specimen, so that the correlation of relative humidity and shrinkage could be established. This relationship appeared to be linear based on the regressed test results with a R^2 of 0.97 (Fig. V-13).

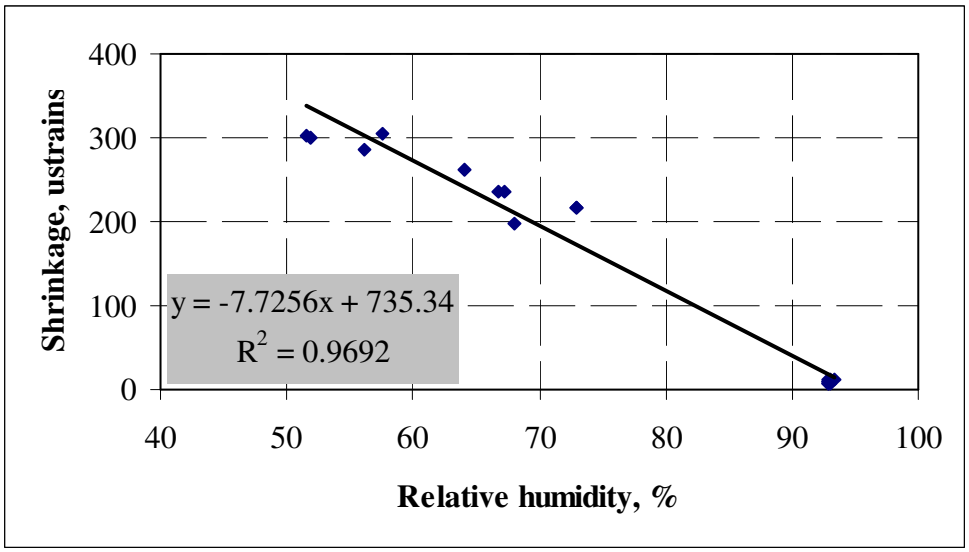

Fig. V-13. Free Shrinkage vs. Relative Humidity

Relative Humidity Data

Four sets of curing data were obtained: the lower layer and upper layer surfaces in section 1, and the lower layer and upper layer surfaces in section 2. A Type I (transparent type) of curing compound was spayed about 45 minutes after concrete placement. After final set, a small amount of water was sprayed on the concrete surface to keep the concrete moist and then plastic sheets were used to cover the concrete pavement surface.

For each set of curing data, relative humidity data at three different locations is presented. As has been observed many times before, the concrete relative humidity started low even if the concrete is in a fresh state, because the build-up of the relative humidity takes time. However, during the hardening stage the vapor pressure does increase as the concrete matures. The surface relative humidity remained rather constant around 80% for all four instances (Fig. V-14, Fig. V-15, Fig. V-16, and Fig. V-17), which can be accredited to the use of plastic sheeting. Experience as indicated from several field tests where the curing medium consisted of only curing compound the surface relative humidity reduces significantly during the second day after concrete

placement and tends to follow the trends of the ambient relative humidity. Due to the controlled environment where the concrete was placed, the ambient relative humidity trends were not entirely normal but reached the lowest point during noon time when the ambient temperature was the highest, but it began to increase as ambient temperature decreased. This ambient relative humidity cycling phenomenon is caused by the fact that the capacity of air is dependent on the air temperature. The air with higher temperature has higher moisture capacity to hold water vapor. The amount of water vapor in the air for the most part remains unchanged through out the day. The relative humidity is the ratio of the water vapor pressure divided by the saturated vapor pressure. Therefore, the relative humidity changes inversely with the air temperature.

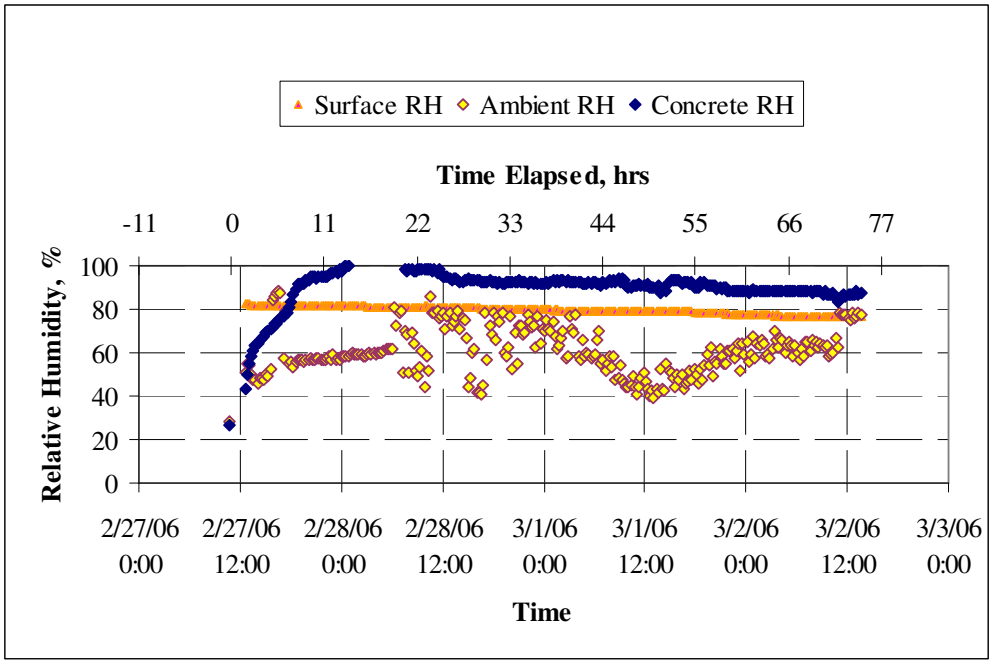

Fig. V-14. Relative Humidity @ the Lower Layer of Section 1

Low ambient relative humidity, high wind speed, high temperature and high solar radiation creat conditions for a high rate of evaportation. Normally, the worst combination occurs during afternoon hours. Placement of the concrete inside a controlled environment eliminated the influence of wind and solar radiation. The air

temperature was around 40 °F to 50 °F during the lower layer placement and 45°F to 70°F during the upper layer placement. Due to these conditions, low PE were expected.

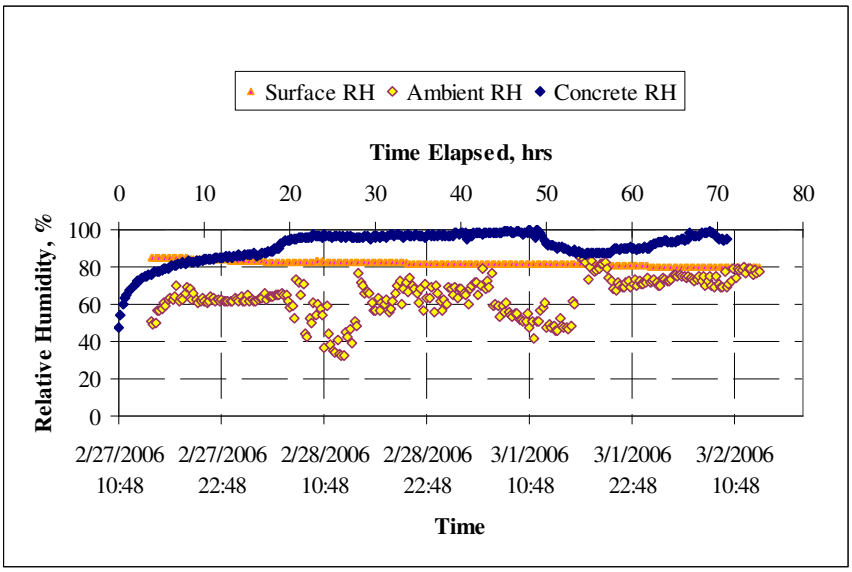

Fig. V-15. Relative Humidity @ the Lower Layer of Section 2

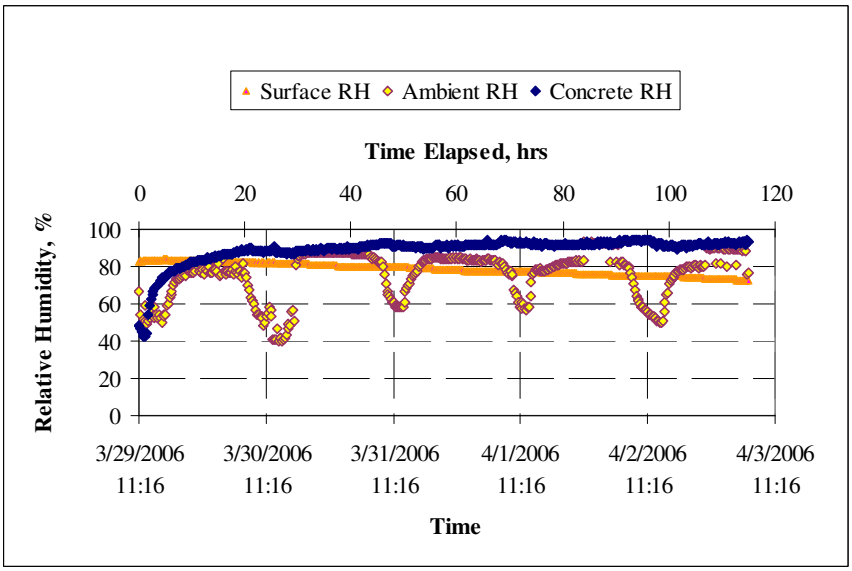

Fig. V-16. Relative Humidity @ the Upper Layer of Section 1

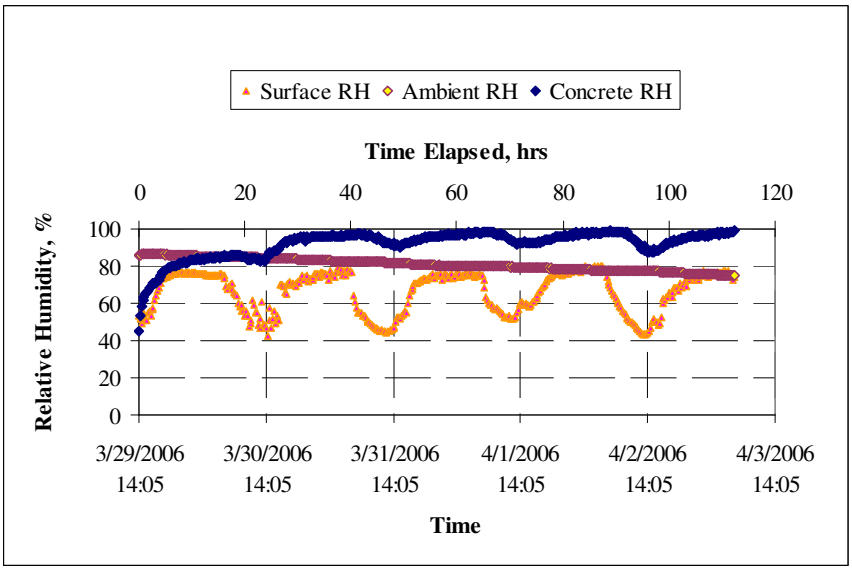

Fig. V-17. Relative Humidity @ the Upper Layer of Section 2

TMAC^2 Analysis

At the bottom layer of section 3, temperature and moisture data at 1", 3", and 7" were measured. These measured data were used to backcalculate the material properties (thermal conductivity and moisture diffusivity).

Hydration Parameters

Water cement ratio was 0.50. Hydration parameters listed in Table V-1 are selected based on the water cement ratio and the type of cement.

Table V-1. Hydration Parameters

Total Heat	436.1	J/g
Cement Content	0.32	g/cm^3
Activation Energy	39.184	KJ/mol
Ultimate Hydration, α	0.893	
β	0.785	
τ	37.87	

Ambient Conditions

Ambient temperature, ambient relative humidity, wind speed and solar radiation are four main factors that affect the temperature and moisture distribution inside concrete pavement. The test road was cast inside NAPTF facilities; therefore wind speed and solar radiation were assigned zeros for the TMAC^2 analysis. Ambient temperature and relative humidity were modeled as sine functions for each day. The recorded average daily high and low ambient temperature and relative humidity are presented in Table V-2.

Table V-2. Averaged Daily High and Low Values for Temperature and RH

	2/27 to 3/2		3/29 to 4/3	
	T, ºC	RH, %	T, ºC	RH, %
High	10	85	20	80
Low	5	40	12	40

The highest temperature occurred at 2:00 PM each day and the relative followed the inversed trend of the ambient temperature. The ambient temperature and relative humidity for two testing periods are plotted in Fig. V-18 and Fig. V-19, respectively.

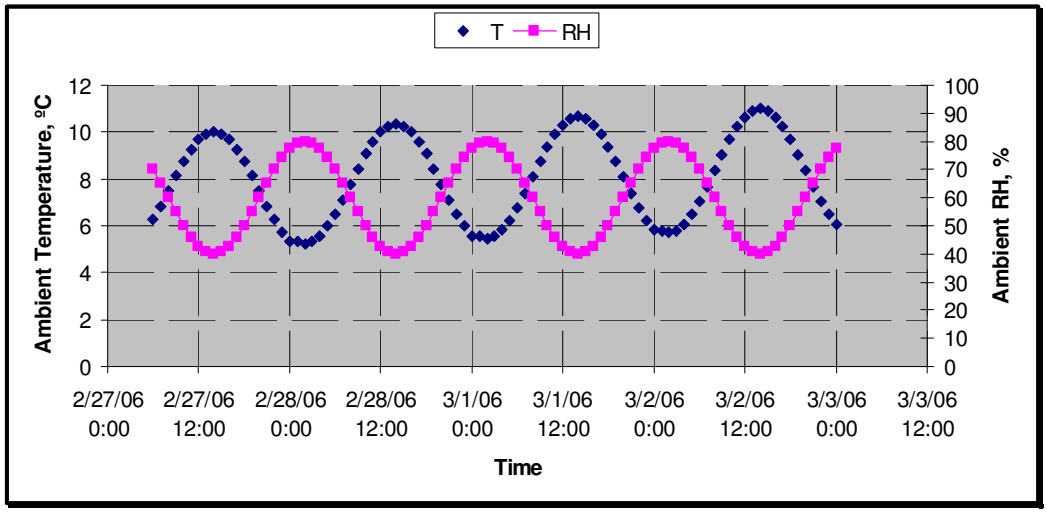

Fig. V-18. Ambient Temperature and Relative Humidity from 2/27/06 to 3/3/06

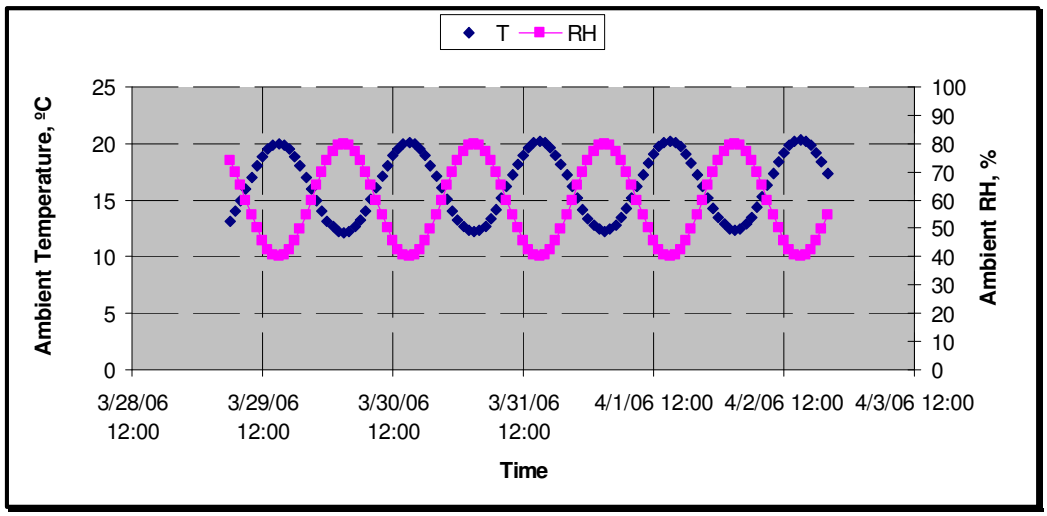

Fig. V-19. Ambient Temperature and Relative Humidity from 3/28/06 to 4/3/06

Thermal Conductivity and Moisture Diffusivity

Concrete thermal conductivity and moisture diffusivity are believed to be functions of the state of concrete temperature, relative humidity and degree of hydration. The following equations (V-38) and (V-39) are the proposed models for the thermal conductivity and moisture diffusivity.

$$K = (a - b\alpha)(0.0212T + 0.5321)(1.25RH^2 + 0.25RH + 0.5) \quad \text{(V-38)}$$

where,

K = thermal conductivity, J/(cm·hr·ºC),

a,b = adjustable coefficients,

α = degree of hydration, and

T = temperature, ºC.

$$D = (c - d\alpha)(0.0212T + 0.5321)(1.25RH^2 + 0.25RH + 0.5) \quad \text{(V-39)}$$

where,

D = thermal conductivity, cm^2/hr, and

c, d= adjustable coefficients.

The coefficients a, b, c, and d are adjusted by fitting the TMAC[2] predicted concrete temperature and relative humidity results to the measured concrete temperature and relative humidity data. The calibrated coefficients are listed in Table V-3.

Table V-3. Calibrated Coefficients

a	196.000
b	49.000
c	10.808
d	10.294

Fig. V-20, Fig. V-21, and Fig. V-22 show how degree of hydration, temperature, and relative humidity affect the concrete thermal conductivity (K) and moisture diffusivity (D). As concrete matures, the concrete porosity decreases, as a result the moisture diffusivity decreases. The decrease of thermal conductivity due to concrete aging can be explained by the decreasing moisture diffusivity and it mitigating effect on the transfer of heat. As temperature increases, both thermal conductivity and moisture diffusivity increase similar to the case when RH is increasing.

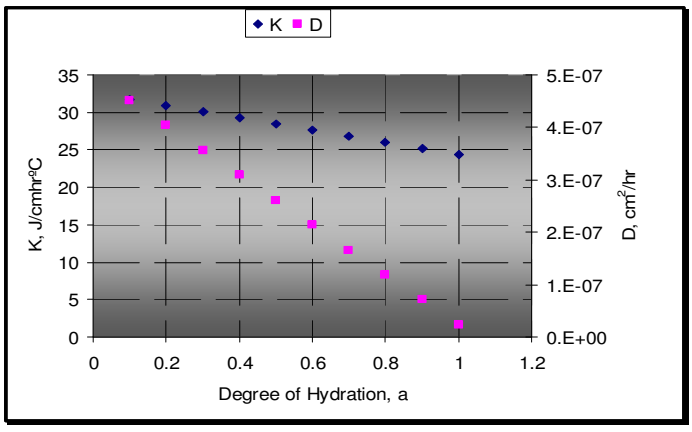

Fig. V-20. α's Effect on K & D (T=20ºC and RH=0.9)

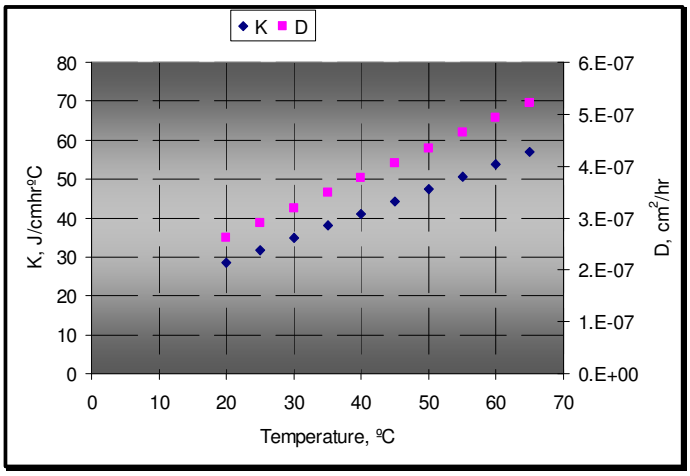

Fig. V-21. T's Effect on K & D (α=0.5 and RH=0.9)

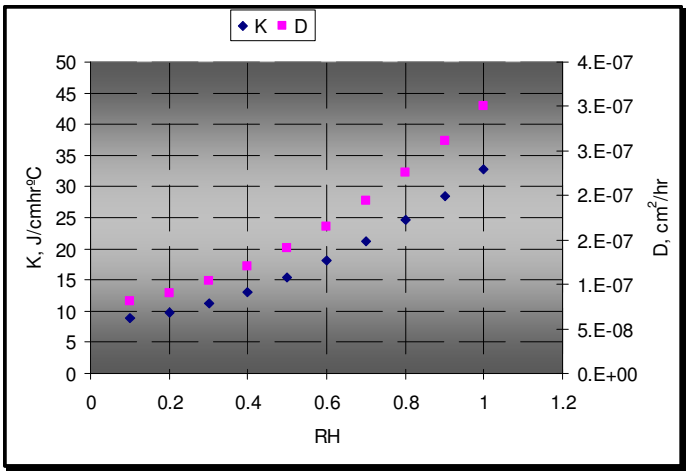

Fig. V-22. RH's Effect on K & D (α=0.5 and T=20°C)

From Fig. V-20 (T=20°C and RH=0.9), it is observed that the thermal conductivity drops from 33 J/cmhr°C to 24 J/cmhr°C, and moisture diffusivity drops from 4.6×10^{-7} to 0.3×10^{-7} cm^2/hr. Fig. V-21 (α=0.5 and RH=0.9) shows that thermal conductivity increases from 30 J/cmhr°C to 55 J/cmhr°C and the moisture diffusivity increases from 2.5×10^{-7} to 5.0×10^{-7} cm^2/hr with the temperature increasing from 20°C to 60°C. Fig. V-22 (α=0.5 and T=20°C) shows the effect of RH on thermal conductivity and moisture diffusivity. With RH changing from 0.2 to 1.0, the thermal conductivity

increases from 8 J/cmhrºC to 33 J/cmhrºC, and the moisture diffusivity increases from 0.8×10^{-7} cm^2/hr to 3×10^{-7} cm^2/hr.

Using adjusted K and D, the comparison between the predicted temperature history and measured temperature histories at different locations are presented in Fig. V-23, Fig. V-24, and Fig. V-25, respectively.

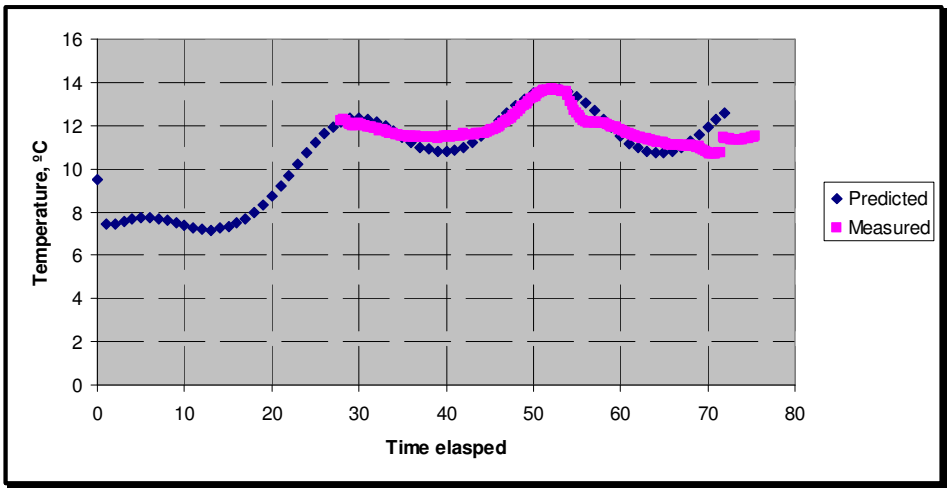

Fig. V-23. Temperature Histories Comparison at 1 Inch

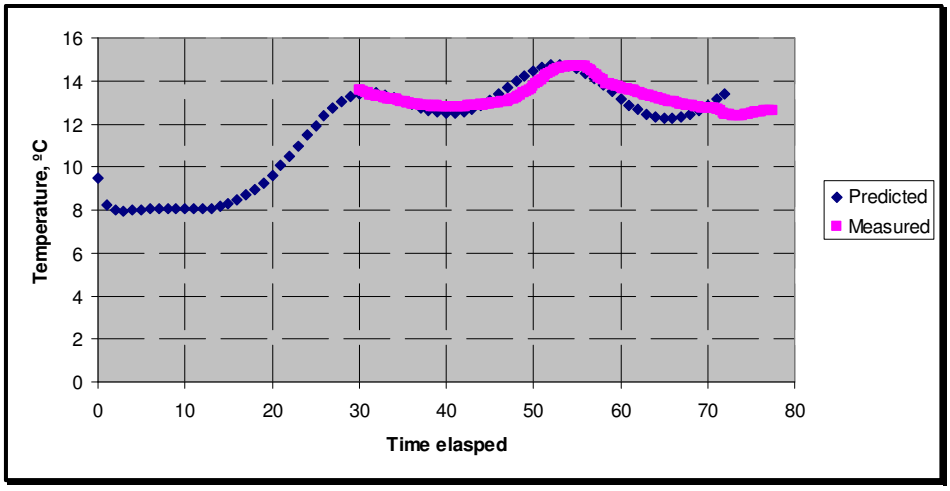

Fig. V-24. Temperature Histories Comparison at 3 Inch

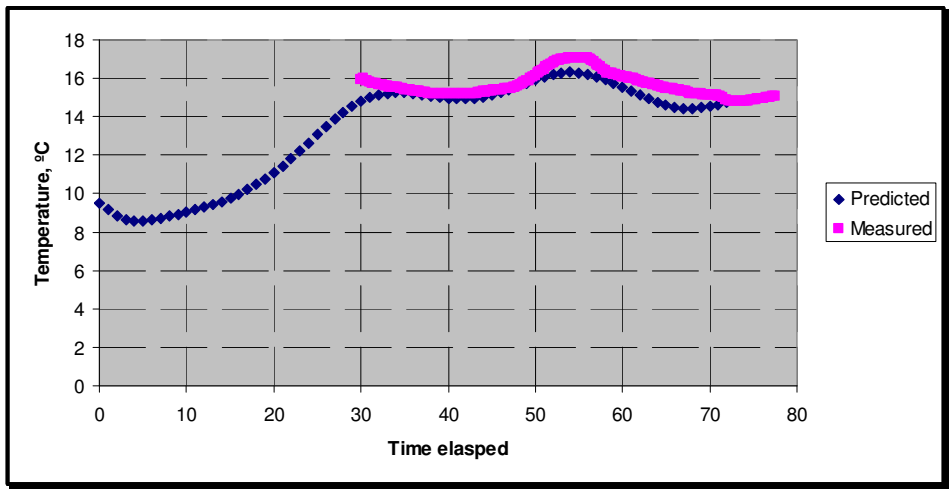

Fig. V-25. Temperature Histories Comparison at 7 Inch

It is observed that, during the first day the concrete temperature was so low and there was hardly any hydration. As a result, the concrete temperature stayed low during the first 20 hours. As the hydration occurred, the concrete temperature began to increase due to the heat that generated by hydration. The predicted temperatures at three different locations match very well with the measured the concrete temperature.

The comparisons between predicted concrete relative humidity and measured concrete relative humidity are presented in Fig. V-26, Fig. V-27, and Fig. V-28, respectively.

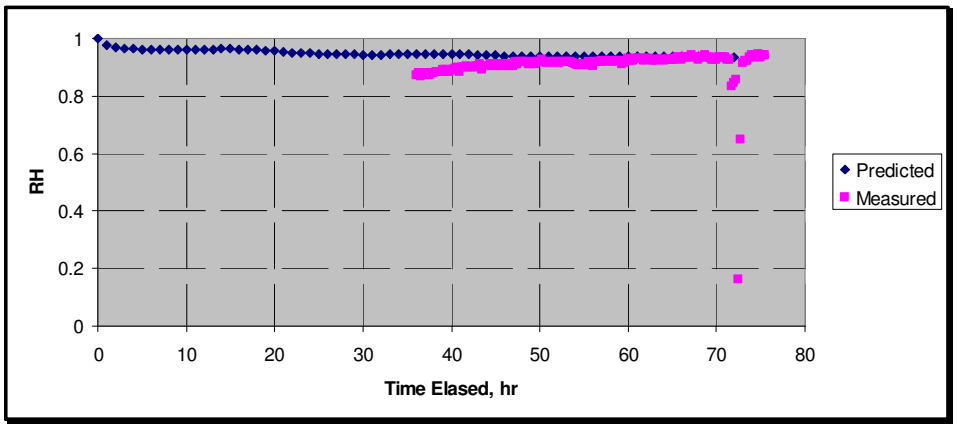

Fig. V-26. RH Histories Comparison at 1 Inch

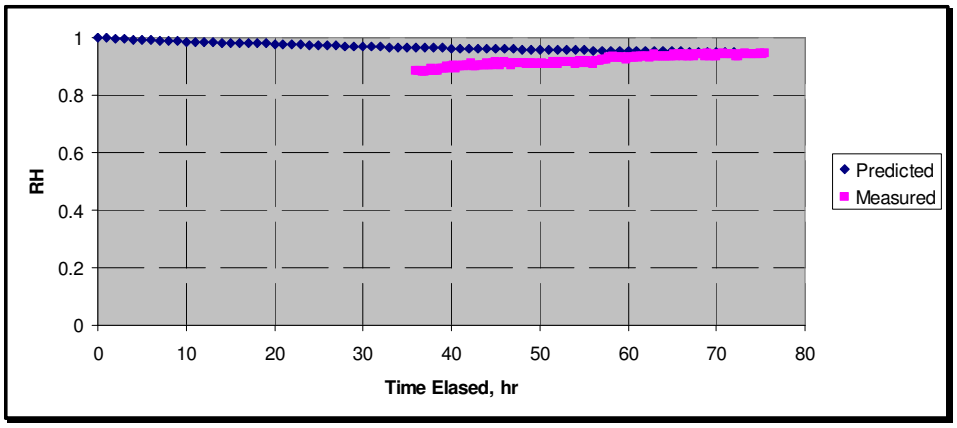

Fig. V-27. RH Histories Comparison at 3 Inch

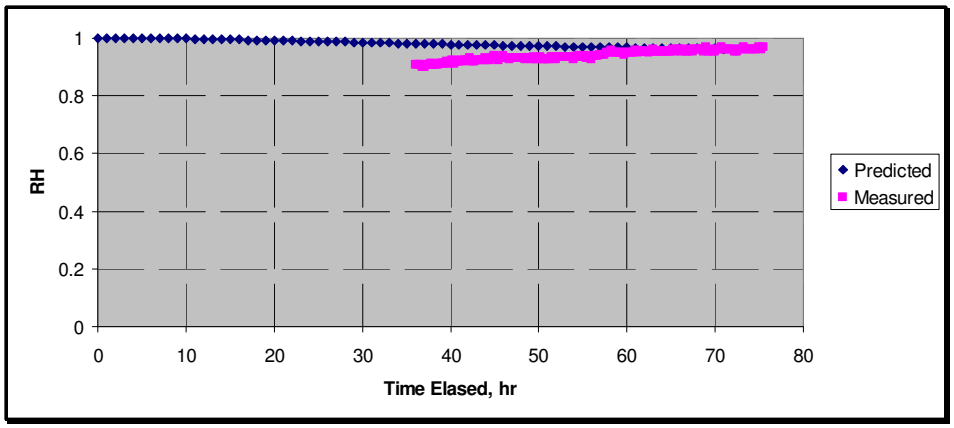

Fig. V-28. RH Histories Comparison at 7 Inch

The concrete relative humidity, measured by chilled mirrors, started off low even though the concrete was still in fresh state and possibly in a saturated condition. However, as the concrete matures the diffusivity decreases and the vapor pressure increases raising the relative humidity. The chilled mirror sensors utilize an electronic heating and cooling system to maintain a constant reading on the dew point temperature of the concrete. The predicted RH at three different locations matches very well with the measured concrete RH as shown in Fig. V-26, Fig. V-27, and Fig. V-28.

Temperature and Moisture Gradients

With known concrete thermal conductivity and moisture diffusivity, temperature and moisture analysis can be predicted other conditions and sections where measurements were not conducted.

The predicted concrete temperature and RH gradients are shown in Fig. V-29, Fig. V-30, Fig. V-31, Fig. V-32, Fig. V-33, Fig. V-34, Fig. V-35, Fig. V-36, Fig. V-37, Fig. V-38, Fig. V-39, and Fig. V-40, respectively.

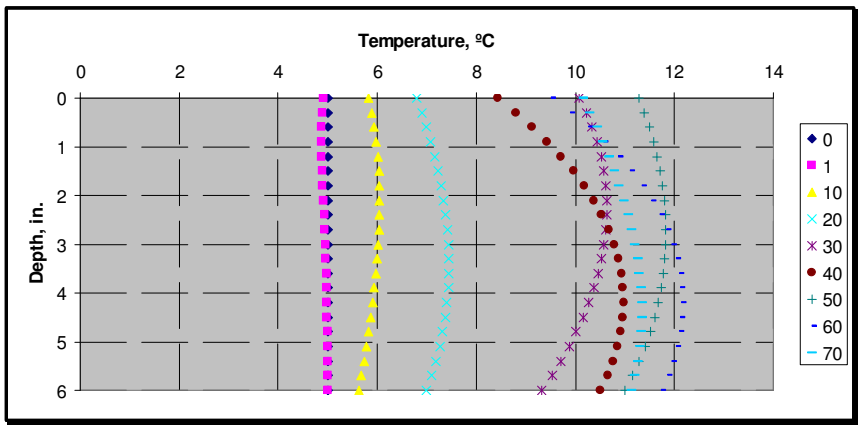

Fig. V-29. Section 1 Bottom Layer Temperature Gradients

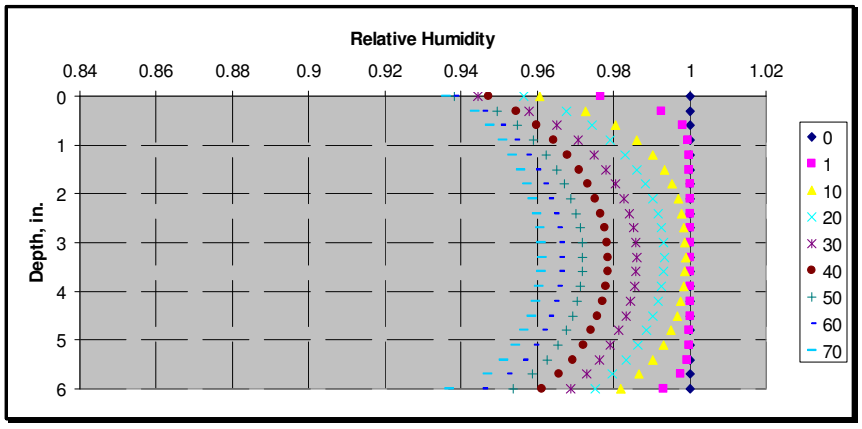

Fig. V-30. Section 1 Bottom Layer RH Gradients

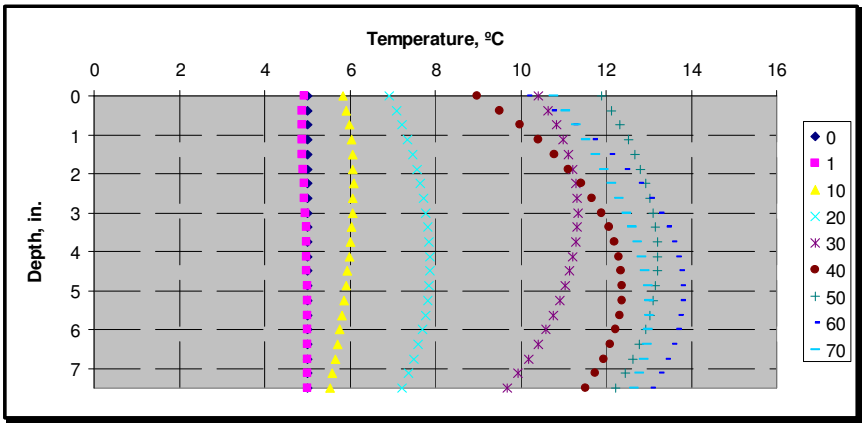

Fig. V-31. Section 2 Bottom Layer Temperature Gradients

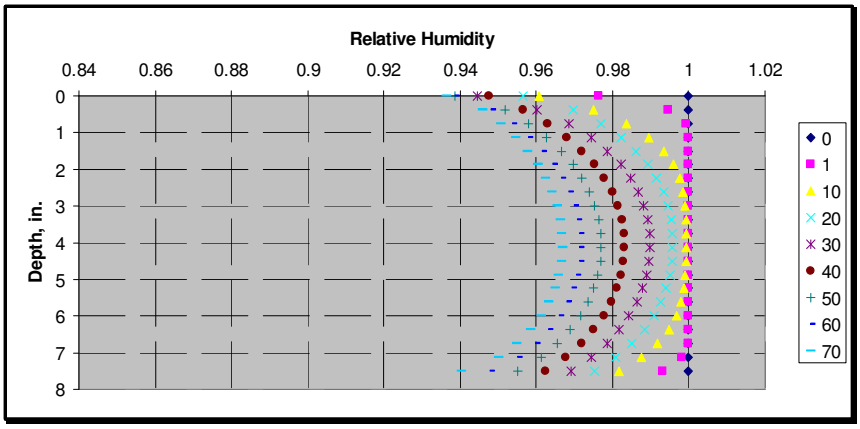

Fig. V-32. Section 2 Bottom Layer RH Gradients

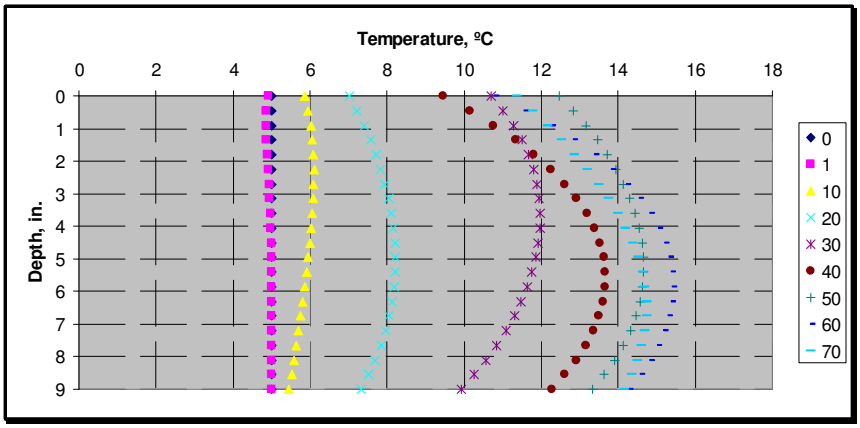

Fig. V-33. Section 3 Bottom Layer Temperature Gradients

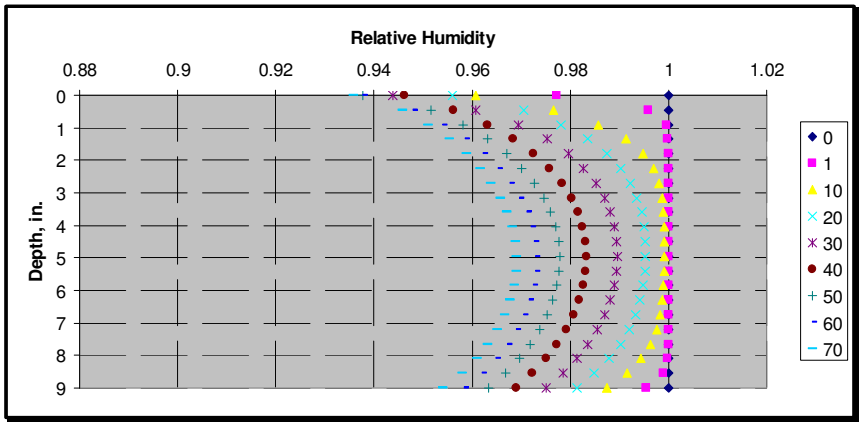

Fig. V-34. Section 3 Bottom Layer RH Gradients

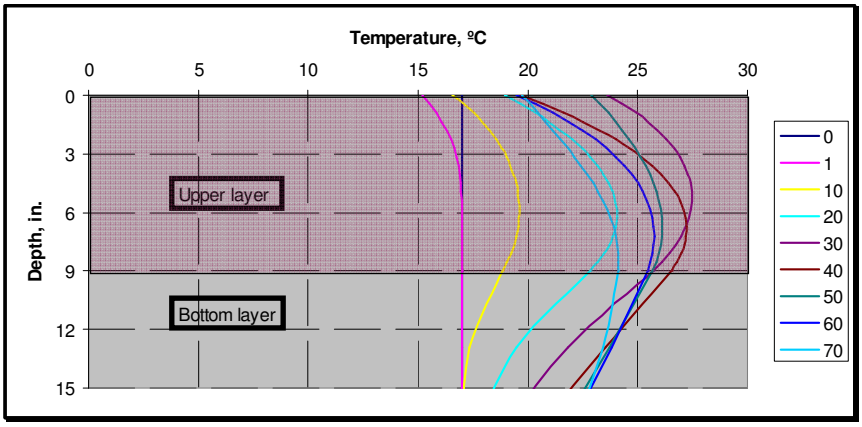

Fig. V-35. Section 1 Top Layer Temperature Gradients

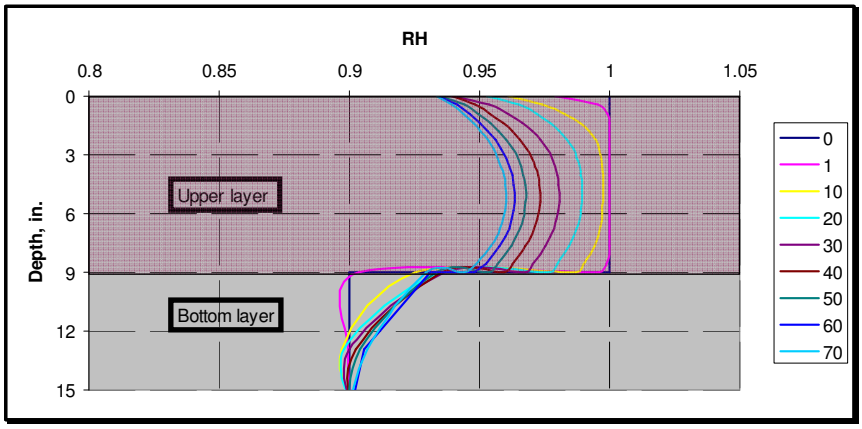

Fig. V-36. Section 1 Top Layer RH Gradients

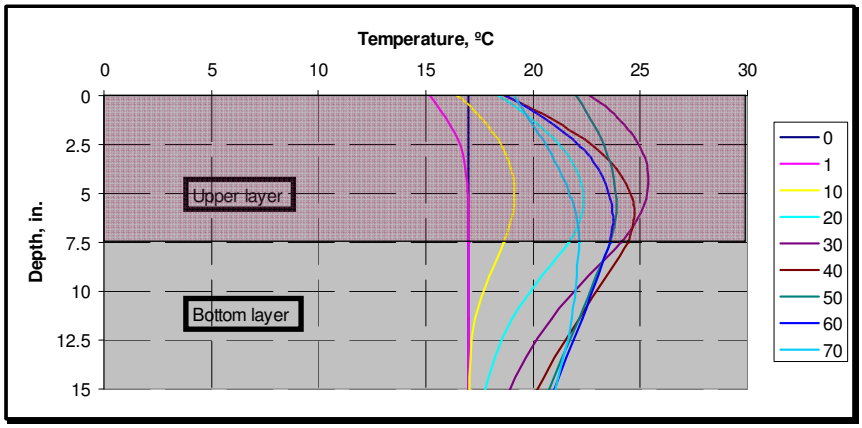

Fig. V-37. Section 2 Top Layer Temperature Gradients

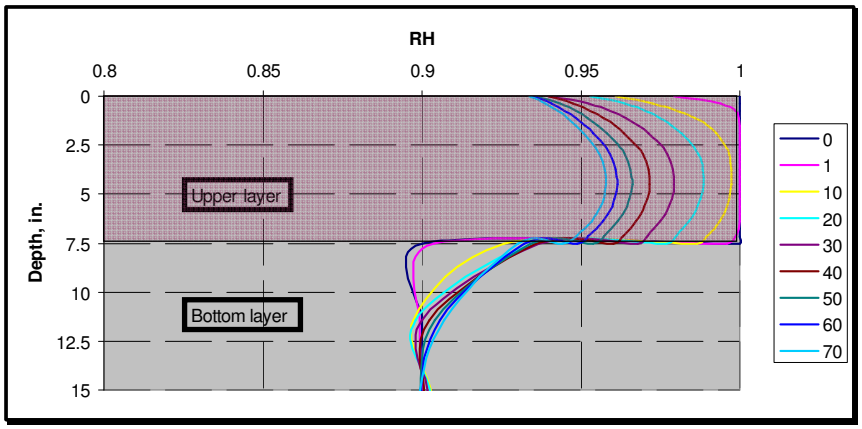

Fig. V-38. Section 2 Top Layer RH Gradients

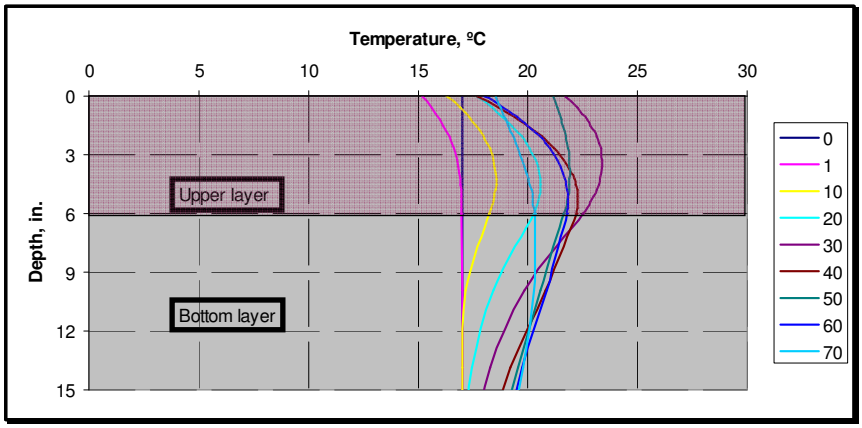

Fig. V-39. Section 3 Top Layer Temperature Gradients

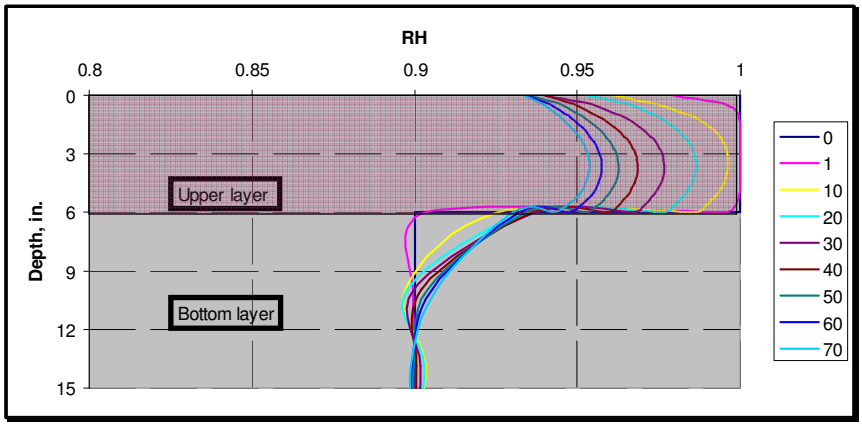

Fig. V-40. Section 3 Top Layer RH Gradients

It is observed that the thicker pavement tends to have larger temperature and moisture gradients, bigger maximum temperature. For bottom layers, the maximum temperatures for each section are 12.2 ºC, 13 ºC and 15.8 ºC respectively, noting that their thicknesses are 6", 7.5", and 9", respectively. For top layers, the maximum temperatures for each section are 27.5 ºC, 26 ºC and 23 ºC respectively while their thicknesses are 9". 7.5", and 6".

The drying of concrete is accredited to two sources: one is the water movement from the concrete to its adjacent medium (top: water evaporates into the air; bottom: water is sucked into less saturated base), the other source is self-desiccation (the water reduction due to hydration lowers the internal relative humidity). Therefore, the concrete at the surface and bottom is subject to both kinds of drying mechanisms and the concrete in the middle depth is subjected mainly to self-desiccation.

The relative humidity for the top layers was decreasing faster than that of the bottom layers. This is because the top layers were cast under relatively warmer ambient conditions which accelerated the hydration process and the self-desiccation.

Set Temperature and Moisture Gradient

As reported previously, the final set maturity was 395 $^{\circ}$C –hr. Before final set, the concrete is still in a semi-plastic form, so temperature and moisture gradient would effectively not produce stress. After final set, the concrete slab can be considered as

rigid and will respond to temperature and moisture gradient thereafter. Therefore, the actual effective temperature and moisture gradient is the forward calculated temperature and moisture gradients offset by the set temperature and moisture gradients. The set temperature and relative humidity gradients are presented in Fig. V-41, Fig. V-42, Fig. V-43, Fig. V-44, Fig. V-45, and Fig. V-46, respectively.

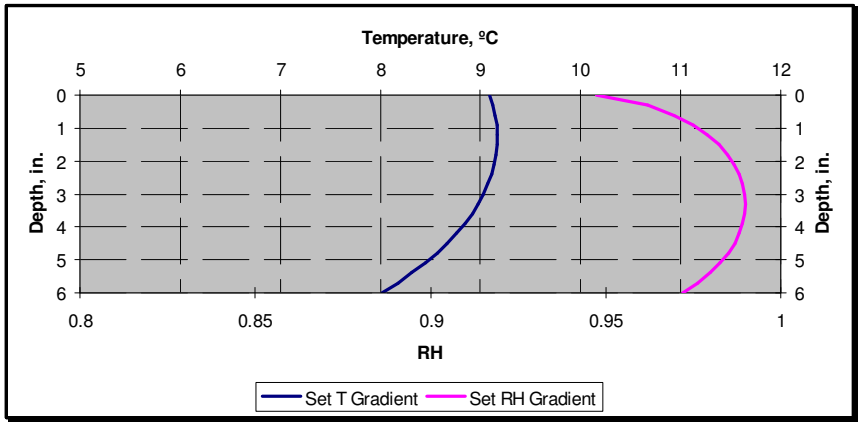

Fig. V-41. Set T and RH Gradients for the Bottom Layer of Section 1

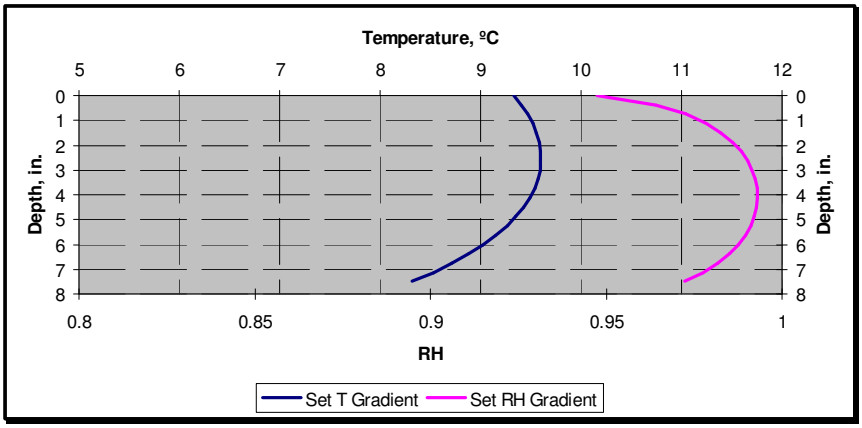

Fig. V-42. Set T and RH Gradients for the Bottom Layer of Section 2

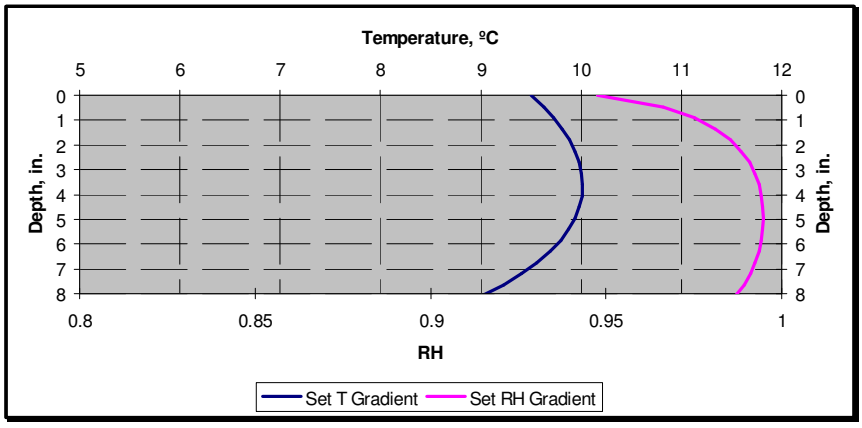

Fig. V-43. Set T and RH Gradients for the Bottom Layer of Section 3

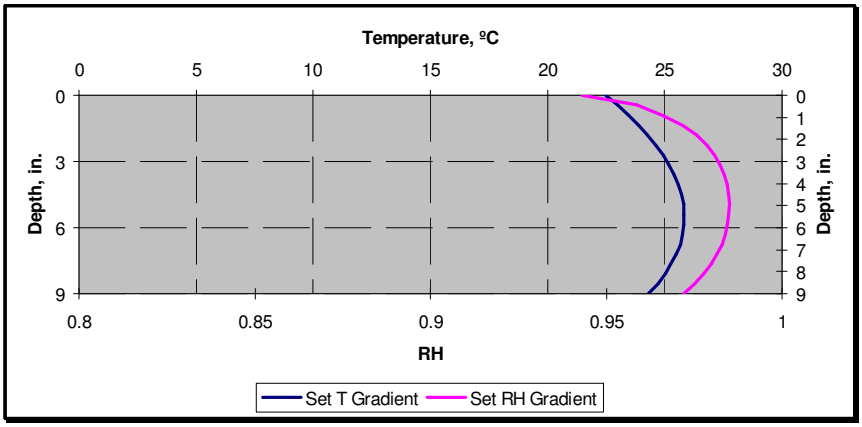

Fig. V-44. Set T and RH Gradients for the Top Layer of Section

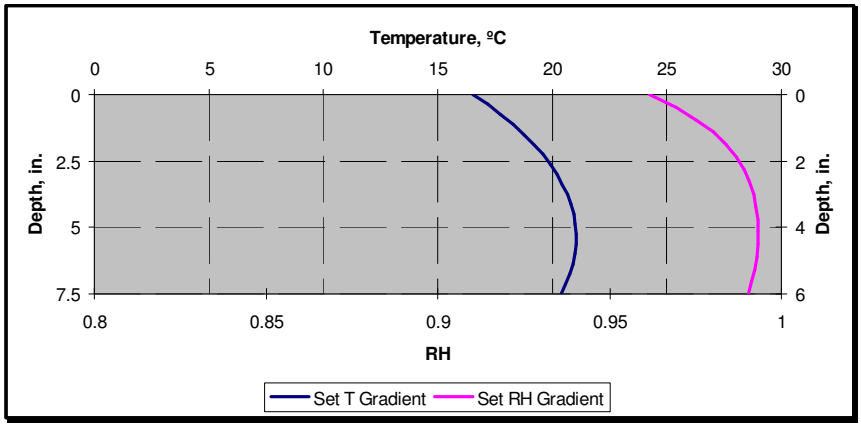

Fig. V-45. Set T and RH Gradients for the Top Layer of Section 2

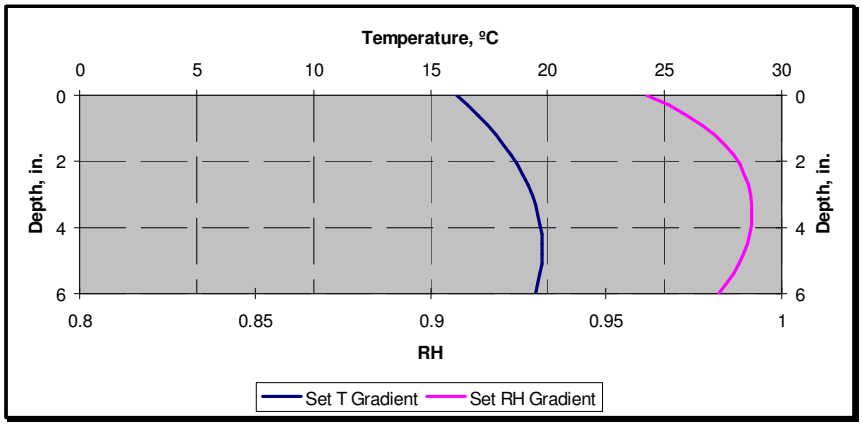

Fig. V-46. Set T and RH Gradients for the Top Layer of Section 3

The concrete set temperatures were higher for thicker pavements. For the bottom layers, the maximum set temperatures were 9.3 ºC, 9.6ºC, and 10ºC respectively from section 1 to section 3 (thicknesses: 6", 7.5", and 9"); while for the top layers, the maximum set temperatures were 26 ºC, 21ºC, and 19.5ºC respectively from section 1 to section 3 (thicknesses: 9", 7.5", and 6"). The concrete set RH gradients show that thinner pavement had larger set moisture gradients.

Equivalent Linear Temperature and Moisture Gradients.

Temperature and moisture gradients through the depth of the concrete pavement are highly nonlinear. It, however, is necessary to transform these nonlinear gradients into equivalent linear gradients in order to conduct curling and warping analysis. The transformation follows in the following equations(Mohamed and Hansen 1997):

$$\Delta T_{eq} = -\frac{12M^*}{\alpha h^2} \tag{V-40}$$

where,

ΔT_{eq} = equivalent linear temperature gradient, °C,

h = slab thickness, m,

α = PCC CTE, m/m/°C, and

M^* = constant dependent on the temperature distribution expressed as shown in the equation (V-41):

$$M^* = \int_{-h/2}^{h/2} \varepsilon(z) z \, dz \tag{V-41}$$

where,

z = distance from slab midplane (z is positive downward), m, and

$\varepsilon(z)$ = strain profile, m/m.

The strain profile is determined by equation (V-42):

$$\varepsilon(z) = \alpha(T_z - T_{z,set}) \tag{V-42}$$

where,

T_z = current temperature at slab depth z, °C, and

$T_{z,set}$ = temperature at slab depth z, at time of set, °C.

Temperature gradient is assumed to be third order polynomial equation as shown in equation (V-43).

$$T_z = A + Bz + Cz^2 + Dz^3 \tag{V-43}$$

where,

A, B, C, and D = coefficients.

Equation (V-44) can be obtained by following through the above equations.

$$\Delta T_{eq} = -12\left(\frac{Bh}{12} + \frac{Dh^3}{80}\right) \tag{V-44}$$

The same procedure is followed to calculate the equivalent linear moisture gradient, except that B and D are the coefficients for moisture profiles.

The equivalent linear temperature and moisture gradients are calculated based on the above equations and the results are listed in Table V-4, Table V-5, Table V-7, Table V-8, and Table V-9, respectively.

Table V-4. Equivalent Linear Temperature and Moisture Gradients for Section 1 Bottom Layer

	Temperature						Moisture					
Time, hours	A	B	C	D	ΔT, °C/in	ΔT, °C/cm	A	B	C	D	ΔRH, 1/in	ΔRH, 1/cm
Set Gradient	9.033700	-0.161600	-0.052800	-0.001900	1.031160	0.405969	0.990901	0.000522	-0.003112	0.000351	-0.014504	-0.005710
10	6.018024	-0.061339	-0.032078	0.003026	0.269992	0.106296	1.000461	0.000222	-0.002900	0.000348	-0.012607	-0.004963
20	7.437321	0.050482	-0.060568	-0.002016	-0.237574	-0.093533	0.994184	0.000766	-0.002890	0.000235	-0.012210	-0.004807
30	10.579648	-0.147207	-0.097313	0.002660	0.797058	0.313802	0.986942	0.000781	-0.003061	0.000321	-0.015086	-0.005940
40	10.786489	0.330352	-0.145647	0.001823	-2.041177	-0.803613	0.978896	0.001415	-0.002604	0.000098	-0.011665	-0.004593
50	11.820086	-0.033169	-0.074651	-0.001458	0.246253	0.096950	0.972694	0.000936	-0.002678	0.000150	-0.010476	-0.004124
60	11.954198	0.325572	-0.147228	0.004880	-2.111544	-0.831317	0.966672	0.001184	-0.002495	0.000004	-0.007234	-0.002848
70	11.198402	0.194603	-0.061510	-0.003888	-1.041647	-0.410097	0.962066	0.001228	-0.002489	-0.000105	-0.003966	-0.001561

Table V-5. Equivalent Linear Temperature and Moisture Gradients for Section 1 Upper Layer

	Temperature						Moisture					
Time, hours	A	B	C	D	ΔT, °C/in	ΔT, °C/cm	A	B	C	D	ΔRH, 1/in	ΔRH, 1/cm
Set Gradient	25.708476	0.235120	-0.114006	-0.001440	-1.958616	-0.771109	0.986293	0.000054	-0.001244	0.000139	-0.015686	-0.006175
10	19.480021	0.211459	-0.086277	0.002123	-2.135281	-0.840662	0.999589	-0.000438	-0.001080	0.000154	-0.012898	-0.005078
20	23.680763	0.448799	-0.136751	-0.000883	-3.942635	-1.552218	0.990668	0.000122	-0.001137	0.000115	-0.013673	-0.005383
30	27.409596	0.177998	-0.134356	0.002486	-1.873826	-0.737727	0.981682	0.000312	-0.001245	0.000124	-0.016367	-0.006444
40	26.425459	0.699400	-0.163721	0.003191	-6.643536	-2.615565	0.973685	0.000800	-0.001123	0.000066	-0.014417	-0.005676
50	25.721084	0.343720	-0.070658	-0.001567	-2.922129	-1.150444	0.968280	0.000802	-0.001115	0.000056	-0.013342	-0.005253
60	25.029909	0.563323	-0.126040	0.005090	-5.626499	-2.215157	0.963764	0.001012	-0.001055	0.000024	-0.011732	-0.004619
70	22.957937	0.550149	-0.051445	-0.003194	-4.602077	-1.811841	0.960434	0.001071	-0.001017	0.000004	-0.010076	-0.003967

Table V-6. Equivalent Linear Temperature and Moisture Gradients for Section 2 Bottom Layer

	Temperature						Moisture					
Time, hours	A	B	C	D	ΔT, °C/in	ΔT, °C/cm	A	B	C	D	ΔRH, 1/in	ΔRH, 1/cm
Set Gradient	9.542299	-0.108712	-0.050505	-0.001894	0.935195	0.368187	0.994502	0.000055	-0.002168	0.000202	-0.013195	-0.005195
10	6.018056	0.077986	-0.022945	0.002550	-0.746262	-0.293804	1.001871	-0.000312	-0.001850	0.000209	-0.010886	-0.004286
20	7.859059	0.058878	-0.055909	-0.001544	-0.343879	-0.135385	0.997148	0.000253	-0.001987	0.000144	-0.011010	-0.004335
30	11.297613	-0.128431	-0.087684	0.002146	0.827431	0.325760	0.991119	0.000265	-0.002174	0.000189	-0.013948	-0.005491
40	12.210912	0.308771	-0.139137	0.002086	-2.447787	-0.963696	0.983793	0.000890	-0.001927	0.000072	-0.011231	-0.004422
50	13.202976	0.062814	-0.080419	-0.001495	-0.376500	-0.148228	0.978001	0.000579	-0.001987	0.000098	-0.010544	-0.004151
60	13.574483	0.320648	-0.138751	0.004593	-2.695511	-1.061225	0.972290	0.000857	-0.001874	0.000023	-0.007883	-0.003104
70	12.732040	0.295005	-0.072214	-0.003111	-2.015670	-0.793571	0.967824	0.000891	-0.001858	-0.000025	-0.005100	-0.002008

Table V-7. Equivalent Linear Temperature and Moisture Gradients for Section 2 Upper Layer

	Temperature						Moisture					
Time, hours	A	B	C	D	ΔT, °C/in	ΔT, °C/cm	A	B	C	D	ΔRH, 1/in	ΔRH, 1/cm
Set Gradient	20.653186	0.480246	-0.155264	0.002228	-3.742836	-1.473557	0.993832	0.000721	-0.001482	0.000139	-0.014204	-0.005592
10	18.978431	0.249278	-0.101588	0.002577	-2.032661	-0.800260	0.998754	-0.000036	-0.001572	0.000237	-0.014728	-0.005798
20	22.007083	0.456357	-0.140960	-0.001200	-3.346740	-1.317614	0.989212	0.000636	-0.001572	0.000168	-0.015401	-0.006063
30	25.347291	0.149589	-0.138005	0.002996	-1.311508	-0.516342	0.979914	0.000855	-0.001678	0.000188	-0.018309	-0.007208
40	23.892763	0.725539	-0.167069	0.003075	-5.636132	-2.218950	0.971715	0.001350	-0.001464	0.000091	-0.015884	-0.006253
50	23.673903	0.235416	-0.061990	-0.001646	-1.661459	-0.654118	0.966122	0.001261	-0.001436	0.000081	-0.014583	-0.005741
60	23.039256	0.569539	-0.134113	0.005609	-4.626487	-1.821452	0.961328	0.001433	-0.001330	0.000031	-0.012709	-0.005004
70	21.211654	0.460348	-0.041286	-0.004014	-3.198599	-1.259291	0.957800	0.001432	-0.001266	0.000001	-0.010803	-0.004253

Table V-8. Equivalent Linear Temperature and Moisture Gradients for Section 3 Bottom Layer

	Temperature						Moisture					
Time, hours	A	B	C	D	ΔT, °C/in	ΔT, °C/cm	A	B	C	D	ΔRH, 1/in	ΔRH, 1/cm
Set Gradient	13.738056	0.239902	-0.079101	-0.001765	-1.966115	-0.774061	0.994245	-0.000290	-0.001348	0.000166	-0.015542	-0.006119
10	9.647213	0.248842	-0.049086	0.001479	-2.401307	-0.945396	1.001724	-0.000693	-0.001115	0.000168	-0.012134	-0.004777
20	12.024298	0.377481	-0.084944	-0.001210	-3.265016	-1.285439	0.996914	-0.000159	-0.001218	0.000134	-0.013222	-0.005205
30	15.479632	0.184493	-0.104614	0.001671	-1.843161	-0.725654	0.990926	-0.000072	-0.001362	0.000158	-0.016629	-0.006547
40	16.418013	0.529377	-0.146020	0.002786	-5.069042	-1.995686	0.983907	0.000568	-0.001215	0.000092	-0.015172	-0.005973
50	16.847553	0.350312	-0.090713	-0.000797	-3.065656	-1.206951	0.978518	0.000448	-0.001246	0.000105	-0.015514	-0.006108
60	16.903467	0.503962	-0.131759	0.004644	-5.043479	-1.985622	0.987342	0.000729	-0.001158	0.000070	-0.014216	-0.005597
70	15.710982	0.529392	-0.078012	-0.001798	-4.567917	-1.798392	0.969421	0.000766	-0.001115	0.000055	-0.012908	-0.005082

Table V-9. Equivalent Linear Temperature and Moisture Gradients for Section 3 Upper Layer

	Temperature						Moisture					
Time, hours	A	B	C	D	ΔT, °C/in	ΔT, °C/cm	A	B	C	D	ΔRH, 1/in	ΔRH, 1/cm
Set Gradient	19.331327	0.539077	-0.170839	0.002497	-3.315365	-1.305262	0.991557	0.001662	-0.002131	0.000191	-0.016160	-0.006362
10	18.365736	0.296281	-0.119703	0.003065	-1.876992	-0.738973	0.997147	0.000804	-0.002394	0.000375	-0.016974	-0.006683
20	20.235695	0.446877	-0.142203	-0.001541	-2.631334	-1.035958	0.986581	0.001441	-0.002219	0.000263	-0.017167	-0.006759
30	23.363454	0.107269	-0.141474	0.003516	-0.757532	-0.298241	0.976705	0.001656	-0.002316	0.000306	-0.019850	-0.007815
40	21.456141	0.737773	-0.169080	0.002770	-4.516386	-1.778105	0.968184	0.002088	-0.001940	0.001280	-0.054000	-0.021260
50	21.865600	0.095887	-0.052430	-0.001404	-0.529832	-0.208595	0.962324	0.001832	-0.001881	0.000121	-0.014912	-0.005871
60	21.189169	0.580638	-0.144056	0.005920	-3.675636	-1.447101	0.957215	0.001914	-0.001699	0.000031	-0.012488	-0.004917
70	19.663757	0.339655	-0.028658	-0.004618	-1.888307	-0.743428	0.953486	0.001829	-0.001597	-0.000028	-0.010067	-0.003963

SUMMARY

This chapter synthesizes current models to conduct the early age concrete temperature and moisture analysis. Since it is an aging problem, the thermal conductivity and moisture diffusivity vary as concrete matures. Moisture capacity concept is induced to characterize the water movement by means of relative humidity so that the relative humidity drop due to self-desiccation can be modeled. With these integrated knowledge at hand, the FEM formulae are derived. These formulae are very useful to conduct temperature and moisture analysis for early-age concrete pavement.

The temperature and moisture gradients obtained from the actually measurements conducted at NAPTF were utilized to characterize the concrete thermal conductivity and moisture diffusivity. Then, further analysis was carried out to calculate the temperature and moisture gradients in all other sections. Set temperature and moisture gradients were calculated based on the set maturity. Equivalent linear temperature and moisture gradients were calculated for further mechanical analysis purpose..

CHAPTER VI
SHEAR DEFORMABLE SLAB CURLING AND WARPING

Curling and warping are important concrete slab behavior. Currently, beam and plate theories are used to model concrete slab mechanical behavior. These theories, however, assume the cross section normal perpendicular to cross section, which eliminates the occurrence of transverse shear. Even if thick plate theory is adapted, the shear stress obtained is constant throughout the cross section. Field data and numerical simulation have shown that the actual temperature and moisture profiles through the depth of concrete pavements are highly nonlinear. And these nonlinear gradients make the assumption of beam and plate theories non-valid anymore. The occurrence of mid-depth delamination shows the evident that there must be some in-plane shear, which thin (or thick) beam and plate theories cannot explain. This chapter attempts to use high order shear deformable beam theory to analyze curling and warping of behavior of infinite plate due to nonlinear temperature and moisture gradients. Kinematical assumption is given, from which the governing equations and boundary conditions are derived using energy method. Finite element method is used to solve this problem.

KINEMATICS ASSUMPATION

For a slab with a side of infinite dimension, it can be simplified as plane strain problem. A unit strip is taken out of the infinite slab for analysis as shown in Fig. VI-1. The *y* direction is the infinite dimension and z is the thickness direction. The full expansions of displacement fields, *U* and *W*, are shown in equations (VI-1) and (VI-2), respectively.

Simplifications on equation (VI-1) and (VI-2) are often made according to its specific geometry. Euler-Bernoulli beam and Timoshenko beam are of the most popular ones. In Euler-Bernoulli theory, the kinematical assumptions are shown in (VI-3) and (VI-4), which means the vertical cross section is always perpendicular to the middle plane (Fig. VI-2). Thus, there is no shear strain based on the assumption.

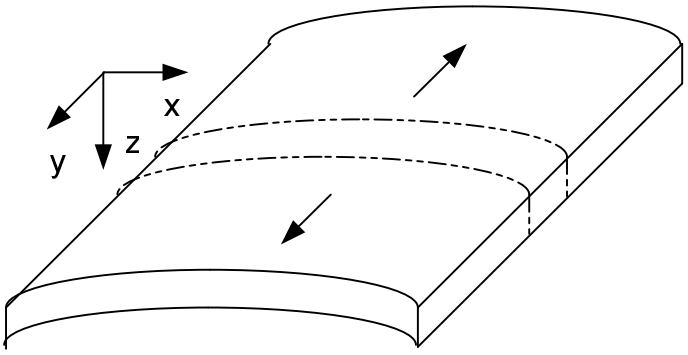

Fig. VI-1. Diagram of a Slab with Infinite Width

$$U(x,z) = u(x) + z\theta_1(x) + z^2\theta_2(x) + z^3\theta_3(x) + z^4\theta_4(x) + \cdots \tag{VI-1}$$

$$W(x,z) = w(x) + z\psi_1(x) + z^2\psi_2(x) + z^3\psi_3(x) + z^4\psi_4(x) + \cdots \tag{VI-2}$$

where

U = displacement in x direction,

W = displacement in z direction,

u = displacement in x direction at the middle plane,

w = displacement in z direction at the middle plane,

θ_i = expansion coefficients, and

ψ_i = expansion coefficients.

$$U(x,z) = u(x) - z\frac{dw}{dx} \tag{VI-3}$$

$$W(x,z) = w(x) \tag{VI-4}$$

The kinematical assumption for the U of Timoshenko theory is presented in (VI-5). An extra parameter, $\theta_{1,}$ is introduced. As a result, there is a constant shear strain throughout the cross section.

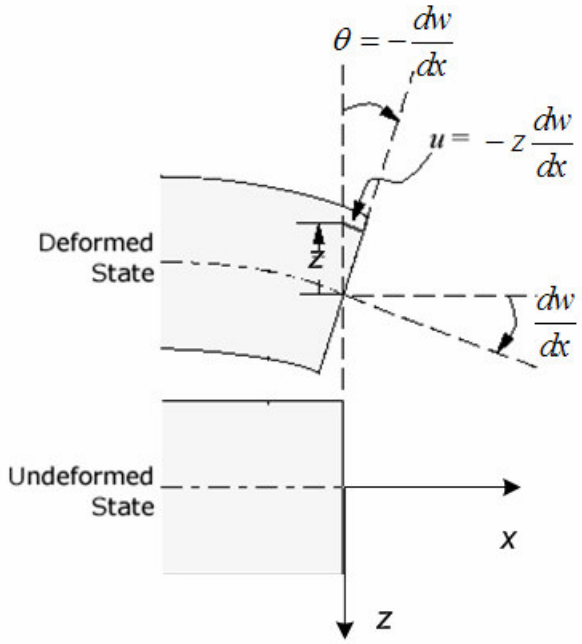

Fig. VI-2. Diagram of Euler-Bernoulli Beam

$$U(x,z) = u(x) + z\theta_1(x) \tag{VI-5}$$

In this special study, nonlinear internal strains will be considered so it is wise to give more freedom in *x* direction to accommodate these strains. A 4th order expansion in z direction is used in this study as shown in equation (VI-6). The vertical displacement, W, is still the same as equation (VI-4).

$$U(x,z) \approx u(x) + z\theta_1(x) + z^2\theta_2(x) + z^3\theta_3(x) + z^4\theta_4(x) \tag{VI-6}$$

Although high order approximation is applied in *x* direction, the overall deformation of this research is still falling into the category of small deformation. Therefore, linear strain formulae are used as shown in equations (VI-7) and (VI-8).

$$\varepsilon_{xx} = \frac{\partial U}{\partial x} \tag{VI-7}$$

$$\gamma_{xz} = \frac{\partial U}{\partial z} + \frac{\partial W}{\partial x} \tag{VI-8}$$

where

ε_{xx} = the normal strain on cross section, and

γ_{xz} = the shear strain on cross section.

Thus the strains according to this kinematical assumption are as follows:

$$\varepsilon_{xx} = \frac{du(x)}{dx} + z\frac{d\theta_1(x)}{dx} + z^2\frac{d\theta_2(x)}{dx} + z^3\frac{d\theta_3(x)}{dx} + z^4\frac{d\theta_4(x)}{dx} \tag{VI-9}$$

$$\gamma_{xz} = \theta_1(x) + 2z\theta_2(x) + 3z^2\theta_3(x) + 4z^3\theta_4(x) + \frac{dw(x)}{dx} \tag{VI-10}$$

It should be noted that the transverse shear strains are zeros at the top and bottom of the slab, $\theta_1, \theta_2, \theta_3, \theta_4,$ and w are not linear independent. This is because the slab top is free of restraints and the slab bottom is in contact with Winkler foundation, which can only have stiffness in the normal direction. Therefore the shear strains must satisfy:

$$\gamma_{xz}\big|_{z=\pm\frac{b}{2}} = \theta_1(x) + 2z\theta_2(x) + 3z^2\theta_3(x) + 4z^3\theta_4(x) + \frac{dw(x)}{dx} = 0 \tag{VI-11}$$

where

b = the thickness of the beam.

Equation (VI-11) leads to two linear independent equations (VI-12) and (VI-13).

$$\theta_1 + 2\frac{b}{2}\theta_2 + 3\left(\frac{b}{2}\right)^2\theta_3 + 4\left(\frac{b}{2}\right)^3\theta_4 + \frac{dw}{dx} = 0 \qquad \text{(VI-12)}$$

$$\theta_1 - 2\frac{b}{2}\theta_2 + 3\left(\frac{b}{2}\right)^2\theta_3 - 4\left(\frac{b}{2}\right)^3\theta_4 + \frac{dw}{dx} = 0 \qquad \text{(VI-13)}$$

Solve the above equations and then the total number of variables can be reduced by assigning θ_3 and θ_4 by other variables as shown in equations (VI-14) and (VI-15).

$$\theta_3 = -\frac{4}{3b^2}\left(\frac{dw}{dx} + \theta_1\right) \qquad \text{(VI-14)}$$

$$\theta_4 = -\frac{2}{b^2}\ \theta_2 \qquad \text{(VI-15)}$$

Substituting equation (VI-14) and (VI-15) into equation (VI-6), equation (VI-16) is obtained.

$$U(x,z) = u(x) + \left(z - \frac{4}{3b^2}z^3\right)\theta_1(x) + \left(z^2 - \frac{2}{b^2}z^4\right)\theta_2(x) - \frac{4}{3b^2}z^3\frac{dw}{dx} \qquad \text{(VI-16)}$$

Accordingly, the strains are simplified into equation (VI-17) and (VI-18).

$$\varepsilon_{xx} = \frac{du}{dx} + \left(z - \frac{4}{3b^2}z^3\right)\frac{d\theta_1}{dx} + \left(z^2 - \frac{2}{b^2}z^4\right)\frac{d\theta_2}{dx} - \frac{4}{3b^2}z^3\frac{d^2w}{dx^2} \qquad \text{(VI-17)}$$

$$\gamma_{xz} = \left(1 - \frac{4}{b^2}z^2\right)\theta_1 + \left(2z - \frac{8}{b^2}z^3\right)\theta_2 + \left(1 - \frac{4}{b^2}z^2\right)\frac{dw}{dx} \qquad \text{(VI-18)}$$

INDUCTION OF INTERNAL STRAIN

Internal strain change due to thermal or moisture change in concrete is a volumetric effect, which means it would not cause the shear strain. So the total normal strain comprise of the mechanical strain and internal strain as shown in equation (VI-19).

$$\varepsilon_{xx} = \varepsilon_M + \varepsilon_I \tag{VI-19}$$

where

ε_M = the strain due to mechanical force, and

ε_I = the strain due to internal strain.

ENERGY FORMULATION

The principle of minimum total potential energy is a fundamental concept used in physics, chemistry, biology, and engineering. It states that a structure or body shall deform or displace to a position that minimizes the total potential energy, with the lost potential energy being dissipated as heat.

The total potential energy is presented in equation (VI-20).

$$\Pi = \mathrm{U} + \mathrm{V} \tag{VI-20}$$

where

Π = total potential energy,

U = internal elastic energy, and

V = external energy.

If the structure is at a stationary position when an infinitesimal variation from such position applied there is no change in energy.

$$\delta\Pi = \delta(\mathrm{U} + \mathrm{V}) = 0 \tag{VI-21}$$

where

δ = variational operator.

The variation of internal energy is given in equation (VI-22) and the variation of external energy, which is caused by foundation, is given in equation (VI-23).

$$\delta \mathrm{U} = \int \delta \varepsilon^T \sigma d\Omega = \int \delta [\varepsilon_M \quad \gamma_{xz}] \begin{Bmatrix} \sigma_{xx} \\ \tau_{xz} \end{Bmatrix} d\Omega \tag{VI-22}$$

$$\delta \mathrm{V} = \int kw \delta w dx \tag{VI-23}$$

where

k = foundation reaction stiffness.

Expanding equation (VI-22), equation (VI-24) is obtained.

$$\begin{aligned}
&\delta \mathrm{U} = \\
&\int \sigma_{xx} \left[\delta \frac{du}{dx} + \left(z - \frac{4}{3b^2} z^3 \right) \delta \frac{d\theta_1}{dx} + \left(z^2 - \frac{2}{b^2} z^4 \right) \delta \frac{d\theta_2}{dx} - \frac{4}{3b^2} z^3 \delta \frac{d^2 w}{dx^2} \right] d\Omega \\
&+ \int \tau_{xz} \left[\left(1 - \frac{4}{b^2} z^2 \right) \delta\theta_1 + \left(2z - \frac{8}{b^2} z^3 \right) \delta\theta_2 + \left(1 - \frac{4}{b^2} z^2 \right) \delta \frac{dw}{dx} \right] d\Omega \\
&= E \int_0^L \left(\frac{du}{dx} b + \frac{7}{120} b^3 \frac{d\theta_2}{dx} \right) \delta \frac{du}{dx} + \left(\frac{17}{315} b^3 \frac{d\theta_1}{dx} - \frac{4}{315} b^3 \frac{d^2 w}{dx^2} \right) \delta \frac{d\theta_1}{dx} dx \\
&+ E \int_0^L \left(\frac{7}{120} b^3 \frac{du}{dx} + \frac{107}{20160} b^5 \frac{d\theta_2}{dx} \right) \delta \frac{d\theta_2}{dx} + \left(-\frac{4}{315} b^3 \frac{d\theta_1}{dx} + \frac{1}{252} b^3 \frac{d^2 w}{dx^2} \right) \delta \frac{d^2 w}{dx^2} dx \\
&+ G \int_0^L \left(\frac{8}{15} b \frac{du}{dx} + \frac{8}{15} b \frac{dw}{dx} \right) \delta\theta_1 + \left(\frac{8}{105} b^3 \theta_2 \right) \delta\theta_2 + \left(\frac{8}{15} b \frac{du}{dx} + \frac{8}{15} b \frac{dw}{dx} \right) \delta \frac{dw}{dx} dx \\
&- \int \delta \varepsilon_M (E \varepsilon_I) d\Omega
\end{aligned} \tag{VI-24}$$

GOVERNING EQUATIONS

Governing equations can be obtained by integrating by parts of the explicit form of equation (VI-21).

In order to simplify the equation (VI-24), the following notations are used while doing the integration by parts.

$$N = Et\left(\frac{du}{dx}b + \frac{7}{120}b^3\frac{d\theta_2}{dx}\right) \tag{VI-25}$$

$$M = Et\left(\frac{7}{120}b^3\frac{du}{dx} + \frac{107}{20160}b^5\frac{d\theta_2}{dx}\right) \tag{VI-26}$$

$$M' = Et\left(-\frac{4}{315}b^3\frac{d\theta_1}{dx} + \frac{1}{252}b^3\frac{d^2w}{dx^2}\right) \tag{VI-27}$$

$$M^* = Et\left(-\frac{4}{315}b^3\frac{d\theta_1}{dx} + \frac{1}{252}b^3\frac{d^2w}{dx^2}\right) \tag{VI-28}$$

$$T = Gt\left(\frac{8}{15}b\frac{du}{dx} + \frac{8}{15}b\frac{dw}{dx}\right) \tag{VI-29}$$

$$T' = Gt\left(\frac{8}{105}b^3\theta_2\right) \tag{VI-30}$$

$$T^* = Gt\left(\frac{8}{15}b\frac{du}{dx} + \frac{8}{15}b\frac{dw}{dx}\right) \tag{VI-31}$$

After integrating by parts, the variation form of energy statement is presented in equation.

$$\begin{aligned}
\delta\Pi &= \int_0^L N\delta\frac{du}{dx} + M\delta\frac{d\theta_1}{dx} + M'\delta\frac{d\theta_2}{dx} + M^*\delta\frac{d^2w}{dx^2}dx \\
&+ \int_0^L T\delta\theta_1 + T'\delta\theta_2 + T^*\delta\frac{dw}{dx}dx - \int_0^L kw\delta w dx - \int \delta\varepsilon_M (E\varepsilon_I) dV \\
&= -\int_0^L \frac{dN}{dx}\delta u + \left(\frac{dM}{dx} - T\right)\delta\theta_1 + \left(\frac{dM'}{dx} - T'\right)\delta\theta_2 + \left(kw + \frac{dT^*}{dx} - \frac{d^2M^*}{dx^2}\right)\delta w dx \\
&- \int \delta\varepsilon_M (E\varepsilon_I) d\Omega \\
&+ N\delta u\Big|_0^L + M\delta\theta_1\Big|_0^L + M'\delta\theta_2\Big|_0^L + M^*\delta\frac{dw}{dx}\Big|_0^L + \left(T^* - \frac{dM^*}{dx}\right)\delta w\Big|_0^L
\end{aligned} \tag{VI-32}$$

Since internal strains are determined only the thermal and moisture state of concrete, they are independent of those variables. Thus their effects only manifest in boundary terms.

According to each variable, there is governing equation.

For δu, the governing equation is presented in equation (VI-33).

$$\frac{dN}{dx} = 0 \tag{VI-33}$$

For $\delta\theta_1$, the governing equation is presented in equation (VI-34).

$$\frac{dM}{dx} - T = 0 \tag{VI-34}$$

For $\delta\theta_2$, the governing equation is presented in equation (VI-35).

$$\frac{dM'}{dx} - T' = 0 \tag{VI-35}$$

For δw, the governing equation is presented in equation (VI-36).

$$kw + \frac{dT^*}{dx} - \frac{d^2M^*}{dx^2} = 0 \tag{VI-36}$$

Continuity requirements are $u, \theta_1, \theta_2, w, \frac{dw}{dx}$ and these variables are essential boundary conditions. N, M, M', M*, and (T*-dM*/dx) are natural boundary conditions.

FINITE ELEMENT MODEL

Interpolation Functions

From the previous section, it is discussed that u, θ_1, θ_2 need to have a continuity requirement of first order polynomial, so linear Lagrange interpolation functions are used. For *w*, it has continuity requirement of at least up to second order of polynomial, so quadratic Hermite interpolation functions are used.

The linear Lagrange interpolation functions are presented in equation (VI-37) and (VI-38). Their first order derivatives with respect to *x* are presented in equation (VI-39) and (VI-40), respectively.

$$N_1 = \frac{L - x}{L} \tag{VI-37}$$

$$N_2 = \frac{x}{L} \tag{VI-38}$$

where

L = the length of the element.

$$N_{1x} = -\frac{1}{L} \tag{VI-39}$$

$$N_{2x} = \frac{1}{L} \tag{VI-40}$$

The quadratic Hermite interpolation functions are presented in equations (VI-41), (VI-42), (VI-43), and (VI-44), respectively. And the second order derivative are presented in equations (VI-41), (VI-45) and (VI-49) respectively.

$$f_1 = 1 - 3\left(\frac{x}{L}\right)^2 + 2\left(\frac{x}{L}\right)^3 \tag{VI-41}$$

$$f_2 = x\left(1 - \frac{x}{L}\right)^2 \tag{VI-42}$$

$$f_3 = 3\left(\frac{x}{L}\right)^2 - 2\left(\frac{x}{L}\right)^3 \tag{VI-43}$$

$$f_4 = x\left[\left(\frac{x}{L}\right)^2 - \frac{x}{L}\right] \tag{VI-44}$$

The first order derivatives with respect to x are presented in equations (VI-45), (VI-46), (VI-47), and (VI-48), respectively.

$$f_{1x} = \frac{6x(-L+x)}{L^3} \tag{VI-45}$$

$$f_{2x} = \frac{(-L+x)(-L+3x)}{L^2} \tag{VI-46}$$

$$f_{3x} = -\frac{6x(-L+x)}{L^3} \tag{VI-47}$$

$$f_{4x} = \frac{x(3x-2L)}{L^2} \tag{VI-48}$$

The second order derivatives with respect to x are presented in (VI-49), (VI-50), (VI-51), and (VI-52), respectively.

$$f_{1xx} = \frac{6(2x-L)}{L^3} \tag{VI-49}$$

$$f_{2xx} = \frac{2(3x-2L)}{L^2} \tag{VI-50}$$

$$f_{3xx} = -\frac{6(2x-L)}{L^3} \tag{VI-51}$$

$$f_{4xx} = \frac{2(-L+3x)}{L^2} \tag{VI-52}$$

As a result, the variables are approximated in the equation (VI-53), (VI-54), (VI-55), and (VI-56), respectively. Index notation is used here.

$$u = N_i u_i \tag{VI-53}$$

$$\theta_1 = N_i \theta_{1i} \tag{VI-54}$$

$$\theta_2 = N_i \theta_{2i} \tag{VI-55}$$

$$w = f_i w_i \tag{VI-56}$$

Stiffness Matrix

For elasticity problem, the element stiffness matrix is always carrying the following form (VI-57).

$$K^e = \int B^T DB d\Omega \tag{VI-57}$$

where

D = constitutive matrix, and

B = kinematical matrix.

B matrix is given by the following equation.

$$B = \frac{\partial \varepsilon_i}{\partial q_j} = \begin{bmatrix} N_{1x} & 0 \\ \left(z - \frac{4}{3b^2} z^3\right) N_{1x} & \left(1 - \frac{4}{b^2} z^2\right) N_1 \\ \left(z^2 - \frac{2}{b^2} z^4\right) N_{1x} & \left(2z - \frac{8}{b^2} z^3\right) N_1 \\ -\frac{4}{3b^2} z^3 f_{1xx} & \left(1 - \frac{4}{b^2} z^2\right) f_{1x} \\ -\frac{4}{3b^2} z^3 f_{2xx} & \left(1 - \frac{4}{b^2} z^2\right) f_{2x} \\ N_{2x} & 0 \\ \left(z - \frac{4}{3b^2} z^3\right) N_{2x} & \left(1 - \frac{4}{b^2} z^2\right) N_2 \\ \left(z^2 - \frac{2}{b^2} z^4\right) N_{2x} & \left(2z - \frac{8}{b^2} z^3\right) N_2 \\ -\frac{4}{3b^2} z^3 f_{3xx} & \left(1 - \frac{4}{b^2} z^2\right) f_{3x} \\ -\frac{4}{3b^2} z^3 f_{4xx} & \left(1 - \frac{4}{b^2} z^2\right) f_{4x} \end{bmatrix}^T \tag{VI-58}$$

where

ε_i = strains, and

q_j = unknowns.

The foundation will enhance the stiffness of the element stiffness matrix. It bears of the form of equation (VI-59).

$$K^{e}{}_{foundation} = \int_{0}^{L} k f_i f_j dx \qquad \text{(VI-59)}$$

As stated earlier, the internal strains will manifest themselves in the boundary terms. In each element, they are calculated by the following equation.

$$Q^{e} = \int \delta\varepsilon_M (E\varepsilon_I) d\Omega = \int B_{i,1} (E\varepsilon_I) d\Omega \qquad \text{(VI-60)}$$

Assembling all the element stiffness matrixes and load vectors together, the global stiff matrix and load vectors are obtained and they should satisfy equation (VI-61).

$$(K + K_{foundation}) q = Q \qquad \text{(VI-61)}$$

EXAMPLE CALCULATION

Assume the material properties and slab dimensions are shown in Table VI-1.

Table VI-1. Material Properties and Slab Dimensions

Young's modulus, psi	3,000,000
Poisson's ratio	0.15
Slab Thickness, in.	12
Slab Length, ft	12

Internal strain distribution is assumed to be a fourth order of polynomial function, which is shown in equation (VI-62).

$$\varepsilon_I = -4.2134E\text{-}07z^4 - 1.6025E\text{-}06z^3 + 9.3452E\text{-}06z^2 + 2.3440E\text{-}05z - 2.2214E\text{-}05 \quad \text{(VI-62)}$$

The shear strain distributions along the slab thickness direction are shown in Fig. VI-3. Location 1 is at the edge of the slab and location 7 is at the center of the slab. It is observed that at each cross section there are two peak shear strains with one at the top and the other at the bottom. Given the fact that the internal strain change dramatically at the top part of concrete slab, shear strains at the top are much higher than those at the bottom, especially at the edge of the slab. As approaching to the center of the slab, the shear strains are getting smaller and the shear strains are zero at the center cross section.

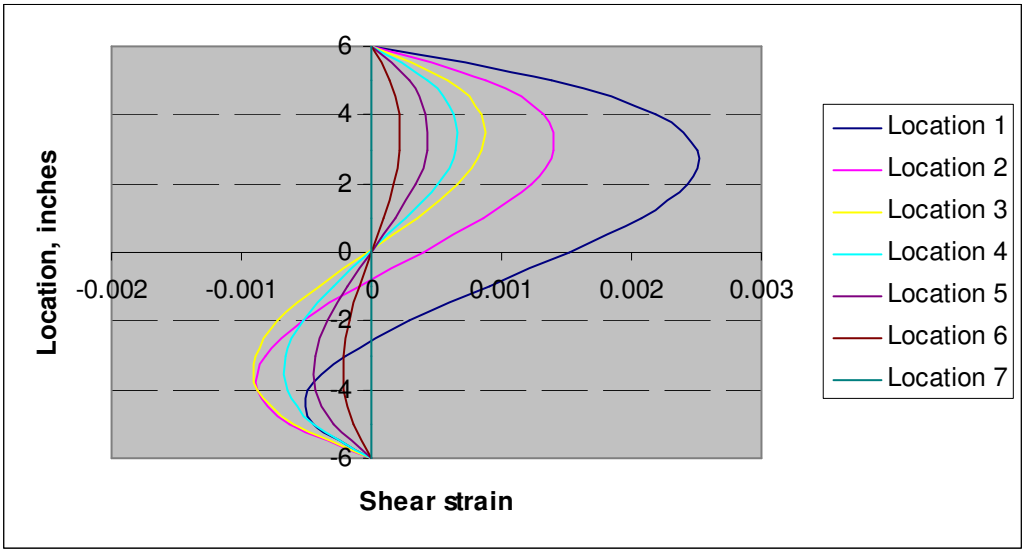

Fig. VI-3. Shear Strain Distributions

SUMMARY

This chapter is attempting to use high order shear deformable theory to conduct concrete slab curling and warping analysis due to nonlinear temperature and moisture gradients. Since temperature and moisture change more dramatically at the top of the concrete slab, a corresponding internal strain profile, with sharp change at the top, is assigned to

conduct the curling analysis. It is found out that there is peak shear strain under the slab surface and it bears the maximum value at the edge of the slab.

CHAPTER VII
CONCLUSIONS

This study is trying to accomplish three objectives: developing a laboratory test protocol for curing evaluation which has a field application, characterizing heat transfer and moisture transport in early-age concrete, and modeling concrete slab curling and warping behavior.

Ensuring sufficient water availability in hydrating concrete is of great importance to produce delamination resistant concrete for both short-term and long- term performance of concrete pavement. Excessive early-age evaporation from the surface of concrete pavement results in high porosity concrete, delamination, and loss of strength. Current laboratory curing membrane evaluation method ASTM C 156 has three deficiencies, which are singular experimental conditions, usage weight loss of mortar specimen, and moisture loss limit based on the compression strength of cylindrical specimen. A new laboratory protocol is developed. It ranks the curing membrane by the shape of the ECT curve that it generates under standard testing conditions. A field protocol was also developed. The field protocol is carried out under a factorial of application rates and PE. Thus it is possible to guide curing practice based on the ambient conditions and type of curing compound.

Extensive field tests were conducted to investigate the curing effectiveness from both a moisture retention standpoint and a physical properties standpoint. It is found out that uniformity of curing membrane is of most important factor affecting curing quality; manual spray has higher possibility to result in non-uniform curing membrane; the second coat in the same day when concrete is placed helps to increase curing quality, especially for manual spray; and Curing compound application in the second does not help to increase the curing quality.

Mechanistic models characterizing the behavior of on-site concrete are becoming more and more demanding. This study integrates the most updated models about the early-age concrete heat transfer and moisture transport. Thermal conductivity and

moisture diffusivity are modeled as a function of concrete temperature, concrete moisture and degree of hydration. Moisture capacity is applied in the formulation, which makes it possible to simulate the relative humidity drop due to self-desiccation. The finite element formulae are derived to solve the nonlinear and coupled heat transfer and moisture transport differential equations. A case study was carried out in a full scale concrete test pavement at the FAA National Airport Pavement Test Facility near Atlantic City, New Jersey. Temperature and moisture data were recorded at three different positions at one section. And these data were used to backcalculate the thermal conductivity and moisture diffusivity of the on-site concrete mixture. The predicted temperature and moisture histories match very well with the measurements. Then the backcalculated material properties were used to forward calculate the temperature and moisture gradients on all other sections. Set maturity was measured and then set temperature and moisture gradients were calculated.

Another effort in this study is to use high order shear deformable theory to account for the curling and warping behavior of concrete slab due to nonlinear temperature and moisture gradients. It is found out that there are maximum shear strains under the surface of the concrete slab top where there are the most dramatic temperature and moisture gradients.

REFERENCES

ASTM. (2003). *Standard Specification for Liquid Membrane-forming Compounds for Curing Concrete*. ASTM C-309, West Conshohocken, PA.

ASTM. (1999a). *Standard Test Method for Length Change of Hardened Hydraulic-Cement Mortar and Concrete*. ASTM C-157, West Conshohocken, PA.

ASTM (1999b). *Standard Test Method for Penetration Resistance of Hardened Concrete*. ASTM C-803, West Conshohocken, PA.

Bažant, Z. P. (1970). "Constitutive Equation for Concrete Creep and Shrinkage Based on Thermodynamics of Multiphase Systems." *Materials and Structures*, 3(13), 3-36.

Bažant, Z. P. and L. J. Najjar (1972). "Nonlinear Water Diffusion in Nonsaturated Concrete." *Materials and Structures*, 5(25), 3-20.

Boer, J. H. d. (1953). *The Dynamical Character of Adsorption*. Clarendon at the University Press, London.

Bradbury, R. D. (1938). *Reinforced Concrete Pavements*, Wire Reinforcement Institute Washington, D.C.

Branco, F. A., R. A. Mendes, and E. Mirabell. (1992). "Heat of Hydration Effects in Concrete Structures." *ACI Materials Journal*, 89(2), 139-145.

Buch, N. and D. G. Zollinger (1993). "Preliminary Investigation on Effects of Moisture on Concrete Pavement Strength and Behavior." *Transportation Research Record 1382*, Transportation Research Board, Washington, D.C., 26-31.

Byrum, C. R. (2001). *A High Speed Profiler Based Slab Curvature Index for Jointed Concrete Pavement Curling and Warping Analysis*. Doctoral Dissertation, University of Michigan, Dearborn.

Carino, N. J. (1991). "The Maturity Method." in *CRC Handbook on Non-destructive Testing of Concrete*. V. M. Malhotra and N. J. Carino (eds.), CRC Press, Boca Raton, FL, 101-146.

Carrier, R. E. and P. D. Cady (1970). "Evaluating Effectiveness of Concrete Curing Compounds." *Journal of Materials*, 5(2), 294-302.

Chapman, A. J. (1982). *Fundamentals of Heat Transfer*. Macmillan Inc, New York.

Choubane, B. and M. Tia (1992). "Nonlinear Temperature Gradient Effect on Maximum Warping Stresses in Rigid Pavement." *Transportation Research Record 1370*, Transportation Research Board, Washington, D.C., 11-19.

Choubane, B. and M. Tia (1995). "Analysis and Verification of Thermal-Gradient Effects on Concrete Pavement." *Journal of Transportation Engineering*, 121(1), 75-81.

Copeland, L. E. and J. C. Hayes (1953). "The Determination of Non-evaporable Water in Hardened Portland Cement Paste." *ASTM Bulletin* 194, 70-74.

Dalton, J. (1802). "Experimental Essays on Evaporation." *Manchester Literary and Philosophical Society of Manchester*, 5, 536-62.

Davis, H. E. (1940). "Autogenous Volume Change of Concrete." *Proceedings of ASTM*, 40, 1102-1110.

Dempsey, B. J., W. A. Herlache, and A. J. Patel. (1986). "Climatic-Materials-Structural Pavement Analysis Program." *Transportation Research Record 1095*, Transportation Research Board, Washington, D.C., 111-123.

Dilley, A. C. (1968). "On the Computer Calculation of Vapor Pressure and Specific Humidity Gradients from Psychometric Data." *Journal of Applied Meteorology*, 7, 717-719.

du Plessis, L. and J. T. Harvey (2003). *Environmental Influences on the Curling of Concrete Slabs at the Palmdale HVS Test Site*. CSIR Transportek, University of California, Berkeley.

Fang, Y. (2001). "Environmental Influences on Warping and Curling of PCC Pavements." 7th International Conference on Concrete Pavements, Orlando, FL., 1, 1-7.

Fwa, T. F. (2006). *Handbook of Highway Engineering*. Taylor & Francis Group, LLC, Boca Raton, FL.

Gates, D. M. (1965). "The Measurement of Water Vapor Boundary Layers in Biological Systems with a Radio Refractrometer." in *Humidity and Moisture, Vol. 2*. A. Wexler, Ed. In Chief, E. J. Amdur, Ed., Reinhold Publ. Co., New York, 33.

Gates, D. M. and G. M. Benedict (1963). "Convection Phenomena from Plants in Still Air." *Am. J. Bot.*, 50(6), 563-573.

Gates, D. M., M. J. Vetter, and M. C. Thompson. (1963). "Measurement of Moisture Boundary Layers and Leaf Transpiration with a Microwave Refractometer." *Nature*, 197, 1070 – 1072.

Gause, G. R. and J. Tucker (1940). "Method for Determining the Moisture Condition in Hardened Cocnrete." *J. Res. Natl. Bur. Stand.*, 25, 403-416.

Gregg, S. J., K. S. W. Sing, and Salzberg, H. W. (1967). "Adsorption Surface Area and Porosity." *ECS*. 114, 279C.

Hsieh, C. K., C. Qin, and E. E. Ryder. (1989). *Development of Computer Modeling for Prediction of Temperature Distribution Inside Concrete Pavements*. Report FL/DOT/SO/90-374, Department of Mechanical Engineering, University of Florida, Gainesville, FL.

Hveem, F. N. (1951). "Slab Warping Affects Pavement Joint Performance." *ACI*, 47(6), 797-808.

Incropera, F. P. and D. P. DeWitt (1996). *Fundamentals of Heat and Mass Transfer*, John Wiley & Sons, New York.

Jeong, J. H. (2003). *Characterization of Slab Behavior and Related Material Properties due to Temperature and Moisture*. Doctoral Dissertation, Texas A&M University, College Station, Tx,.

Jeong, J. H. and D. G. Zollinger (2004). "Early-Age Curling And Warping Behavior: Insights from a Fully Instrumented Test-Slab System." *Transportation Research Board 1896*, Transportation Research Board, Washington D.C., 66-74.

Jones, F. E. (1969). *Barium Fluoride Film Humidity Element Calibration Analysis, Applications and Other Developments*. Report 10058, National Bureau of Standards. Washington D.C.

Jones, F. E. (1991). *Evaporation of Water: With Emphasis on Applications and Measurements*. Lewis Publishers, Inc., Chelsea, MI.

Jones, F. E. and A. Wexler (1960). "A Barium Fluoride Film Hygrometer Element." *J. Geophys. Res.,* 65, 2087.

Kant, T. and A. Gupta (1988). "A Finite Element Model for a Higher-order Shear-deformable Beam Theory." *Journal of Sound and Vibration*, 125(2), 193-202.

Kapila, D., J. Falkowsky, and J. L. Plawsky. (1997). "Thermal Effects during the Curing of Concrete Pavements." *ACI Materials Journal*, 94(2), 119-128.

Kasi, S. S. H. and S. E. Pihlajavaara (1969). *An Approximate Solution of a Quasi-Linear Diffusion*. The Station Institute for Technical Research, Helsinki, Finland.

Kaviany, M. (1994). *Principles of Convective Heat Transfer*. Springer-Verlag, New York.

Klemens, P. G. (1969). *Theory of the Thermal Conductivity of Solids*. Academic Press, London, England.

Kohler, M. A., T. J. Nordenson, and W. E. Fox. (1955). *Evaporation from Pans and Lakes*. U.S. Department of Commerce, Washington D.C.

Lasseter, F. P. (1931). "Concrete." *Cement Mill Ed*., 38, 89-92.

Linsley, R. K., M. A. Kohler, and J. L. Paulhus. (1975). *Hydrology for Engineers*. McGraw-Hill, New York.

Mehta, P. K. and P. J. M. Monteiro (2006). *Concrete: Microstructure, Properties, and Materials*, McGraw-Hill, New York.

Meinel, A. B. and M. P. Meinel (1976). *Applied Solar Energy: An Introduction*. Addison-Wesley, Reading, MA.

Menzel, C. A. (1954). "Causes and Prevention of Crack Development in Plastic Concrete." *Portland Cement Association Annual Meeting*, 130-136.

Mikhail, R. S. (1983). *Microstructure and Thermal Analysis of Solid Surfaces*. John Wiley & Sons, New York.

Miller, J. S. and W. Y. Bellinger (2003). *Distress Identification Manual for the Long-Term Pavement Performance Program*. Federal Highway Administration, McLean, VA.

Mindess, S. and J. F. Young (1981). *Concrete*. Prentice-Hall, Inc., Englewood Cliffs, NJ.

Mohamed, A. R. and W. Hansen (1997). "Effect of Nonlinear Temperature Gradient on Curling Stress in Concrete Pavements." *Transportation Research Board 1568*, Transportation Research Board, Washington D.C., 65-71.

Mukhopadhyay, A. K., D. Ye, et al. (2006). *Moisture-related Cracking Effects on Hydrating Concrete Pavement*. Texas Transportation Institute, College Station, TX.

Murray, F. W. (1967). "On the Computation of Saturation Vapor Pressure." *Journal of Applied Meteorology*, 6(1), 203-204.

Neville, A. M. (1996). *Properties of Concrete*. John Wiley and Sons, New York.

Parrott, L. J. (1988). "Moisture Profiles in Drying Concrete." *Advances in Cement Research*, 1(3), 164-170.

Parrott, L. J. (1991). "Factors Influencing Relative Humidity in Concrete." *Magazine of Concrete Research*, 43(154), 45-52.

Pasternak, P. L. (1954). "On a New Method of Analysis of an Elastic Foundation by Means of Two Foundation Constants." *Gos. Izd. Lit*., Po Strait I Arkh, Moscow.

Penman, H. L. (1948). "Natural Evaporation from Open Water." *Bare Soil and Grass*, JSTOR., 193, 120-145.

Penman, H. L. (1948). "Natural Evapotranspiration from Open Water, Bare Soil, and Grass." *Proceedings of the Royal Society of London*, Series A, 193, 120–145.

Pihlajavaara, S. E. (1964). *Introductory Bibliography for Research on Drying of Concrete.* The State Institute for Technical Research, Helsinki, Finland.

Powers, T. C. (1947). "A Discussion of Cement Hydration in relation to the Curing of Concrete." *Highway Resource Board*, Washington D.C., 27, 178-188.

Reissner, E. (1945). "The Effect of Transverse Shear Deformation on the Bending of Elastic Plates." *Journal of Applied Mechanics*, 12(11), 69-76.

Ruiz, J. M., A. K. Schindler, R. O. Rasmussen, P. K. Nelson, and G. K. Chang. (2001). "Concrete Temperature Modeling and Strength Prediction Using Maturity Concepts in the FHWA HIPERPAV Software." *Proceedings 7th International Conference on Concrete Pavements*, Orlando, FL.

Says, W. M. and M. E. Crawford (1980). *Convective Heat and Mass Transfer*. McGraw-Hill, New York.

Shiba, K. and M. Ueda (1965). "Humidity Distribution and Rate of Evaporation of Water." in *Humidity and Moisture*, *Vol. 2.* A. Wexler, Ed. in Chief, E. J. Amdur, Ed., Reinhold Publ. Co., New York, 349.

Siegel, R. and J. R. Howell (1981). *Thermal Radiation Heat Transfer*. McGraw-Hill, New York.

Swayze, M. A. (1942). "Early Concrete Volume Changes and Their Control." *American Concrete Institute*, 13(5), 425-440.

Teller, L. W. and E. C. Sutherland (1935). "Part 2: Observed Effects of Variations in Temperature and Moisture on the Size, Shape and Stress Resistance of Concrete Pavement Slabs." *The Structural Design of Concrete Pavements*, 16, 169-197.

Tetens, O. (1930). "Uber Einige Meteorologische Begriffe Z." *Geophysics*, 6, 203-204.

Thepchatri, T., C. P. Johnson, and H. Matlock. (1977). *Prediction of Temperature and Stresses in Highway Bridges by a Numerical Procedure Using Daily Weather Reports*. Center for Transportation Research, The University of Texas at Austin.

Thornthwaite, C. W. (1948). "An Approach toward a Rational Classification of Climate." *JSTOR.*, 38, 55-94.

Timoshenko, S. P. and S. Woinowsky-Kreiger (1959). *Theory of Plates and Shells*. McGraw Hill, New York.

Vandenbossche, J. M. (1999). *A Review of the Curing Compounds and Application Techniques Used by the Minnesota Department of Transportation for Concrete Pavements*. Minnesota DOT Final Report 2001-06, Minnesota Department of Transportation.

Veihmeyer, F. J. (1964). *Handbook of Applied Hydrology*, McGraw-Hill, New York.

Verbeck, G. J. (1955). "Hardened Concrete - Pore Structure." *ASTM Sp. Tech Publ.*, (169), 136-42.

Wainwright, P. J. and J. G. Cabrera (1990). "Assessment of the Efficiency of Chemical Membranes to Cure Concrete." *Proceedings of an International Conference on the Protection of Concrete*, Dundee, Scotland, 907-920.

Walker, S. and D. L. Bloem (1957). "Studies of Flexural Strength of Concrete-Part 3: Effects of Variations in Testing Procedures." *Highway Research Board*, 57, 1122-1139.

Wang, J. C. C. K. and Z. Ge (2003). "Investigation onto Improved Pavement Curing Materials and Techniques." *Proceedings of the 2003 Mid-Continent Transportation Research Symposium*, Ames, IA.

Westergaard, H. M. (1926). "Analysis of Stresses in Concrete Pavements Due to Variation of Temperature." *Proceedings of Highway Research Board*, 6, 201-214.

Westergaard, H. M. (1927). "*Theory of Concrete Pavement Design*." *Proceedings of Highway Research Board*, 19, 197-202.

Whiting, N. M. and M. B. Snyder (2003). "Effectiveness of Portland Cement Concrete Curing Compounds." *Transportation Research Record 1834*, Transportation Research Board, Washington D.C., 59-68.

Wu, C. H. and T. J. Larsen (1993). "Analysis of Structural Response of Concrete Pavements under Critical Thermal Loading Conditions." *Proceedings of 5th International Conference on Concrete Design and Construction*, Purdue University, Lafayette, Ind., 1, 317–340.

Xi, Y., Z. P. Bažant, et al. (1994). "Moisture Diffusion in Cementious Materials." *Advanced Cement Based Materials*, 1, 258-266.

Xin, D., D. G. Zollinger, et al. (1995). "An Approach to Determine Diffusivity in Hardening Concrete Based on Measured Humidity Profiles." *Advanced Cement Based Materials*, 2, 138-144.

Yang, S. (1996). *A Temperature Prediction Model in New Concrete Pavement and New Test Method for Concrete Fracture Parameters*. Doctoral Dissertation, Texas A&M University, College Station, TX.

Ytterberg, R. F. (1987), "Shrinkage and Curling of Slabs on Grade—Part 2: Warping and Curling," *Concrete International*, 9(5), 54-61.

Zhang, J., T. F. Fwa, K. H. Tan, and X. P. Shi. (2003). "Model for Nonlinear Thermal Effect on Pavement Warping Stresses." *Journal of Transportation Engineering*, 12(6), 695-702.

VITA

Dan Ye obtained both his B.S. and M.S. degrees in civil engineering as Southeast University in Nanjing China. After receiving his M.S. degree in 2003, he worked for Shanghai Municipal Engineering Design General Institute. In September 2003, he began his doctorate study in the Zachary Department of Civil Engineering at Texas A&M University in College Station, Texas. He served as a graduate research assistant on several projects from FHWA (Federal Highway Administration) and TxDOT (Texas Department of Transportation).

Address: CE/TTI Building 501J
College Station, TX 77840-3135
USA
Email: yeahokcn@hotmail.com